



ANNUAL **R**EPORT

2022

Kansai Photon Science Institute
Foundational Quantum Technology Research Directorate
National Institutes for Quantum Science and Technology

KPSI
ANNUAL
REPORT
2022

Contents

Preface	1
Activities of KPSI	4
User Facilities	14
Research Highlights	20
Publication Lists	54
The Kids' Science Museum of Photons	66
Appendix	70

はじめに

本年報では、関西光科学研究所（以下、関西研）において 2022 年度に実施された研究開発の主だった成果を紹介しています。関西研は国立研究開発法人量子科学技術研究開発機構（以下、量研）の研究開発拠点であり、けいはんな学研都市にある京都府木津地区と兵庫県播磨地区の 2 か所に研究サイトを持っています。木津地区では、世界トップレベルの高強度レーザー技術を基盤としたレーザー加速やレーザーの短パルス性を活かした超高速計測技術開発、またそれらの産業・医療等への応用研究、さらに量子生命科学の最先端の研究開発を実施しています。また、播磨地区では、大型放射光施設 SPring-8 の 2 本の専用ビームラインと計算機シミュレーションを活用することで、新しい放射光 X 線利用技術開発と物質材料科学の最先端研究を展開しています。

量研関西研として 7 年が経ち、2022 年度も優れた研究成果が得られて来ております。木津地区のレーザー科学分野においては、高強度レーザーの相対論的透過現象によるレーザー駆動イオン加速の飛躍的な高効率化や集光前のレーザー空間プロファイルの整形によるレーザー加速電子ビームの安定化・高品質化、また、二次元電子分光装置の開発と生体分子における量子コヒーレンスの検出やレーザー照射された固体からの高調波発生メカニズムの計算科学的解析、さらにはシミュレーションデータと実験データに基づく複雑なレーザープラズマ EUV スペクトルのモデリングやダブルガスジェットによる高調波発生とそれを用いた EUV レジスト材料の評価などについて着実な成果を挙げました。量子生命科学分野においては、シミュレーションを用いた遺伝子制御に関わるヌクレオソーム構造動態の解明や原子間力顕微鏡を用いた DNA 損傷と修復における新知見などの成果が得られました。また、播磨地区においても、高圧下での金属の水素吸蔵に関する放射光メスバウアー分光分析や機能性結晶材料の局所構造解析、SPring-8 に隣接された X 線自由電子レーザー施設 SACLA を利用した分子のクーロン爆発時のダイナミクス解析、また、量研で発見した X 線の磁気光学効果である X 線磁気円偏光発光のスペクトルの理論計算などで優れた成果を挙げています。さらに、光技術の社会実装の観点からは、病理診断への応用を目指した中赤外顕微鏡の開発やレーザー打音検査技術の道路橋への実用化に向けた取り組みを引き続き行っています。

関西研は、2023 年 4 月 1 日より、関西光量子（こうりょうし）科学研究所となりました。関西光量子科学研究所は、「光」をキーワードとして我が国の量子科学技術の発展とイノベーションの創出へ貢献する研究拠点としての役割を果たすとともに地域にも世界にも開かれた研究所となれるよう、職員一同、より一層努力してまいります。皆様のご理解・ご協力を宜しくお願い申し上げます。

2023 年吉日

関西光量子科学研究所 所長

田中 淳

Preface

This annual report from Kansai Photon Science Institute (KPSI) provides highlights of the scientific and technical research that was conducted over the 2022 fiscal year. KPSI is one of the research and development bases of the National Institutes for Quantum Science and Technology (QST) and has two sites, the Kizu site in Keihanna science city in Kyoto prefecture and the Harima site in Hyogo prefecture. At the Kizu site, we are conducting state-of-art research such as developing new-type laser-driven radiation sources such as laser accelerated particle beams and ultrashort X-rays based upon world-leading top-class high-intensity laser technology, ultrafast measurement methodology using ultrashort pulse technology, and quantum life science which helps us understand radiation effects and develop new medicines. At the Harima-site, using two contract beamlines of SPring-8 and computer simulation, we are developing new technology to utilize synchrotron radiation X-rays and carrying out state-of-art research in material science.

Seven years have passed since the restart of KPSI in QST, and several outstanding research results have been obtained this year as well. In the field of laser science at the Kizu site, dramatic improvement of the efficiency of laser-driven ion acceleration through relativistic transmission of the two ultraintense lasers, stabilization and enhancement of laser-accelerated electron beams by shaping the laser near field profile have been obtained. The development of two-dimensional electronic spectroscopy (2D-ES) and the detection of the existence of quantum coherence in biomolecules by the 2D-ES, computational analysis of high harmonic generation from laser-irradiated solids, and modeling of complex EUV spectra from laser plasma by combining theoretical and experimental data for developing a laser plasma EUV source, enhancement of high-order harmonic generation by double gas jets and evaluation of EUV resist materials using it, have been conducted. In the field of quantum life science, elucidation of the dynamics of nucleosome structure with relevance to gene regulation using simulation, and new findings on DNA damage and repair using atomic force microscopy have been obtained. Outstanding research was also conducted at the Harima site, including a synchrotron radiation-based Mössbauer spectroscopy observation of hydrogen absorption in metals under high pressure, a local structural analysis of functional crystalline materials, a study of molecular dynamics during Coulomb explosion induced by X-rays at SACLA (adjacent to SPring-8), and theoretical calculations of the spectra of X-ray magnetic circularly polarized emission - a magneto-optical X-ray effect which was first discovered at QST. Furthermore, from the perspective of social implementation of optical technology, we are continuing to work on the development of a mid-infrared microscopic imaging aimed at application to pathological diagnosis and the practical application of laser hammering inspection technology to road bridges.

The KPSI will play a role as a research base that contributes to the development of quantum science and technology in Japan and the creation of innovation with the keyword "light" and will be a research institute open to the community and society. We appreciate your understanding and cooperation.



Sincerely, 2023
TANAKA Atsushi
Director General of KPSI

Activities of KPSI

関西光科学研究所の主な動き

シンポジウム・研究会の開催等

2022年6月7日

【JST 未来社会創造事業シンポジウム “レーザー駆動イオン加速システムの開発”】

量研が JST より受託している未来社会創造事業「レーザー駆動による量子ビーム加速器の開発と実証」プロジェクトのシンポジウムを、量研と本プロジェクトでオンライン共催しました。

本シンポジウムは、レーザープラズマ加速技術の社会実装に向けて、プロジェクトの主要3テーマのうち量研が担当しているレーザー駆動イオン加速システム開発の内容や成果を一般および関連業界に周知するために実施したものです。参画企業である住友重機械工業株式会社、日立造船株式会社をはじめとした民間企業 48 社 89 名を含む 188 名が参加し、活発な質疑が行われました。



佐野プロジェクトマネージャーの講演の様子（右上：量研平野理事長、右下：大石 JST 運営統括）

2022年6月28日～29日

【光・量子ビーム科学合同シンポジウム 2022 (OPTO 2022)】

大阪大学と量研との間で締結された包括協定に基づき、合同シンポジウム OPTO 2022 を開催いたしました。昨年に続き今年も会場およびオンライン配信によるハイブリッド開催を行いました。参加者は約 186 名で、招待講演を含む講演 8 件、パワーレーザーコミュニティ会議、ポスター発表と若手ポスター表彰、大阪大学近藤賞受賞講演、春に逝去されたレーザー科学研究所教授河仲先生を偲ぶ追悼講演が行われました。また、併催として「パワーレーザーDX プラットフォーム」シンポジウムが 28 日午前中に開催されました。



パワーレーザーコミュニティ会議
ハイブリッドディスカッションの様子

2022年9月2日

【文部科学省マテリアル先端リサーチインフラ事業 JAEA & QST 合同放射光利用講習会】

マテリアル先端リサーチインフラ事業の新規利用者を開拓するために実験装置とその利用方法を説明する講習会をオンラインで日本原子力研究開発機構 (JAEA) と共催しました。まず NIMS の松波副センター長に「ARIM 事業における共用機器からのデータ収集の進め方」について解説していただき、量研 (QST) からは綿貫センター長が「マテリアル先端リサーチインフラ事業の概要」について、藤原研究員が「放射光メスbauer分光装置による鉄系材料の分析」について、齋藤グループリーダーが「放射光を利用した新規水素化物の高温高压合成」について説明しました。講師、スタッフも含めて合計 51 名もの参加があり、盛況でした。

2022年9月6日、10月18日

【インフラメンテナンス最新技術の公開実証実験】

関西研のレーザー打音検査装置を始めとする、戦略的イノベーション創造プログラム(SIP)で開発してきた最新のインフラ点検技術の公開実証実験を、9月に静岡県焼津市、10月に山梨県山梨市で行いました。静岡県交通基盤部と共催した9月の試験では、デジタル庁、国土交通省、自治体、大学、企業等、120名以上の参加者となる大きなイベントとなりました。

山梨県での公開実験は、2012年12月2日に山梨県笹子トンネルで起きた天井板落下事故が日本のインフラ点検のあり方を見つめ直す大きな契機となり、我々がこの研究を始めたきっかけでもあることから、非常に大きな意味があったと考えております。地元からの注目度も非常に高く、土木業界、自治体、大学などの関係者に加えて、山梨県県政記者クラブを通じて多数のメディアからも参加頂き、地元の山梨放送、山梨日日新聞を始め、NHK、TBS、読売新聞など多数のメディアでも紹介されました。

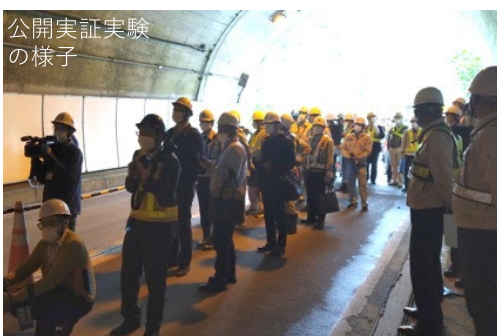
両公開実験を通じ、様々な立場のユーザーからの意見を頂くことができ、今後の開発方向を決める重要なイベントとなりました。



公開実証実験後に開催した説明会の様子



静岡県焼津市での公開実証実験の様子



山梨県山梨市での公開実証実験の様子

2023年2月8日～9日

【第6回 理研光量子工学研究センター・量研関西光科学研究所合同セミナー】

今回6年目を迎えた本合同セミナーは、3年ぶりの対面とオンライン参加を含むハイブリッド形式での開催となりました。理研からは緑川克美センター長を含む8名が関西研に訪し、40名程度（オンライン参加含む）が参加しました。初日は、最先端レーザー開発からイオン加速や生命現象解明などのレーザー応用研究、さらには精密加工や化学反応ダイナミクスの理論研究に至るまで、多岐にわたるテーマの講演と意見交換が行われました。2日目は関西研・実験棟内のレーザー設備などを理研からの参加者に見学していただきました。



**6th
RIKEN-RAP and QST-KPSI
Joint Seminar**

Date: February 8(Wed.)-9(Thu.), 2023
Place: 大会議室A119 KPSI, QST (Hybrid: Microsoft Teams)

[Wed. 8 Feb.]
13:00-13:05 Opening Remarks 河内 哲哉 (QST-KPSI)
13:05-13:40 「ブラスミコンシステムによるJ-KAREN-レーザーの高時間コントラスト化」
今 亮 (QST-KPSI 高強度レーザー科学研究グループ)
13:40-14:15 「High energy, ultrashort CEP-stable IR driving source towards GW isolated attosecond pulses in the water window」
Lu XU (RIKEN-RAP 超高速コヒーレントX線光学研究チーム)
— Break (20 min.) —
14:35-15:10 「PW級J-KARENレーザーと水素クラスターの相互作用による準準色陽子加速」
堀田 拓仁 (QST-KPSI 先端レーザー技術開発グループ)
15:10-15:45 「中性子光学のための超精密加工」
細島 拓也 (RIKEN-RAP 先端光学素子開発チーム)
— Break (20 min.) —
16:05-16:40 「X線化学反応のX線吸収断面積分光理論」
山崎 隆 (RIKEN-RAP 光子科学研究チーム)
16:40-17:15 「10 kHz サブ10 fs可視光/ルビ光の発生とその二次元電子分光への応用」
坪内 雅明 (QST-KPSI 超高速光物性研究グループ)
17:15-17:20 Closing Remarks 緑川 克美 (RIKEN-RAP)

[Thu. 9 Feb.]
9:30-11:50 Laboratory tour & Free discussion @QST-KPSI (Kizu)
参加登録: 2/1 までに kizu-symposium@qst.go.jp へ氏名、所属、現地 or Web参加をご連絡ください

理化学研究所 光量子工学研究センター (RIKEN-RAP)
量子科学技術研究開発機構 関西光科学研究所 (QST-KPSI)

合同セミナーのポスター



現地講演者・主催者集合写真

2023年2月21日

【京大・JAEA・QST 微細構造解析プラットフォーム合同地域セミナー (最新の微細構造・状態解析)】

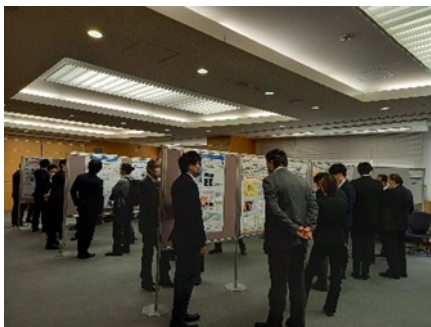
マテリアル先端リサーチインフラ事業の新規利用者を開拓するために支援成果を発表するセミナーをオンラインで京大、JAEA と共催しました。量研からは大和田グループリーダーが「ナノ結晶の内部構造を解明するコヒーレント X 線回折イメージング装置と研究事例の紹介」について、量研専用ビームライン BL11XU に設置したコヒーレント X 線回折イメージング装置を活用して得た研究成果について発表しました。講師、スタッフも含めて合計 44 名もの参加があり、前回以上に盛況でした。様々な業界の企業から 17 名もの参加がありました。近年の講習会やセミナーでは企業参加者の多さ、その業種の多様さが目立つ傾向が続いています。

2023年3月13日

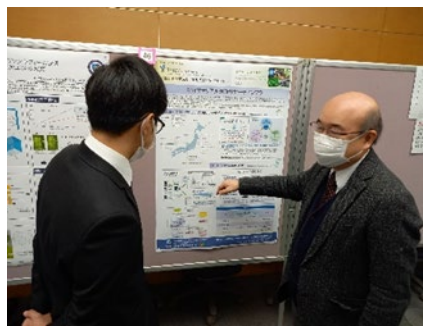
【兵庫県立大学高度産業科学技術研究所ニューズバルシンポジウム 2023】

マテリアル先端リサーチインフラ事業の新規利用者を開拓するため、イーグレひめじで開催された本シンポジウムに協賛し、量研が実施している QST マテリアル先端リサーチインフラ事業についてポスター展示しました。ニューズバルの先生方、及び産学連携・研究推進機構のスタッフに本事業の理解を深め

ていただきました。



ポスター発表会場の様子



QST マテリアル先端リサーチインフラのポスター展示

出展等イベント

7月10日～13日「第22回 SPring-8 夏の学校」開催（大型放射光施設 SPring-8）



第22回 SPring-8 夏の学校ポスター



SPring-8 の量研ビームライン：BL11XU 放射光メスバウアー分光装置での実習の様子

9月4日～7日「第6回 SPring-8 秋の学校」に協力（大型放射光施設 SPring-8）

9月6日～7日「第14回日本放射光学会 放射光基礎講習会 放射光の基礎と活用の可能性」を共催（オンライン）

9月7日～9日「JASIS2022」のマテリアル先端リサーチインフラ事業ブースにポスター展示（幕張メッセ）

9月25日～26日「SPring-8 シンポジウム 2022 - SPring-8 がつむぐ学術と社会のリンケージ -」に協賛（大型放射光施設 SPring-8）

10月6日～7日「けいはんな R&D フェア 2022」へ出展（Web 開催）

10月6日～7日「けいはんなビジネスメッセ 2022」へ出展（けいはんなオープンイノベーションセンター）

10月17日 播磨高原東中学校出前授業

播磨科学公園都市内にある播磨高原広域事務組合立播磨高原東中学校において、3年生16名を対象に出前授業を行いました。新型コロナウイルスの影響で3年ぶりの開催となりました。今年のテーマは「核エネルギーと放射線」としました。実際に身の回りの核反応で発生している自然放射線を簡易な霧箱を使って観察することに挑戦しました。霧箱は耐熱ガラス容器や液体窒素を使って、実際に生徒に組み上げてもらいました。液体窒素をはじめて見た生徒も多かったようで、歓声が上がっていました。皆様最終的には自然放射線を観察することができました。



播磨高原東中学校での出前授業の様子

10月22日 関西光科学研究所（木津地区） 施設公開

新型コロナウイルス感染予防対策のため、2022年度も前年度に続いて事前予約制での開催とはなりましたが、200名を超える方々にお越しいただきました。

光の実験ショー、光に関する工作教室や専門家によるサイエンスセミナー、世界トップクラスの高強度レーザーの施設見学、レーザー打音トラック展示・模擬実験やプラネタリウム鑑賞など、ご来場いただいた皆様には好評をいただきました。また、今年度は大阪科学技術センター様にもご協賛いただき、「オーロラエッグ工作」をご出展いただきました。



工作教室



ふおとん君も大活躍



サイエンスセミナー

2月1日～3日「第22回国際ナノテクノロジー総合展・技術会議（nano tech 2023）」の MATERIAL 先端
リサーチインフラ事業ブースに説明員派遣（東京ビッグサイト）



第22回国際ナノテクノロジー総合展・技術
会議（nano tech 2023）の MATERIAL 先端
リサーチインフラ事業ブース



技術スタッフ表彰式、秀でた利用成果発
表会の様子

プレスリリース（研究成果）

1. 光と加熱で、金属と絶縁体を行ったり来たり
—高性能な光応答イットリウム化合物薄膜を世界で初めて作製—（2022年4月7日）
<https://www.qst.go.jp/site/press/20220407.html>
論文タイトル：Repeatable Photoinduced Insulator-to-Metal Transition in Yttrium Oxyhydride Epitaxial Thin Films
2. 世界トップクラス超高強度レーザーの劇的な性能向上に成功！
—レーザーによる夢の超小型加速器実現へ前進—（2022年8月4日）
<https://www.qst.go.jp/site/press/20220810-2.html>
論文タイトル：“Characterization of plasma mirror system at J-KAREN-P facility”
3. ～人の手に頼らないロボット点検技術へのイノベーション～
『レーザー打音検査装置』の社会実装を鉄道トンネルへ拡大（2022年8月9日）
<https://www.qst.go.jp/site/press/20220809.html>
4. 強力なレーザーを使ってエネルギーがそろった純度100%の陽子ビーム発生に成功
—レーザー駆動陽子ビーム加速器の実現へ向けて大きく前進—（2022年10月12日）
<https://www.qst.go.jp/site/press/20221012.html>
論文タイトル：Laser-driven multi-MeV high-purity proton acceleration via anisotropic ambipolar expansion of micron-scale hydrogen clusters

5. 最大性能の巨大負熱膨張物質
—材料組織観察の結果を用いた物質設計— (2023年1月23日)
<https://www.qst.go.jp/site/press/20230123-2.html>
論文タイトル: Polar-Nonpolar Transition Type Negative Thermal Expansion with 11.1% Volume Shrinkage by Design

6. 光が金属の中を突き進む!
—相対論効果が拓くレーザーイオン加速の新世界— (2023年3月16日)
<https://www.qst.go.jp/site/press/20230316.html>
論文タイトル: Enhanced ion acceleration from transparency-driven foils demonstrated at two ultraintense laser facilities

7. ～人の手に頼らないロボット点検技術のイノベーション～
『レーザー打音検査装置』のタイルパネル診断支援への拡大 (2023年3月28日)
<https://www.qst.go.jp/site/press/20230328.html>

その他のトピックス

2023年3月13日

【平野理事長退任記念植樹式】

量研の初代理事長である平野俊夫理事長が今年度末で任期を迎えるにあたり、理事長ご参列の下、関西研(木津地区)で植樹と銘板の除幕を行いました。当日は直前まであいにくの雨模様ではありましたが、式直前には雨が止み、無事、式を実施することができました。平野前理事長、7年間のご指導ありがとうございました。



銘板の除幕



土やり

2023年3月31日

【関西研（木津地区）北側構内道路保全対策工事の完了】

令和3年に構内道路の不陸改修のため、アスファルトを撤去したところ地割れが確認され、調査の結果、地下水脈の存在と軟弱地盤層が確認されました。北側構内道路は木津川市道に面しており、大雨や地震による市道への土砂流出が懸念されるため、軟弱地盤を補強するための地盤改良と地下水排水のための集排水管を新たに設置する保全対策工事を実施しました。工事後は地下水が継続的に排水されており、構内のハンドホール内においても水位の低下を確認しています。本工事の実施により、土砂流出を未然に防ぎ関西研のみならず近隣住民の安全確保に繋がることを期待します。



法面

北側構内道路

地下水排水状況

工事完了後写真（撮影日 2023.4.20）

User Facilities

主要な施設・装置

木津地区

○J-KAREN-P レーザー装置

【装置概要】

世界トップクラスの極短パルス超高強度レーザーです。最大 30 J のレーザーエネルギーを 30 フェムト秒 (1 フェムトは 1000 兆分の 1) の時間に閉じ込めることにより 1000 兆ワットの超高強度を実現します。

(右の写真は強力な励起レーザーの光で緑色に光っています。)



【供給装置性能】

- ・ 中心波長：810 nm
- ・ 繰り返し：シングルショット～0.1 Hz
- ・ ターゲット照射エネルギー：～10 J/pulse
- ・ パルス幅：30～50 フェムト秒
- ・ 集光強度： $10^{20}\sim 10^{22}$ W/cm²
- ・ 時間コントラスト比：<math><10^{-11}</math> (プラズマミラー不使用時)
<math><10^{-13}</math> (シングルプラズマミラー使用時)
<math><10^{-15}</math> (ダブルプラズマミラーへアップグレード予定)

上記以外のパラメータはお問い合わせ下さい。

【主要な研究課題】

超高強度レーザー高度化技術開発、イオンや電子の加速技術開発、高輝度 X 線等の量子ビーム源開発

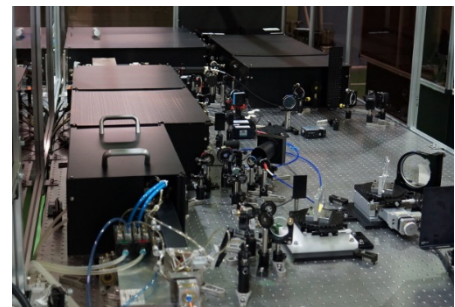
○QUADRA-T レーザーシステム

【装置概要】

1 秒間に 3000 発のレーザーパルスが繰り返し出せる高平均出力ピコ秒パルスレーザーです。

【装置性能】

- ・ 照射エネルギー：10 mJ/pulse
- ・ 波長：1030 nm
- ・ 繰り返し：3 kHz
- ・ パルス幅：約 1 ピコ秒



【主要な研究課題】

高繰り返し高出力レーザー (パラメトリック増幅器等) の開発、高強度テラヘルツ光源の開発

播磨地区

播磨地区では大型放射光施設 SPring-8 に 2 本の量研専用ビームラインを設置しているほか、日本原子力研究開発機構 (JAEA) の専用ビームラインにも複数の放射光専用実験装置を常設しています。一方で、量研専用ビームラインにも、JAEA の専用実験装置が常設されています。

○BL11XU (QST 極限量子ダイナミクス I ビームライン)

【装置概要】

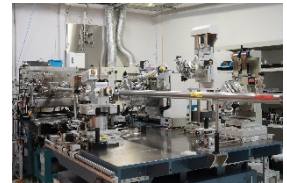
SPring-8 標準の真空封止アンジュレータを光源とし、マルチ結晶交換システムを装備することで、広範囲のエネルギー領域の高輝度放射光 X 線を高効率に利用できるビームラインです。

【装置性能】

- ・光源：真空封止アンジュレータ
- ・エネルギー領域：6~70 keV
- ・分光結晶：Si(111)、Si(311)
- ・実験装置：放射光メスバウアー分光装置、共鳴非弾性 X 線散乱装置、及び表面 X 線回折計

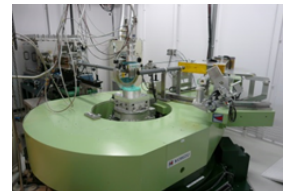
1. 放射光メスバウアー分光装置

^{57}Fe 、 ^{61}Ni 等のメスバウアー核種を対象とした放射光メスバウアー分光が可能で、物質の電子、磁気状態から格子振動状態に関する情報などを得ることができます。更に、斜入射法や同位体置換試料を利用する事で、金属薄膜の表面部を原子層単位で測定する事も可能です。



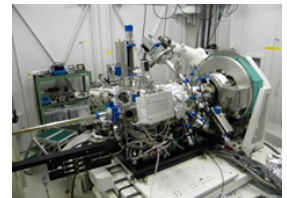
2. 共鳴非弾性 X 線散乱装置

入射 X 線、散乱 (発光) X 線の双方のエネルギーを 0.1 eV 程度のエネルギーで分光実験が可能な装置です。4 軸回折計配置で共鳴非弾性 X 線散乱により電子励起の運動量依存性が測定できるほか、高エネルギー分解能 X 線吸収分光、X 線発光分光の実験も可能です。試料温度は 10 K から 800 K まで可変です。



3. 表面 X 線回折計

分子線エピタキシー (MBE) チェンバーを搭載した表面構造解析用 X 線回折計です。半導体量子ドットや半導体多層膜などの成長過程を X 線回折によりその場観察・リアルタイム観察が可能です。2 台の MBE を交換し、GaAs、InAs などのヒ素化合物成長と RF-MBE による GaN、InN などの窒化物半導体成長を行うことができます。



【主要な研究課題】

金属薄膜の原子層単位での磁性探査、遷移金属化合物における電荷・スピン・軌道励起の観測、触媒や電池電極材料のオペランド電子状態解析、半導体量子ドットや半導体多層膜の成長過程のリアルタイム解析

○BL14B1 (QST 極限量子ダイナミクスⅡビームライン)

【装置概要】

偏向電磁石を光源とすることで、連続スペクトルを持つ白色 X 線や高エネルギーの単色 X 線が利用可能なビームラインです。全反射ミラーや分光結晶の曲げ機構によって、試料位置への集光が可能となっています。

【装置性能】

- ・光源：偏向電磁石
- ・エネルギー領域：白色 X 線 (5~150 keV)、単色 X 線 (5~90 keV)
- ・実験装置：高温高压プレス装置、汎用四軸 X 線回折計及び分散型 XAFS 測定装置 (JAEA)

1. 高温高压プレス装置

10 GPa (13 万気圧)、2300 K 程度までの圧力・温度状態下の試料を、白色 X 線を用いたエネルギー分散型 X 線回折法やラジオグラフィ法、単色 X 線を用いた XAFS (X 線吸収微細構造) 法や角度分散型 X 線回折法等によって調べることができます。

【主要な研究課題】 高压下での金属水素化物形成過程のその場観察



2. 汎用四軸 X 線回折計

令和 2 年 3 月に RI 実験棟から移設。X 線照射位置を可視化するためのレーザーを整備しており、がん研究等のための単色 X 線を利用した照射実験に使用できます。高エネルギー単色 X 線を利用した回折法により、大型構造材料中の応力・ひずみ、結晶方位分布計測の測定も可能です。

【主要な研究課題】 応力・ひずみ、結晶方位の三次元分布測定、及び照射実験等



○BL22XU (JAEA 専用ビームライン) における放射光専用実験装置

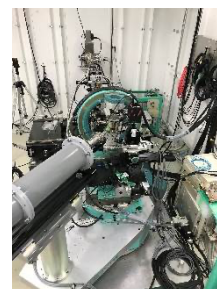
1. 高速 2 体分布関数計測装置 (旧ダイヤモンドアンビルセル回折計)

最高 70 keV の高エネルギー X 線と大型二次元 X 線検出器の利用により最大 $Q = 27 \text{ \AA}^{-1}$ までの X 線全散乱プロファイルが迅速に得られ、約 100 \AA までの距離相関の原子二体分布関数が導出できます。専用アタッチメントにより、室温、1 MPa 未満の水素と窒素ガス雰囲気でのその場観察ができます。試料-検出器間距離が可変のため高角データから高分解能データまで取得が可能であり、ダイヤモンドアンビルセルを用いた高圧力下 X 線回折測定にも適用可能です。



2. コヒーレント X 線回折イメージング装置 (旧大型 X 線回折計)

X 線領域のブラッグ反射を利用したコヒーレント X 線回折イメージングが実施できる水平振りの大型 X 線回折計です。粒径 100 nm 以下のナノ結晶ひと粒のサイズや形状、内部構造 (応力、ドメイン等) を含む 3 次元イメージングが可能です。



【主要な研究課題】

水素貯蔵合金、負の熱膨張材料、100~500 nm 級チタン酸バリウムナノ結晶粒子一粒の 3 次元可視化、40 nm 級パラジウムナノ結晶粒子一粒の 3 次元可視化

施設の稼働実績と利用状況

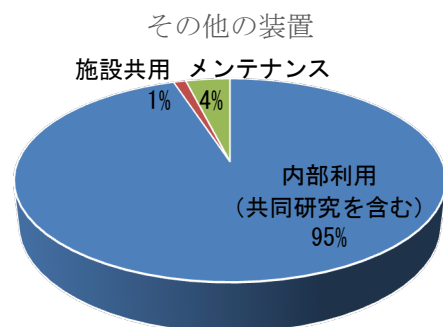
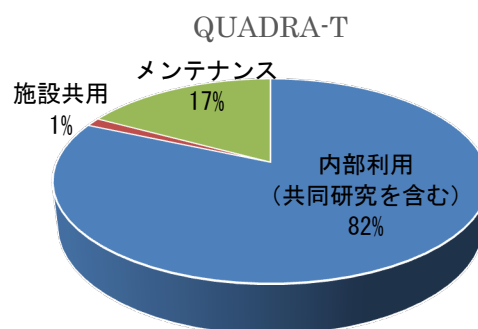
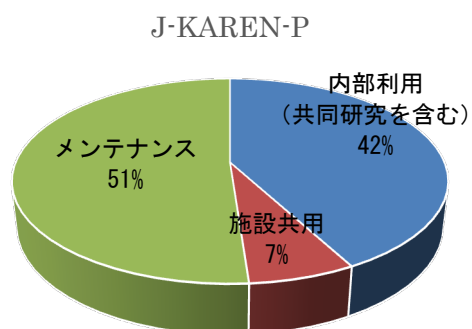
木津地区

2022年度の運転時間はJ-KAREN-Pは1771時間、QUADRA-Tは1052時間、その他装置は合計1722時間でした。J-KAREN-Pはコントラスト比を上げるためのプラズマミラーの運用を開始しました。

実施課題件数

装置名称	独自研究	受託研究	共同研究	施設共用
J-KAREN-P レーザー装置	6	0	0	6
QUADRA-T レーザーシステム	1	1	0	1
kHz チタンサファイアレーザー	5	1	1	1
X線回折装置	0	0	0	0

稼働時間内訳



播磨地区

2022年度のSPring-8蓄積リングの運転時間は5184時間で、放射光利用時間はそのうちの4440時間でした。量研、JAEAとも専用ビームラインでは10%程度の調整時間を除き、放射光利用時間で独自研究や受託研究、外部利用者への施設共用と研究支援を行っています。

実施課題件数

ビームライン	独自研究	受託研究	共同研究	施設共用
BL11XU	9	0	4	16
BL14B1	15	0	6	13
BL22XU	7	0	7	11

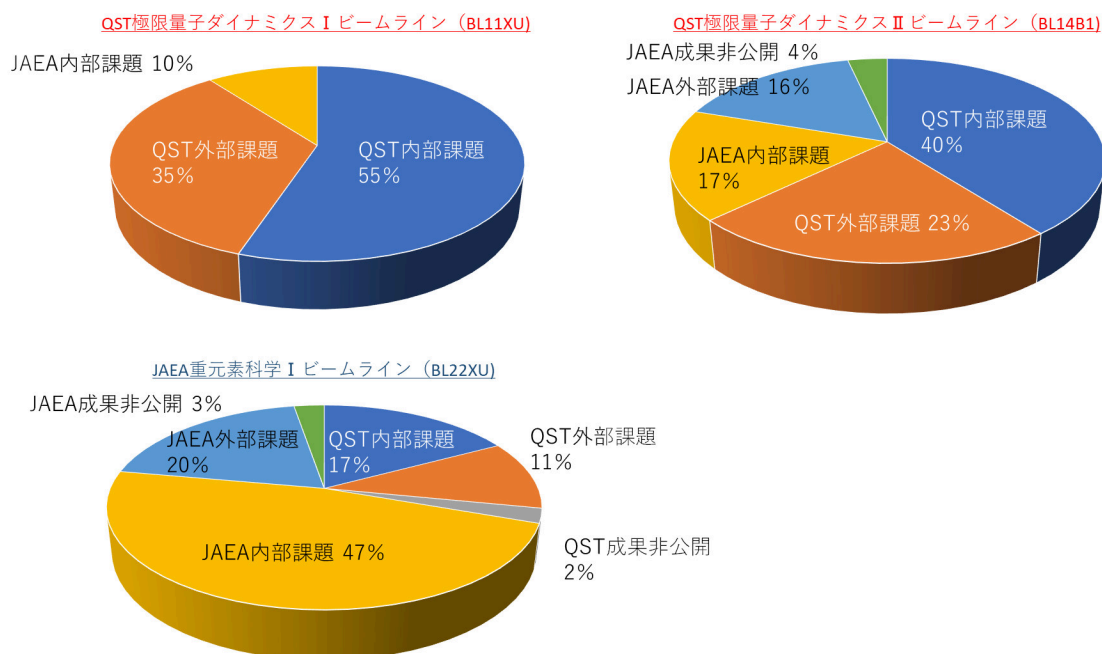
利用日数

ビームライン	独自研究	受託研究	共同研究	施設共用
BL11XU	91	0	25	57
BL14B1	68	0	26	44
BL22XU	30	0	24	23

*件数、日数ともに量研の利用課題のみ

*日数は3シフトを1日とした。

稼働時間内訳



Research Highlights

Advanced Photon Research Activities

KONDO Kiminori

Department of Advanced Photon Research



The science and technology related to advanced lasers is the foundation for the research conducted in the Department of Advanced Photon Research. Advanced laser development is the basic focus area of this department. Laser technologies producing high peak power, high repetition rate, and high stability, and ultrashort-pulse technologies are of particular importance. We develop these technologies in-house and apply them in various projects.

The largest laser system in KPSI is the petawatt (PW)-class high-peak-power J-KAREN-P laser. This system was upgraded in FY2012 after obtaining supplementary budget. After a long commissioning operation term, internal users in KPSI and external users have been allowed to use this system in the PW-class operation mode. Moreover, from FY2021, the large-aperture plasma mirror system (PM) has also been opened to users, which helps avoid the unnecessary rising part of the femtosecond high-peak-power pulse, which is a serious problem associated with laser-driven ion acceleration with a nanometer-thin foil target. However, the other upgrade, the so-called “digital transformation (DX)” has also been funded for the Advanced Photon Science Facility, which includes J-KAREN-P. Although the machine time with PM for the users started in September 2021, J-KAREN-P was not operational from April to July, owing to upgradation including DX, in FY2022. With DX, the improvement in the PM was successfully demonstrated. We expect good results in the J-KAREN-P experiments using the improved PM system. Dr. Nishiuchi, of the high-intensity laser science group, has reported the progress of laser-driven ion acceleration experimental studies at two ultra-intense laser

facilities, KPSI and HZDR (Helmholtz-Zentrum Dresden-Rossendorf), in Germany. Her report is related to the installation of a high-quality PM system in J-KAREN-P; however, the improved PM is not described in this report. Ion acceleration in relativistically transparent plasma with a nano-thickness foil target has been observed with high-quality intense laser pulses, even without PM. She explains the importance of suppressing the unnecessary rising part of the PW laser pulse.

The exemplary status of our high-power laser infrastructure is maintained by the laser facility operation office, advanced laser group, and high-intensity laser science group. The advanced laser group not only maintains J-KAREN-P to deliver laser pulses with the best conditions but also develops and introduces new technologies to maintain the global first-class status of J-KAREN-P.

One of the most important applications is the development of laser-driven quantum beams. The applications of J-KAREN-P in KPSI include laser-driven ion acceleration, laser electron acceleration, and relativistic high-order harmonic generation. An extremely high optical field can be formed by focusing an extremely high peak power to an ultimately small spot size. While the corresponding optical intensity of the atomic unit is only 3×10^{16} W/cm², the extremely high field corresponds to up to 10^{22} W/cm² in intensity with J-KAREN-P. The irradiated atoms and molecules are then immediately ionized to generate free electrons, which move along this extremely high optical field, inducing the so-called ultrarelativistic quiver motion. These energetic electrons generate various secondary radiation sources, which

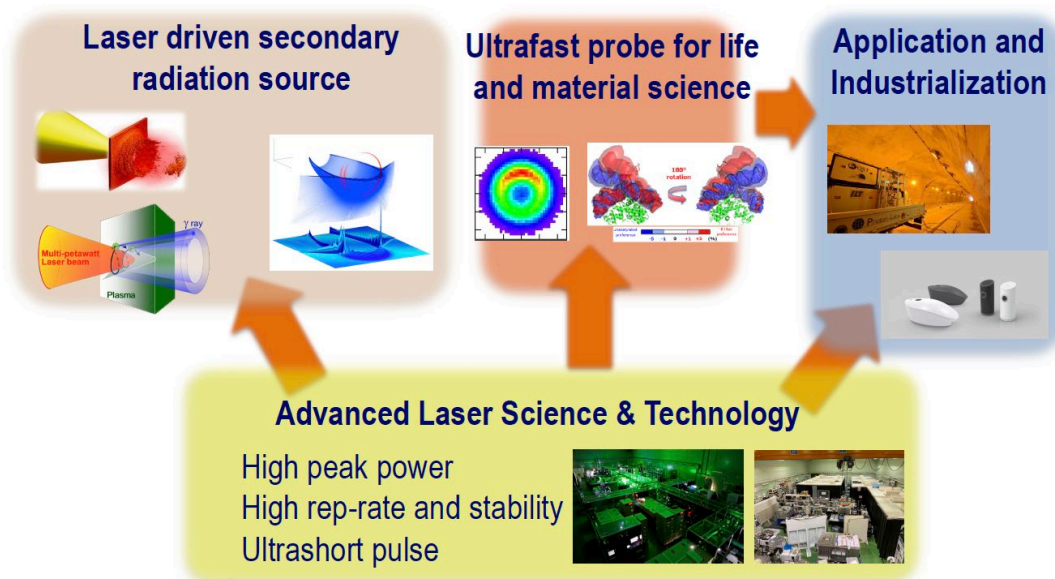


Fig.1 Research and development activities of the Department of Advanced Photon Research.

indicates the possibility of a compact energetic quantum beam source without a conventional accelerator. If this technology is established and applied to various fields, a type of destructive innovation can occur. For this purpose, special technologies must be developed for stable quantum beam generation and precise observation of extreme plasma behavior. Dr. Nakanii, of the high-intensity laser science group, reported precise pointing control of high-energy electron beams from laser wakefield plasmas. He simply placed and moved a serrated aperture before a large off-axis parabolic mirror, which was used to focus the high-peak-power laser pulse to the gaseous target. This simple technology has also been used in other facility for laser electron acceleration studies. At this facility, stable pointing for laser-accelerated electrons has successfully been demonstrated. Dr. Pirozhkov, of the advanced laser group, reported enhanced relativistic plasma diagnostics with ultrashort probe pulses. He has been developing an ultrashort probe pulse to freeze high-speed plasma fluids, which generate high-order harmonics. This high-harmonic generation (HHG) is unique. Although the usual HHG emitted from neutral atoms and molecules at the irradiation intensity is around the field ionization threshold, his HHG is far beyond this threshold in the relativistic field. This means that a much shorter wavelength HHG is possible, although the usual HHG has a limited ionization threshold. However, the high-speed plasma fluid-emitting HHG has almost never been observed. He is now developing a unique diagnostic tool for observing plasma using the Schlieren method. Related to the usual HHG, Prof. Nanba at Hiroshima University and Dr. Dinh in the X-ray laser group have reported the nonlinear propagation effect in X-ray parametric amplification during HHG.

Although there are no precise reports in this annual report, one of the most important applications of laser-driven energetic particles is the application to the Quantum Scalpel, which is a new-generation heavy-ion cancer-therapy machine. Quantum Scalpel is one of the main projects of QST. The injector part of Quantum Scalpel is based on a laser-driven carbon accelerator. The large-scale JST-MIRAI R&D program (large-scale type) started in November 2017. The aim of this program is to demonstrate the proof of concept (POC) of a laser plasma accelerator. In addition to an ion accelerator, a laser plasma electron accelerator is also under development in KPSI, under the MIRAI program. The POC of the laser-driven heavy-ion injector will be demonstrated by the end of FY2026. In FY2020, the first-stage gate was successfully passed. FY2022 witnessed the second stage of JST-MIRAI. In 2022, a high-repetition-rate tape target for pure carbon-ion generation was developed with a collaboration of Hitachi Zosen. The invented technology was submitted for a patent. The beam line for estimating the number of energetic carbon ions with a finite solid angle was estimated to

be set in the ion acceleration platform with a collaboration of the Sumitomo Heavy Industry. In the next fiscal year, FY2023, the second-stage gate exam will be held for the JST-MIRAI. Currently, the development of related technologies is being vigorously pursued.

Another important application of advanced laser science and technology is ultrafast probes for life and material sciences. The ultrafast dynamics group not only studies the basic science of ultrafast molecular behavior but has also developed a unique ultrafast high-power laser system. The ultrafast dynamics group is developing and improving the over-kHz-repetition-rate high-average-power ultrashort laser system, QUADRA-T. Recently, this system has been improved using a high-quality thin-disk Yb:YAG amplifier. This system is used as the pumping source for a mid-infrared high-average-power laser, which will be used for shorter-wavelength HHG. In addition to HHG, a laser system has been used to study the ultrafast dynamics of energy states, including that of biomolecules. Dr. Tsubouchi reported beat-frequency-resolved two-dimensional electron spectroscopy. With his high-level diagnostics, the ultrafast changes in the energy states of the biomolecules can be observed, which introduces new findings not only in the material science but also life science fields, which is a collaborative study with the Institute of Quantum Life Science in QST. The laser systems developed in the ultrafast dynamics group will be used for laser fabrication and ultrafast laser science, which are studied in the Q-LEAP program at JST. Dr. Yamada reported a theoretical approach for elucidating the propagation effects in HHG from solids, which is related to attosecond science in the Q-LEAP project. Moreover, Dr. Aoyama reports the application of mid-infrared microscopic imaging techniques to histopathological analysis, which is also a collaborative study with the Institute of Quantum Life Science in QST.

The most important application of our advanced laser science and technology is industrialization. In the SIP program, a nondestructive tunnel-inspection technology is under development in the X-ray laser group. This technology is being tested for application in commercial technology at the venture company Photon-Labo. Nondestructive tunnel inspection is possible using laser-hammering technology. The laser-hammering technology is expected to be useful for inspecting not only tunnels but also various concrete structures. Dr. Sasaki of the X-ray laser group has also reported the modeling of the wavelength of unresolved transition arrays in an EUV laser plasma light source, which is related to EUV lithography technology.

Enhanced ion acceleration using transparency-driven foils demonstrated in two ultraintense laser systems

NISHIUCHI Mamiko

High-Intensity Laser Science Group, Department of Advanced Photon Research



The advent of reliable, high-quality, and high-power lasers has facilitated rapid technological progress, with their application in particle acceleration [1]. The development of ultrashort high-peak-current laser-driven ion sources has benefit in the delivery of ultraintense laser pulses combined with conceptual breakthroughs in controlling the interactions of extreme electromagnetic fields with matter [2]. The unique properties of laser-accelerated ion beams have motivated numerous applications, including radiography injectors for accelerators [3, 4] and high-dose-rate radiobiology [5].

Target normal sheath acceleration (TNSA) is a robust technique for generating energetic ions through laser irradiation [6]. However, this mechanism's modest intensity scaling [7] makes it challenging to further increase the beam energy.

Advanced acceleration schemes promise higher ion energies when using ultraintense pulses, such as light-sail radiation pressure acceleration (LS-RPA) [8]. However, LS-RPA requires an opaque ultrathin target (thickness $d \ll 100$ nm); thus, an ultrahigh laser temporal contrast, the ratio of intensities between the main pulse and preceding light. Even state-of-the-art lasers have a finite contrast laser pulse, which causes heating of the target electrons and rapid expansion of the target. The electron density n_e drops below the relativistically corrected critical density $n_{cr} = \gamma n_c$, where γ is the electron Lorentz factor and $n_c = m_e \omega_L^2 / 4\pi e^2$ is the classical critical density (m_e and ω_L are the electron mass and laser frequency, respectively), resulting in laser propagation through the target in the relativistically induced transparency (RIT) regime.

However, it has been shown that for targets driven in the RIT regime can also generate high ion energies [9,10], but the way how to trigger the RIT for efficient ion acceleration is not obvious.

The experiment was conducted using the J-KAREN-P laser at the Kansai Photon Science Institute [11] and Draco-PW laser system at the Helmholtz-Zentrum Dresden-Rossendorf [12]. The effect of changing the target thickness on ion acceleration was investigated after the laser temporal pulse contrast conditions of the two systems were adjusted to be identical. The experimental setup is shown in Fig. 1(a). Laser pulses with 10 (15) J on-target energy and 45 (30) fs full-width-at-half-maximum (FWHM) duration for J-KAREN-P (Draco-PW) were focused onto plastic targets placed at 45° to the incident laser [13]. The focal spot diameter was ≈ 1.5 (2.6) μm FWHM, resulting in a peak intensity of 3.5 (5) $\times 10^{21}$ W/cm² for J-KAREN-P (Draco-PW).

The maximum detected energy of the proton and the energy of the 1ω transmitted laser light (ϵ_{trans}) are plotted in Fig. 1(b), as functions of the initial target thickness d . Similar ion-acceleration performances were produced in both systems. There is an optimal thickness $d_{opt} \approx 250$ nm, where the energies of both species are maximized, reaching $E_{m,p} > 60$ (80) MeV for protons in J-KAREN-P (Draco-PW). In the J-KAREN-P system, an $E_{m,c} > 30$ MeV/u was obtained for carbon with the optimum target thickness. Thinner or thicker targets resulted in lower

energies.

The amount of transmitted light also indicated a clear thickness dependency. While targets with $d > 300$ nm exhibited a constant and nearly negligible amount of transmitted light ($\epsilon_{trans} < 30$ mJ $\approx 0.3\%$ of input energy), the transmission increased exponentially for thinner targets and reached $\epsilon_{trans} \gg 500$ mJ ($> 5\%$ of input energy) for $d < 200$ nm. This sudden increase in the transmission for target thicknesses between 200 and 300 nm indicated a pronounced decrease in the peak density of the targets at the time of the main pulse arrival. There was a clear correlation between the onset of transparency and the significant increase in the generated beam energies. However, for very thin targets with high transmission, the ion energy decreased. The measurable, but relatively low, transmission for optimum ion energies indicated the efficient conversion of laser energy in the transparent, but still dense, target.

Understanding the pre-expansion of the target is essential for elucidating the high-intensity laser-plasma interactions at the peak of the pulse. We implemented a two-stage simulation method, performing hydrodynamic simulations of the low-intensity rising edge after laser induced breakdown (LIB) followed by 3D particle-in-cell (PIC) simulations of the final high-intensity ramp and main pulse using the FLASH and EPOCH codes respectively. The timing of LIB is determined experimentally by Draco-PW laser system [14].

The variations in E_m and ϵ_{trans} with changing d , from the two-stage simulations are shown overlaid (circles) on the experimental data, in Fig. 1(b). There is good agreement with the experimental results over the entire thickness range. The simulations exactly reproduce the optimum target thickness and maximum ion energy.

To identify the ion acceleration process for the optimum thickness, we describe the main pulse interaction with the pre-expanded plasma for $d = d_{opt} = 250$ nm. The laser was strongly absorbed by the opaque plasma during the femtosecond rising edge before the peak of the pulse. The ultrahigh intensities resulted

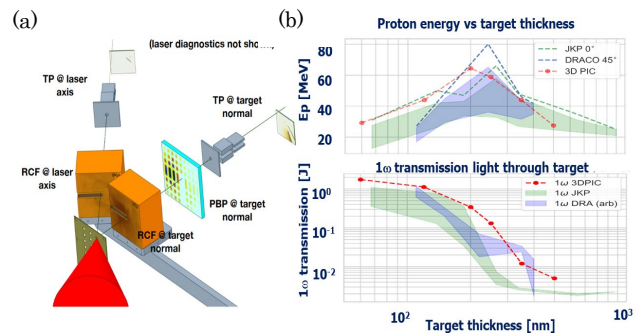


Figure.1 (a) Experimental setup at both laser systems. (b) Accelerated proton energy at J-KAREN-P (green) and Draco-PW (blue) dependency on the target thickness. The dotted line shows the peak value, while the shaded regions show the 1-sigma region from the mean values. The red data points show the simulation results.

in strong $v \times B$ radiation pressure, bunching, and acceleration of the electrons along the laser axis. A two-dimensional (2D) slice from the simulation, at the peak of the pulse, is shown in Fig. 2(a). The electrons at the center of the target were heated and expanded such that $n_c < n_e < n_{cr}$, and the laser began to penetrate the target. The laser interacted volumetrically with the target electrons, leading to strong absorption, resulting in $v \times B$ driven electrons being rapidly expelled from the focal region. Because the ions were not significantly accelerated by the laser fields, owing to their lower charge-to-mass ratios, a region of large space charge developed in the transparent region, highlighted by the green box. This space charge was maintained by the continuous expulsion of electrons owing to radiation pressure. Although the expulsion of electrons was not complete, the magnitude of the time-averaged space charge could reach $\langle \rho \rangle > 10enc$, which resulted in a region of large cycle-averaged quasi-static electric field $\langle E_x \rangle \sim 30$ TV/m, with a spatial extent of $\sim 500 \times 500 \times 500$ nm³ (see inset in Fig. 2).

Our results demonstrate that having relativistic transparency occur at the peak of the pulse is strikingly beneficial. Here, however, during the ultraintense femtosecond pulse interaction, the largest accelerating gradients and energy gain dominantly arises from significantly higher space charge fields resulting from electron expulsion from the relativistically transparent target core.

The RIT-enhanced acceleration mechanism described herein is a promising regime for application-oriented high-energy ion acceleration. In contrast to the recent efforts to use plasma mirrors to minimize the prepulse of high-power femtosecond lasers to enable the irradiation of targets with a

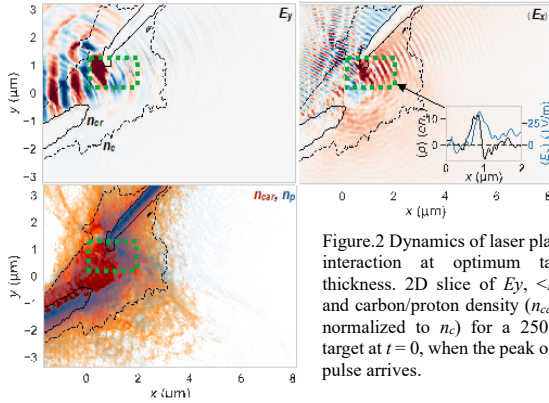


Figure 2 Dynamics of laser plasma interaction at optimum target thickness. 2D slice of E_y , $\langle E_x \rangle$, and carbon/proton density ($n_{car, p}$ normalized to n_c) for a 250 nm target at $t = 0$, when the peak of the pulse arrives.

thickness of a few nanometers, we show that these lasers can be used in different acceleration regimes with relaxed contrast requirements. This not only significantly reduces the complexity, size, and cost of the ion source but also removes the limitation of continuous high-repetition-rate operation. The required target thickness, of a few hundred nanometers, improves the robustness, compared to the $d \sim 10$ nm targets required for LS-RPA in the same intensity range, which are easily damaged during handling, pump down, or by preceding shots on the target system.

The similarity in the results from the J-KAREN-P and DRACO-PW systems, despite different laser front-end configurations and slightly different focal-spot parameters, reveals the robustness of the regime. Our investigation of the prepulse-induced density shaping and acceleration mechanism implies that the laser contrast and intensity are the most important factors that determine the optimal target thickness for this regime. The laser contrast determines the target density at the peak of the pulse for a given target thickness, whereas the laser intensity determines the density required for relativistic transparency.

In summary, we investigated the ion acceleration due to the interaction of an ultraintense femtosecond laser pulse with thin

CH foils and found an optimized target thickness for the acceleration of protons (carbon ions) > 60 MeV (> 30 MeV/u). We determined that the laser prepulse played an essential role in priming the plasma density for relativistic transparency. The acceleration of the highest-energy ions was due to a strong space-charge field generated by the expulsion of electrons during RIT, followed by further acceleration in an ambient sheath. Our reproduction of the acceleration regime, with two different lasers, underlines its robustness and demonstrates that plasma mirrors and ultrathin nanometer-scale targets are not necessarily required for high-energy ion acceleration using femtosecond-class laser systems. This conceptual breakthrough establishes a path toward the development of ~ 100 MeV class repetitive ion sources using the currently available laser technology.

Acknowledgments

The author is grateful to all the co-authors of reference [13], J-KAREN/Draco laser operation team, and KPSI staff. This work was partially supported by Kakenhi Grant No. 22H00121, Grant No. 21KK0049, and the QST President's Strategic Grant (QST International Research Initiative (AAA98) and Creative Research (ABACS)).

References

- Albert, F. *et al.* 2020 roadmap on plasma accelerators. *New Journal of Physics* **23**, 031101 (2021).
- Daido, H., Nishiuchi, M. & Pirozhkov, A. S. Review of laser-driven ion sources and their applications. *Reports on Progress in Physics* **75**, 056401 (2012).
- Aymar, G. *et al.* LhARA: The laser-hybrid accelerator for radiobiological applications. *Frontiers in Physics* **8**, 567738 (2020).
- Nishiuchi, M. *et al.* Dynamics of laser-driven heavy-ion acceleration clarified by ion charge states. *Physical Review Research* **2**, 033081 (2020).
- Kroll, F. *et al.* Tumour irradiation in mice with a laser-accelerated proton beam. *Nature Physics* **18**, 316 (2022).
- Clark, E. L. *et al.* Energetic heavy-ion and proton generation from ultraintense laser-plasma interactions with solids. *Physical Review Letters* **85**, 1654 (2000).
- Dover, N. P. *et al.* Effect of small focus on electron heating and proton acceleration in ultra-relativistic laser-solid interactions. *Physical Review Letters* **124**, 084802 (2020).
- Esirkepov, T., Borghesi, M., Bulanov, S. V., Mourou, G. & Tajima, T. Highly efficient relativistic-ion generation in the laser-piston regime. *Physical Review Letters* **92**, 175003 (2004).
- Higginson, A. *et al.* Near-100 MeV protons via a laser-driven transparency-enhanced hybrid acceleration scheme. *Nature Communications* **9**, 724 (2018).
- Jung, D. *et al.* Laser-driven 1 GeV carbon ions from preheated diamond targets in the break-out after-burner regime. *Physics of Plasmas* **20**, 083103 (2013).
- Kiriyama, H. *et al.* Enhancement of pre-pulse and picosecond pedestal contrast of the petawatt J-KAREN-P laser. *High Power Laser Science and Engineering* **9**, e62 (2021).
- Ziegler, T. *et al.* Proton beam quality enhancement by spectral phase control of a PW-class laser system. *Scientific Reports* **11**, 7338 (2021).
- Dover, N.P. *et al.* Enhanced ion acceleration from transparency-driven foils demonstrated at two ultraintense laser facilities. *Light Science and Applications* **12**, 71 (2023).
- Haffa, D. *et al.* Temporally Resolved Intensity Contouring (TRIC) for characterization of the absolute spatio-temporal intensity distribution of a relativistic, femtosecond laser pulse. *Scientific Reports* **9**, 7697 (2019).

Beam stabilization of laser plasma accelerator by shaping the laser near-field profile

NAKANII Nobuhiko



High-Intensity Laser Science Group, Department of Advanced Photon Research

Ever since laser wakefield acceleration (LWFA) concept was proposed by Tajima, the former Director General of KPSI, and Dawson in 1979 [1], a laser-plasma accelerator, which has an acceleration gradient that is thousand times higher than that of conventional accelerators, has been studied and developed as a next-generation compact accelerator [2-6]. The maximum energy of the LWFA electron beam have already achieved to be 8 GeV [7]. Recently, as one of the milestones in this research area, self-amplified spontaneous emission (SASE) free-electron laser (FEL) has been demonstrated by Chinese group [8], and seeded FEL has been demonstrated by a group of French and German researchers[9]. In Japan, we have a similar project to demonstrate FEL with wavelengths around extreme ultraviolet (XUV) and vacuum ultraviolet (VUV) in the JST MIRAI program [10].

The stability of electron beams is crucial for the practical application of laser-plasma accelerators, such as FELs. Here, we focus on the pointing stability. If the pointing of the beams is unstable, the electron beam cannot be transported to the beamline and guided to the undulator. The stability of the LWFA beams, including the pointing stability, can be improved by stabilizing the laser system and choosing appropriate injection methods. However, the cause of the instability of the LWFA electron beams still needs to be clarified. The typical pointing fluctuations of the electron beams observed in the experiments are three times larger than those of the driving laser pulses.

In our experiment, we succeeded in stabilizing the electron beams by simply placing an aperture in the laser transport line before the focusing element, that is, an off-axis parabolic mirror (OAP). Shaping the near-field profile (NFP) of the laser pulse with the aperture removes the outer part of the laser pulse with unstable wavefront and intensity. This improves the quality and stability of the focusing laser pulse, and thus, the electron beam generated by this laser pulse also becomes stable. This simple method is expected to be a key technique for realizing an ultracompact accelerator with LWFA, in the future[11].

The experiment was performed with J-KAREN-P at KPSI. J-KAREN-P is a high-contrast petawatt-class Ti:Sapphire laser system using optical parametric chirped-pulse amplification [12-14]. The central wavelength was around 810 nm and the contrast ratio between the main pulse and nanosecond prepulse caused by amplified spontaneous emission (ASE) was better than 10^{-11} . The experimental schematic is shown in Fig. 1(a). In this experiment, the laser system delivered ~ 8.5 J of pulse energy on the target with a pulse duration of 44 fs full-width-at-half-maximum (FWHM). The laser pulse was focused onto a supersonic gas jet by an OAP with a 2.6 m focal length, to excite a laser wakefield and produce high-energy electrons.

A supersonic hydrogen-based gas mixture was expelled from a rectangular slit nozzle with a length of 1 cm and width of 1.2 mm. A density ramp was created by inserting a razor blade into the gas flow at the nozzle exit to induce the injection of electrons into the laser wakefield due to the breaking of plasma wave at the density boundary [15]. Moreover, the gas included 0.5% nitrogen in hydrogen to inject electrons into the wakefield effectively via

the ionization injection scheme [16]. The typical inlet pressure of the gas was around 0.6 MPa.

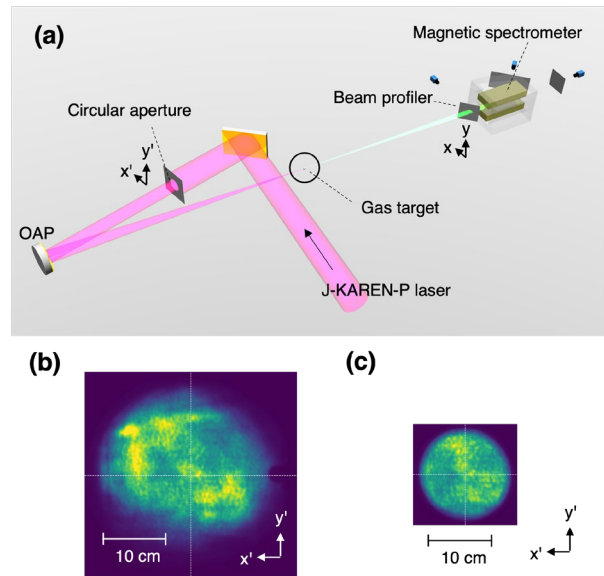


Fig. 1 (a) Experimental setup for stabilization of the LWFA electron beams by laser profile shaping with an aperture. (b) Original NFP of J-KAREN-P before OAP. (c) NFP shaped with an aperture with the same scale as (b).

The aperture used to shape the NFP of the laser pulse was a thin metal plate with an open diameter of ~ 13 cm, which was placed upstream of the OAP. By shaping the NFP with the aperture, the F-number of this focal system was increased to approximately 20 from the original F-number of 10. The NFPs of the laser pulse at the OAP without and with the aperture are shown in Fig. 1 (b) and (c), respectively. The energy of the laser pulse with the aperture was approximately 3 J at the target. The wavefront of the laser pulse was optimized to be flat by using a deformable mirror, with roughness of less than 80 nm (rms) for the full beam.

The electron beam produced by the LWFA was irradiated onto a phosphor ($Gd_2O_2S:Tb$) screen located 1.9 m from the gas target, and the fluorescence from the screen was detected using a charged-coupled device (CCD) to evaluate the beam profile of the electron beam. After passing through the phosphor screen as the beam profiler, the electron beam was bent by a 0.75 T permanent dipole magnet with a 10 cm gap and detected by other phosphor screens with CCDs, to evaluate the electron energy spectrum.

Figure 2 shows the profiles and pointing stabilities of the laser focus spots and electron beams measured the beam profiler

in the cases with and without shaping NFP with the aperture. From Fig. 2(a)-1 and (b)-1, the effective focal spot radius without and with the NFP shaping is $\sim 9.4 \mu\text{m}$ and $\sim 12.8 \mu\text{m}$, respectively. The definition of the effective spot radius is shown in Ref. 14. The focal peak intensities with and without the NFP shaping were estimated to be $\sim 7.0 \times 10^{19}$ and 1.4×10^{19} W/cm², which correspond to the normalized laser field of $a_0 \sim 5.7$ and ~ 2.5 , respectively. The Strehl ratio was improved from 0.29 to 0.56 by shaping the NFP with the aperture. The position and pointing stability of the focal spot did not change significantly when the aperture was inserted or moved. The pointing fluctuations of the laser pulse with/without the NFP shaping were approximately $\pm 1.5 \mu\text{rad}$ (rms).

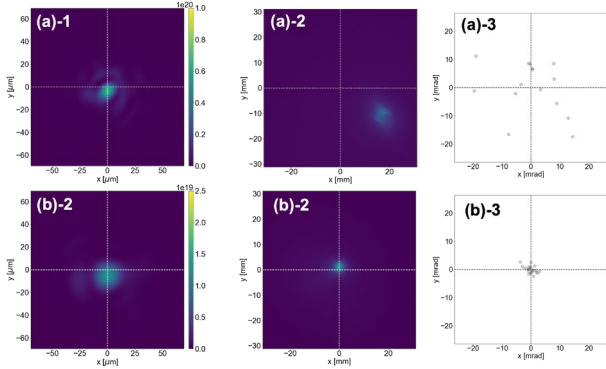


Fig. 2 Focus profiles of the laser pulses and beam profiles and pointing stabilities of the electron beam (a) with and (b) without laser-beam NFP shaping by the aperture. 1, 2, and 3 indicate the focus profiles of the laser pulses, beam profiles, and successive 20-shot pointing of the electron beams, respectively.

However, the electron-beam quality was drastically improved by shaping NFP with the aperture. One of the profiles of the electron beams is presented in Fig. 2(a)-2 and (b)-2. The intensity of the electron beam in the case with the NFP shaping was higher than that without the NFP shaping, even though the laser energy was less than half. Moreover, the generation probability and pointing stability of the electron beam were improved by shaping the NFP with the aperture. The probability of beam generation in 20 consecutive shots was 100% with the NFP shaping and 75% without the NFP shaping. The horizontal and vertical pointing fluctuations of the electron beam without the NFP shaping were ± 1.6 and ± 1.3 mrad (rms) and those with the NFP shaping were ± 9.8 and ± 8.8 mrad (rms), respectively, as shown in Fig. 2(a)-3 and (b)-3. The electron energy spectrum measured using a magnetic electron spectrometer was also stabilized using this method.

The pointing fluctuation of the laser pulses in the high-intensity laser systems is basically in the order of μrad , otherwise that of the electron beams from the LWFA is in the order of mrad. In this experiment, the pointing stability of the electron beams improved however the pointing stability of the laser pulse did not by shaping the NFP with the aperture. These facts indicate that the fluctuation of the distribution of the NFP can affect the electron pointing stability. According to the Fresnel–Kirchhoff’s law, the distribution of the intensity and wavefront at the focal point are represented by the superposition of the waves emitted from each point in the NFP. If the intensity distribution of the NFP is not uniform and the centroid of the NFP is off the center of the

NFP, the wavefront at the focal point will be tilted, with the tilt angle depending on the centroid of the NFP. Stabilizing and making the NFP of the laser pulse uniform is important for further improving the stability of LWFA electron beams. We attribute the pointing improvement to not only NFP improvement but also the increase in the F-number, and Strehl-ratio improvement. More detailed study of these improvements is left as a future task.

In summary, the shaping of the NFP of the laser pulse by installing an aperture smaller than the laser diameter before the OAP enabled the beam stabilization of high-energy electron bunches of several hundred MeV. This beam stabilization method by the NFP shaping with the aperture was simple and effective because the high-energy electron beam could be stabilized without manipulating the optics in the laser system. For future practical applications of laser plasma accelerators, such as free-electron lasers, this method could be necessary. In particular, in staging LWFA [17,18] for higher electron energy, μrad beam-control accuracy is required to inject electrons into the next laser wakefield. Further stabilization of the NFP of the laser pulse are required to improve the pointing of the electron beams.

Acknowledgments

The author would like to thank Drs. K. Huang, Ko. Kondo, I. Daito, and M. Kando for their contributions to the experiments and discussions associated with this work. The author is also grateful to the J-KAREN-P operation team, Drs. Y. Miyasaka, A. Kon, A. Sagisaka, K. Ogura, and H. Kiriyaama, for their contributions in providing the laser light for the experiments. We gratefully acknowledge Drs. J. K. Koga and Ki. Kondo, Prof. T. Hosokai of Osaka University, and Dr. Y. Sano of the Institute for Molecular Science for their fruitful discussions and encouragement. This work was funded by the JST-MIRAI program (Grant Number JPMJMI17A1). This work used research equipment shared in the MEXT Project to promote public utilization of advanced research infrastructure (Program for Advanced Research Equipment Platforms) Grant No. JPMXS0450300221. This work was partially supported by JSPS KAKENHI (Grant No. JP22K12665, JP21H01103 and JP21K17998.)

References

1. T. Tajima and J. M. Dawson, *Phys. Rev. Lett.* **43**, 267 (1979).
2. E. Miura et al., *Appl. Phys. Lett.* **86**, 251501 (2005).
3. S.P.D. Mangles et al., *Nature* **431**, 535 (2004).
4. C.G.R. Geddes et al., *Nature* **431**, 538 (2004).
5. J. Faure et al., *Nature* **431**, 541 (2004).
6. W.P. Leemans et al., *Nat. Phys.* **2**, 696 (2006).
7. A.J. Gonsalves et al., *Phys. Rev. Lett.* **122**, 084801 (2019).
8. W. Wang et al., *Nature* **595**, 519 (2021).
9. M. Labat et al., *Nat. Photon.* (2022).
<https://doi.org/10.1038/s41566-022-01104-w>
10. Y. Sano et al., JST MIRAI project “Development and demonstration of laser-driven quantum beam accelerators”
<https://lpa.ims.ac.jp/>
11. N. Nakanii et al., *Appl. Phys. Express* **16**, 026001 (2023).
12. H. Kiriyaama et al., *Opt. Lett.* **43**, 2595 (2018).
13. H. Kiriyaama et al., *Opt. Lett.* **45**, 1100 (2020).
14. A.S. Pirozhkov et al., *Opt. Express* **25**, 20486 (2017).
15. S. V. Bulanov et al., *Phys. Fluids B* **4**, 1935 (1992).
16. C. McGuffey et al., *Phys. Rev. Lett.* **104**, 025004 (2010).
17. S. Steinke, *Nature* **530**, 190-193 (2016).
18. Z. Jin et al., *Sci. Rep.* **9**, 20045 (2019).

Beat-frequency-resolved two-dimensional electronic spectroscopy with sub-10 fs visible laser pulses

TSUBOUCHI Masaaki

Ultrafast Dynamics Group, Department of Advanced Photon Research



Quantum coherence in photosynthetic proteins in solutions has recently been reported and is actively discussed.¹ A pair of photoexcited adjacent chromophores can form exciton states. When the chromophores are excited by an ultrashort laser pulse with a spectrum broad enough to cover the split energy levels of the exciton states, quantum coherence is expected to be generated in the pair of exciton states. The quantum coherence in photosynthetic proteins has been suggested to be related to the unidirectional energy flow with extremely high efficiency, which occurs during photosynthesis.² However, quantum coherence during photosynthesis has not yet been confirmed.

Two-dimensional electronic spectroscopy (2D-ES) has been used to analyze this problem. 2D-ES can spectrally resolve quantum states that cannot be resolved using conventional spectroscopic techniques, owing to the inhomogeneous broadening that occurs in solution; it can also map the correlation between states.^{1,3} Measurement of the correlation map, as a function of the pump-probe delay, reveals a reaction pathway from a specific state excited by an initial pump pulse. However, in the time-dependent 2D electronic spectra, the quantum beat signal between the superposition states can hardly be seen because it is usually hidden by the strong stationary signal, which is not related to the temporal evolution of the coherently excited superposition states, but rather to that of the single quantum state. To overcome this difficulty in 2D-ES, beat-frequency-resolved analysis of 2D electronic spectra has been proposed to illustrate the vibronic and exciton states and the coherences between them as coherence amplitude maps.^{4,5} In this study, we demonstrate the visualization of the vibrational coherences in an artificial protein, through beat-frequency-resolved 2D-ES.⁶ We successfully extract the vibrational coherences behind the strong stationary signal that dominates the typical 2D spectra and the inhomogeneous broadening in the absorption spectra.

We generate sub-10 fs visible pulses using a Yb:KGW laser (1030 nm, 1.0 mJ, 10 kHz, 190 fs), followed by two pulse-compression stages. The first pulse-compression stage employs a multiplate pulse compression (MPC) technique.⁷ The output from the Yb:KGW laser is loosely focused into a gas cell filled with 1.0 bar of He, to avoid nonlinear effects around the focus. The fused-silica exit window of the gas cell and the subsequent second and third fused-silica plates act as thin plates to achieve spectral broadening in our MPC setup. The output pulses are temporally compressed by two Gires-Tournois interferometer mirrors, down to 40–50 fs. The second pulse-compression stage employs spectral broadening based on laser filamentation.⁸ The output pulses from the first MPC stage are focused by a concave mirror into a mixed gas cell (0.5 bar of Xe and 0.5 bar of He), generating white light via laser-based filamentation. The visible spectral part of the white light is selected using a short-pass filter. The transmitted visible pulses are recollimated and compressed using two chirp-mirror pairs. The white-light spectrum and temporal profile after pulse compression are depicted in Fig. 1(a) and (b), respectively. The pulse energy after pulse compression is

approximately 4.7 μ J. The long-term power fluctuation is measured to be 0.26% (standard deviation) for 25 h.

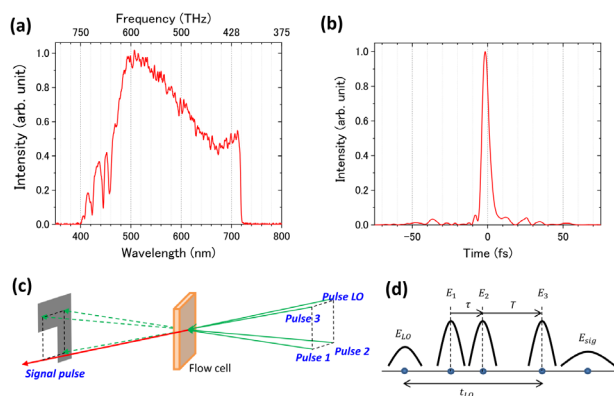


Fig. 1. (a) Spectrum and (b) temporal profile of the sub-10 fs visible pulse output after chirp-mirror-pair-based pulse compression. (c) BOXCARS geometry of four-wave mixing. (d) Time ordering of the four input pulses and signal light. E_1 and E_2 are the pump double pulses with a time interval of τ . E_3 is the probe pulse delayed from E_2 by time T . The local oscillator pulse E_{LO} is prior to the pump and probe pulses with a fixed time interval of t_{LO} between E_{LO} and E_3 .

The 2D-ES measurement system is an extension of the application of 2D infrared spectroscopy⁹ to the visible spectral region, to investigate the electronic states of the molecules. In 2D-ES measurement, three identical pulses (1, 2, and 3) and one weak local oscillator (LO) are focused on a sample in the BOXCARS geometry, as shown in Fig. 1(c). The signal light from the four-wave-mixing (FWM) process is spatially separated from pulses 1, 2, and 3, and interferes with the LO pulse to achieve heterodyne detection. The time ordering of the pulses and time interval between them are presented in Fig. 1(d). One of the pulses passes through the computer-controlled translational stage to scan the temporal delay, T , between pulses 2 and 3. The temporal delay, τ , between pulses 1 and 2 is scanned (or varied) by a pair of dispersion wedge plates in the optical path of pulse 1 to achieve sub-fs temporal resolution. The signal and LO pulses are spatially dispersed via holographic grating and focused on a line-scan CMOS camera.

The molecules are excited by double pulses 1 and 2 with the time interval τ , and probed by pulse 3 delayed by time T after pulse 2. The beating signal produced by the coherent excitation of a pair of vibronic states is measured by scanning the waiting time, T . Double pump pulses are used to obtain the excitation spectra. We measure the time-domain interferogram by scanning the time interval, τ , and obtain the spectrum from the Fourier transformation of the interferogram.

We apply our 2D-ES apparatus to the measurement of the vibrational coherence in a RasM monomer artificially synthesized by the Adachi Group at iQLS. The absorption spectrum of this molecule is shown in Fig. 2(a). Figure 2(b) shows the 2D power spectrum of the rephasing signal measured at a waiting time T of 40 fs. The FWM signal mainly appears in the upper-left region above the diagonal line, which means that the detection energy E_{det} is higher than the excitation energy E_{exc} . The dashed lines indicate the frequencies of the peak ($E_{\text{exc}} = 512$ THz) and shoulder ($E_{\text{exc}} = 550$ THz) in the RasM absorption spectrum.

Figure 2(c) shows the time profiles of the signal intensities at the diagonal points of $(E_{\text{exc}}, E_{\text{det}}) = (512 \text{ THz}, 512 \text{ THz})$ and $(550 \text{ THz}, 550 \text{ THz})$ and at the off-diagonal point of $(E_{\text{exc}}, E_{\text{det}}) = (510 \text{ THz}, 580 \text{ THz})$ in the 2D electronic spectra, as functions of the waiting time, T . At the diagonal points, fast oscillations that survive until $T = 600$ fs are clearly observed. On the other hand, at the off-diagonal point, no significant fast oscillation is observed. Figure 2(d) shows the Fourier-transformed spectra of the time profiles. The beat frequencies can be identified as $E_{\text{beat}} = 35.2$ THz for the time profile measured at $(E_{\text{exc}}, E_{\text{det}}) = (512 \text{ THz}, 512 \text{ THz})$, $E_{\text{beat}} = 46.0$ THz at $(550 \text{ THz}, 550 \text{ THz})$, and $E_{\text{beat}} = 16.5$ THz at $(510 \text{ THz}, 580 \text{ THz})$. These beat signals provide clear evidence of the vibrational coherence.

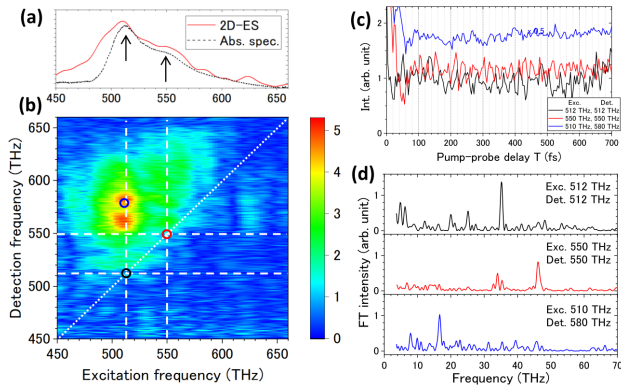


Fig. 2. (a) Absorption spectrum of the RasM monomer. (b) 2D power spectrum of the rephasing signal measured at the waiting time T of 40 fs. The white dashed lines indicate the frequencies of the peak (512 THz) and shoulder (550 THz) in the absorption spectrum of RasM. (c) Pump-probe time profiles observed at the three points of the 2D spectra shown in (a). (d) Beat-frequency spectra calculated by the Fourier transformation of the time profile shown in (c).

To further investigate the vibrational coherence, the FFT spectra of the pump-probe profiles are calculated at all excitation and detection frequencies on the 2D spectra at intervals of 4 THz. The intensity at a specific beat frequency is mapped as a function of the excitation and detection frequencies. Figure 3 shows the 2D intensity maps at $E_{\text{beat}} = 16.5$ and 35.2 THz, found in Fig. 2(d). In the beat-frequency-resolved 2D spectra, we find many peaks hidden by a strong stationary signal ($E_{\text{beat}} \approx 0$ THz).

The progression of the peaks along the excitation frequency axis can be observed clearly in the 2D map at $E_{\text{beat}} = 16.5$ THz. All peaks belonging to the progression are broad along the detection frequency axis. The progression of the peaks along the

excitation frequency axis, observed in the beat-frequency-resolved 2D-ES is not visible in the absorption spectrum, owing to the occurrence of inhomogeneous broadening. Progression A starts at $E_{\text{exc}} = 510$ THz with an interval of 35 THz on the excitation frequency axis. The frequency of 510 THz is close to the peak frequency in the absorption spectrum, indicating that the pump pulse excites the molecules to the bottom of the first electronically excited state.

At $E_{\text{beat}} = 35.2$ THz, peak B1 is found at the diagonal position of the 2D map. Both the excitation and detection frequencies at this diagonal position are approximately 512 THz, which is the peak frequency of the absorption spectrum shown in Fig. 2(a). The other diagonal peak, B2, is also found at approximately $E_{\text{exc}} = E_{\text{det}} \approx 550$ THz, which is close to the shoulder in the absorption spectrum. Weak cross-peaks B3 and B4 are observed at off-diagonal positions $(E_{\text{exc}}, E_{\text{det}}) = (512 \text{ THz}, 550 \text{ THz})$ and $(550 \text{ THz}, 512 \text{ THz})$, respectively.

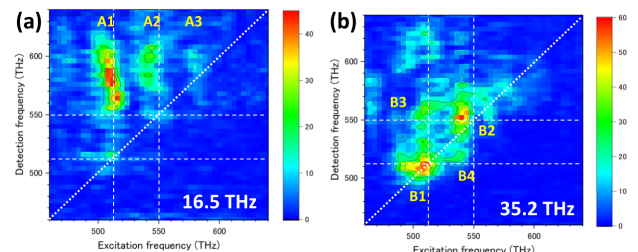


Fig. 3. Beat-frequency-resolved 2D spectra of RasM. The 2D spectra (a) and (b) are extracted from the total 2D spectra at the beat frequencies of $E_{\text{beat}} = 16.5$ and 35.2 ± 1 THz, respectively.

We will extend this method to observe the quantum coherence between the exciton states in a RasM dimer or heterodimer of RasM and its derivative. Because we have already assigned vibrational coherence to the RasM monomer, we can easily distinguish it from the coherence between the exciton states. This method can be applied to natural and artificial photosynthesis proteins to investigate the relationship between the coherence phenomena and high-efficiency unidirectional energy transfer during photosynthesis.

Acknowledgements

The authors thank Y. Yonetani and A. Tanaka at QST for the valuable discussions on quantum coherence within biomolecules. We also thank A. Ishizaki at the Institute for Molecular Science for the valuable comments on 2D-ES.

References

1. J. Cao et al., *Sci. Adv.* **6** eaaz4888. (2020).
2. G. D. Scholes et al., *Nat. Chem.* **3** 763-774. (2011).
3. A. Ishizaki, G. R. Fleming, *Annu. Rev. Condens. Matter Phys.* **3** 333-361. (2012).
4. F. D. Fuller et al., *Nat. Chem.* **6** 706-711. (2014).
5. E. Romero et al., *Nat. Phys.* **10** 676-682. (2014).
6. M. Tsubouchi et al., arXiv:2211.02220. (2022).
7. C.-H. Lu et al., *Optica* **1** 400-406. (2014).
8. C. P. Hauri et al., *Appl. Phys. B* **79** 673-677. (2004).
9. D. B. Strasfeld, S.-H. Shim, M. T. Zanni, in *Advances in Chemical Physics*, pp. 1-28 (2009).

Numerical experiments to elucidate propagation effects in high harmonic generation from solids

YAMADA Shunsuke

Ultrafast Dynamics Group, Department of Advanced Photon Research



Recently, high-order harmonic generation (HHG) in solids has been the subject of extensive experimental and theoretical research. HHG in waves reflected or transmitted from a solid thin film is thought to be significantly modulated by the nonlinear light-propagation effect within the thin film [1]. However, it is impossible to experimentally observe this modulation inside thin films. First-principles calculations using the time-dependent density functional theory (TDDFT) can provide realistic and reliable descriptions for the microscopic mechanisms underlying HHG in solids [2]. In this study [3], numerical experiments were conducted to investigate the nonlinear light-propagation effect in HHG from laser-irradiated silicon (Si) thin films by employing a computational method that combines Maxwell's equations for light propagation and TDDFT for electron dynamics.

We consider the irradiation of a free-standing Si thin film of thickness d in vacuum by an ultrashort light pulse of a linearly polarized plane wave with normal incidence [Fig. 1(a)]. The light propagation is described in the macroscopic scale by solving the following one-dimensional wave equation:

$$\left(\frac{1}{c^2} \frac{\partial^2}{\partial t^2} - \frac{\partial^2}{\partial z^2}\right) \mathbf{A}_Z(t) = \frac{4\pi}{c} \mathbf{J}_Z(t),$$

where Z is the macroscopic coordinate. $\mathbf{A}_Z(t)$ and $\mathbf{J}_Z(t)$ are the vector potential and current density, respectively, of the film. This wave equation is solved using a one-dimensional grid for the Z variable. At each grid point of Z inside the film, we consider an infinite crystalline system of the film material. The electronic motion in the unit cell of each crystalline system is described by the Bloch orbitals $u_{nk,z}(\mathbf{r}, t)$, which satisfy the time-dependent Kohn–Sham equation:

$$i\hbar \frac{\partial}{\partial t} u_{nk,z}(\mathbf{r}, t) = h_k[\mathbf{A}_Z](t) u_{nk,z}(\mathbf{r}, t),$$

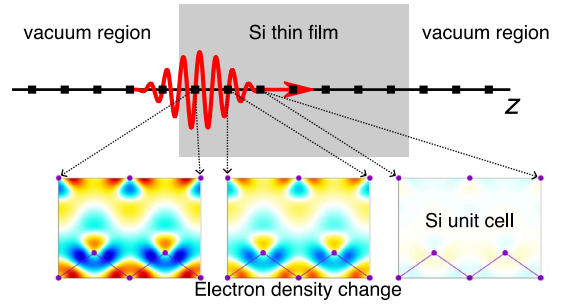
where $h_k[\mathbf{A}_Z](t) = (1/2m)(-i\hbar\nabla + \hbar\mathbf{k} + (e/c)\mathbf{A}_Z(t))^2 + V_{\text{KS}}(\mathbf{r}, t)$ is the effective single-electron Hamiltonian and $V_{\text{KS}}(\mathbf{r}, t)$ is the Kohn–Sham potential. The electric current density averaged over the unit-cell volume Ω is defined as follows:

$$\mathbf{J}_Z(t) = -e \int_{\Omega} \frac{d^3r}{N_k \Omega} \sum_{n,k} u_{nk,z}^*(\mathbf{r}, t) \left[\frac{r}{i}, h_k[\mathbf{A}_Z](t) \right] u_{nk,z}(\mathbf{r}, t).$$

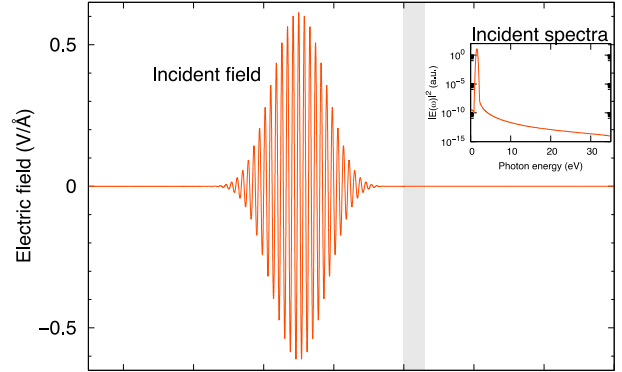
By simultaneously solving the above equations, the ultrafast and nonlinear dynamics of the light pulse and electrons inside the film can be simulated. We call this method [4] “multiscale Maxwell-TDDFT.”

Figures 1(b) and (c) show snapshots of the electric field of the light pulse propagating through a thin Si film with a thickness $d = 3000$ nm. Figure 1(b) presents the electric field of the initial pulse ($t = 0$ fs), which is located in front of the film, wherein the film is presented as a thin gray area. We used an incident pulse with a wavelength of 800 nm, full-width-at-half-maximum (FWHM) of 21.4 fs, and peak intensity of 5×10^{12} W/cm². Figure 1(c) shows a snapshot of the electric field at $t = 150$ fs. Here, we display the results corresponding to initial pulses of two different maximum intensities: a strong pulse ($I = 5 \times 10^{12}$ W/cm², red solid line), and a weak pulse ($I = 10^9$ W/cm², blue dotted line). Linear

(a) Multiscale Maxwell-TDDFT method



(b) $t = 0$ fs



(c) $t = 150$ fs

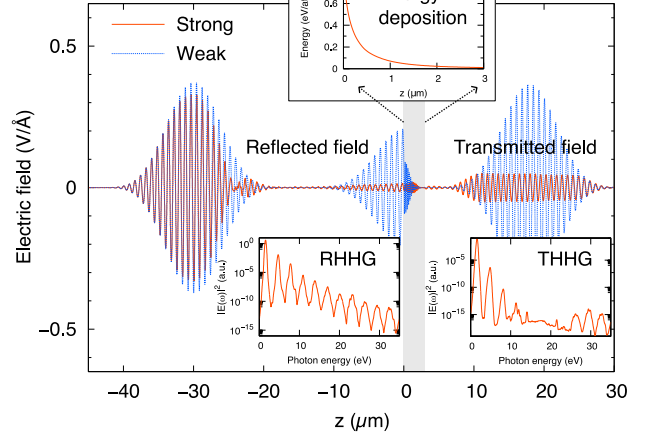


Fig. 1 (a) Overview of the multiscale Maxwell-TDDFT method for light propagation through a thin Si film. The electron density changes driven by the light pulse are illustrated for the first three grid points. (b) Electric field at $t = 0$. The incident pulse is generated in front of the thin Si film, which is exhibited as a gray area. (c) Electric field at $t = 150$ fs is shown for the case of two incident pulses: a strong pulse ($I = 5 \times 10^{12}$ W/cm², red solid line) and a weak pulse ($I = 10^9$ W/cm², blue dotted line) scaled up by a factor of $\sqrt{5000}$. The Fourier spectra of the respective pulses and energy deposition [(c)] are shown in the insets.

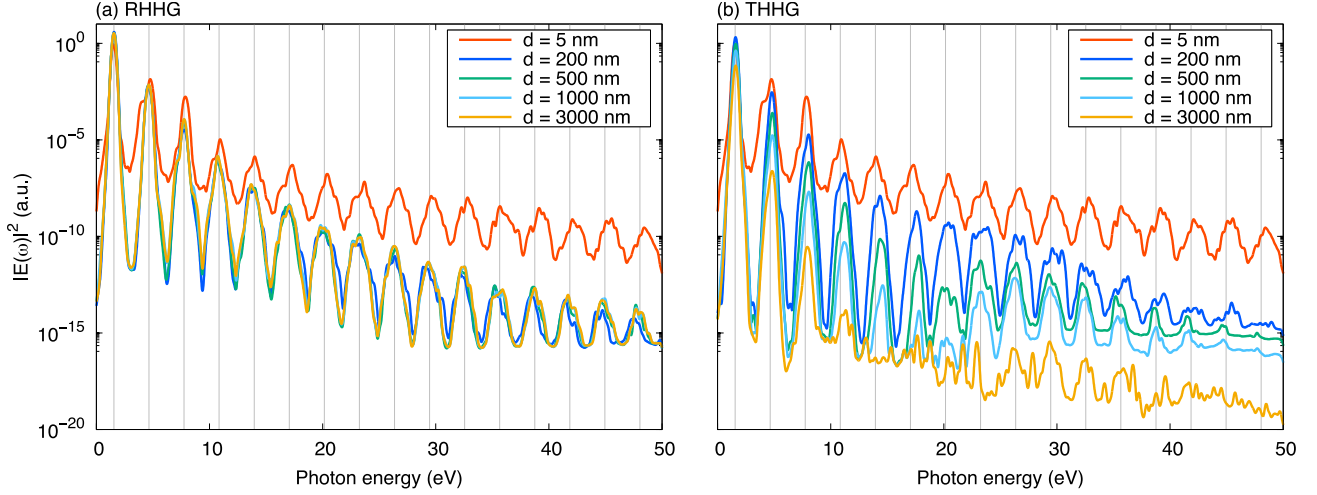


Fig. 2 HHG spectra for the waves (a) reflected and (b) transmitted from the thin Si film with a thickness of $d = 5, 200, 500, 1000,$ and 3000 nm.

propagation is expected for the weak pulses. In the figure, the weak pulse is multiplied by a factor of $\sqrt{5000}$ so that the differences between the two lines manifest nonlinear effects in the stronger pulse. The reflected and transmitted pulses are shown in Figure 1(c). They are separated from the film (left for the reflected pulses and right for the transmitted pulses). There also appears to be a component around the film, which is caused by reflection at the back surface of the film. By Fourier transforming the reflected and transmitted fields, we obtain the HHG spectra for the respective fields, as depicted in the insets.

Figure 2 shows the calculated HHG spectra in the waves reflected and transmitted from thin Si films with thicknesses of $d = 5, 200, 500, 1000,$ and 3000 nm. We used an incident pulse with a wavelength of 800 nm, FWHM of 21.4 fs, and peak intensity of 4×10^{12} W/cm². The spectra for reflection and transmission, for a film thickness of 5 nm, are equivalent and are the strongest among the signals of films of different thicknesses. These features have already been reported in our previous analysis [5], and can be understood in terms of the two-dimensional approximation for electromagnetism, which is valid for very thin films. While the reflection HHG [Fig. 2(a)] is almost saturated at $d = 200$ nm, the transmission HHG [Fig. 2(b)] continuously decreases as the thickness increases. In particular, the latter for $d = 1000$ nm shows a dip around the photon energy of 20 eV. Through frequency- and depth-resolved analyses of light pulses, we find that the transmission HHG has two origins: the HHG generated near the front edge and propagating to the back surface, and that generated near the back edge and emitted directly [3]. The dominant mechanism of the transmission of HHG is found to depend on the thickness of the thin film and the frequency of the HHG. For the film with $d = 1000$ nm, a transmission HHG with a frequency below 20 eV is generated near the back edge, whereas that with a frequency above 20 eV is generated near the front edge and propagates from there to the back surface. The transmission

HHGs below and above 20 eV have different origins, and the dip at 20 eV is due to the combination of the two mechanisms.

In this study, we found that the nonlinear propagation dynamics of light pulses cause significant effects in HHG from nano to micrometer-thick Si films. This study demonstrates that the multiscale Maxwell-TDDFT scheme provides a reliable description of such phenomena.

Acknowledgments

The authors thank T. Otobe, D. Freeman, A. Kheifets, and K. Yabana. This research was supported by JST-CREST under grant number JP-MJCR16N5, MEXT Quantum Leap Flagship Program (MEXT Q-LEAP) Grant Number JPMXS0118068681 and JPMXS0118067246, and JSPS KAKENHI Grant Number 20H2649. Calculations were carried out on the Fugaku supercomputer with the support of the HPCI System Research Project (Project ID: hp220120), SGI8600, at the Japan Atomic Energy Agency (JAEA) and Wisteria at the University of Tokyo with the support of the Multidisciplinary Cooperative Research Program in CCS, University of Tsukuba.

References

1. P. Xia, C. Kim, F. Lu, T. Kanai, H. Akiyama, J. Itatani, and N. Ishii, *Opt. Express* **26**, 29393 (2018).
2. C. Yu, S. Jiang, and R. Lu, *Adv. Phys. X* **4**, 1562982 (2019).
3. Yamada, T. Otobe, D. Freeman, A. Kheifets, and K. Yabana, *Phys. Rev. B* **107**, 035132 (2023).
4. K. Yabana, T. Sugiyama, Y. Shinohara, T. Otobe, and G. F. Bertsch, *Phys. Rev. B* **85**, 045134 (2012).
5. S. Yamada and K. Yabana, *Phys. Rev. B* **103**, 155426 (2021).

Modeling the wavelength of unresolved transition arrays in the extreme ultraviolet region for Sn to Hf ions by combining theoretical and experimental spectral data



SASAKI Akira

X-ray Laser Group, Department of Advanced Photon Research

We studied the collisional radiative (CR) model of Sn and heavier elements with atomic numbers $Z = 50-71$. We investigated the atomic emission of multiple-charged ions in the extreme ultraviolet (EUV) wavelength region [1,2]. Sn ions exhibit strong emission in the $\lambda = 13.5$ nm wavelength region, which is now being applied to lithography [3]. This technology will be extended to shorter wavelengths near $\lambda = 6$ nm using rare-earth elements [4].

More than 300 W of EUV power was obtained using a laser-pumped plasma (LPP) EUV source [5]. The Sn microdroplet target was irradiated by a CO₂ laser pulse to produce plasma with a temperature and electron density of 30 eV and 10^{20} /cm³, respectively. EUV emission from Sn arises from 4d–4f and 4p–4d transitions from ~ 10 times ionized states [6].

These ions have a ground-state configuration of $4d^n$, where n is the number of bound electrons. Figure 1 shows an example of the energy-level diagram of Y-like Sn (Sn^{11+}). With a ground-state configuration of $4d^{3+}$, this ion has many multiply excited states, which have a large population in the plasma. The EUV emission is generated from the 4d–4f and 4p–4d transitions, not only from singly excited states but also from multiply excited states. Moreover, each transition consists of fine structure lines, which are distributed over a wavelength region of ~ 1 nm, resulting in the emission spectrum appearing as a broad peak called an unresolved transition array (UTA).

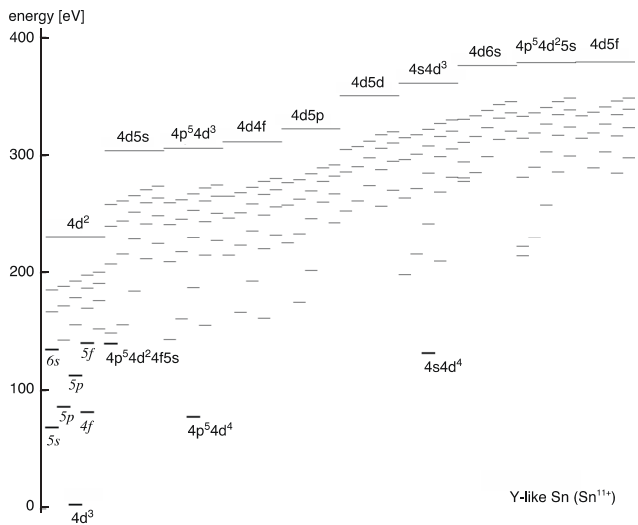


Figure 1. Energy-level diagram of Y-like Sn (Sn^{11+}).

Although the atomic structure of multiply charged Sn ions is complex, the observed EUV spectrum is sometimes simple, with few peaks that correspond to 4d–4f, 4p–4d, 4d–5p, and 5d–5f transitions. In the presence of the effect of configuration interaction, 4d–4f and 4p–4d transitions appear as a single UTA at $\lambda = 13.5$ nm.

We show that the wavelength of the combined 4d–4f/4p–4d UTA can be explained based on the screening theory [9]. As shown in Fig. 2, the model assumes a hydrogen-like structure of the ion. The electric field for an electron in the nl shell feels is determined from the effective charge, Z_{nl}^* , which is defined by the charge of the nucleus, considering the screening effect of electrons in closed shells up to 4p, $Z_{core,nl}$, with the screening effect from the electrons in the 4d shell, as

$$Z_{nl}^* = Z_{core,nl} - \sigma_{4d,nl} N_{4d}, \quad (1)$$

where $\sigma_{4d,nl}$ is the screening coefficient from the electrons in the 4d shell to an electron in nl shell and N_{4d} is the occupation number of the electrons in the 4d shell. Subsequently, the energy of the 4d–nl transition is determined from the energy of the upper and lower states using Balmer’s formula for hydrogen-like ions, as follows:

$$\Delta E_{4d-nl} = R_y \left[\left(\frac{Z_{4d}^*}{4} \right)^2 - \left(\frac{Z_{nl}^*}{n} \right)^2 \right]. \quad (2)$$

We also investigate the wavelengths of the combined 4d–4f/4p–4d, 4d–5p, and 4d–5f UTA of Pd-like to Rb-like Sn to Hf based on the atomic data calculated using HULLAC [7]. First, we calculate the atomic energy levels and transition probabilities of the UTAs. Second, we fit the effective charge, Z_{nl}^* , to obtain the core charge, $Z_{core,nl}$, and screening coefficient, $\sigma_{4d,nl}$, as in Eq. (1). Finally, we calculate the transition energy and thus, the

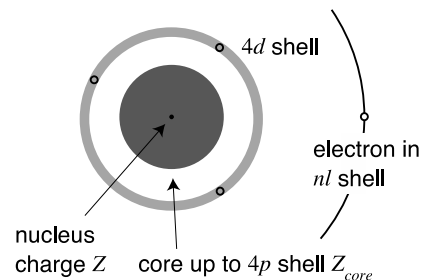


Figure 2. Screening model of the atomic structure of multiple charged Sn ions with open 4d shell.

wavelength of the UTAs using Eq. (2). The model shows that the wavelengths of the 4d–5p and 4d–5f UTAs decrease as the charge increases, whereas the wavelength of the combined 4d–4f/4p–4d UTA is almost constant in the $\lambda = 13.5$ nm wavelength region.

We validate this model through a detailed comparison of the calculated and experimental results. Figure 3 shows the calculated and observed EUV spectra of Gd ions. It is shown that the calculated wavelength, based on the screening theory, reproduces the observed trend. Nevertheless, the experimental wavelengths are longer by ≈ 0.2 nm, owing to the strong configuration interaction. It is difficult to consider the effect of the configuration interactions. However, even for the calculated structure of the UTA, the distribution of fine structure lines is different from that in the experiment, and the average width of the UTA is similar. To model the EUV spectrum, the present results suggest that the model can reproduce the experimental spectrum by applying minor corrections to the wavelength.

In summary, we studied the atomic and radiative properties of Sn in rare-earth plasmas to develop a CR model that reproduced the emission spectrum.

We developed the CR model based on computational atomic data. The calculations showed that the EUV emission arose from the 4d–4f/4p–4d, 4d–5p, and 5d–5f UTAs from multiply charged ions of Sn to rare-earth elements. The calculations were validated through a detailed comparison with the experimental spectra.

The model was shown to be useful for the realization of the EUV source at $\lambda = 13.5$ nm using Sn plasmas. Improvement of the accuracy of the model is still necessary for further improvement of Sn sources as well as the development of shorter-wavelength sources.

The wavelength of the UTA can be explained based on a simple screening theory, which makes a simple representation of the atomic model possible. In contrast to the present complex atomic model, which sometimes consists of 10^4 energy levels, an atomic model with fewer levels with averaged collisional and radiative rates is of interest because such a modeling method would enable the investigation of radiative transfer in Sn plasmas, which has been out of reach with the present method because of computational difficulties.

Acknowledgments

AS acknowledges the useful discussions with Izumi Murakami and Hiroyuki Sakaue at the National Institute for Fusion Science, Keiske Fujii at Kyoto University, Hayato Ohashi at Toyama University, Takeshi Nishikawa at Okayama University, and Nobuyuki Nakamura at the University of Electro-Communications.

This work was supported by the JSPS (Grant No. 21H04460) and the Matsuo Science Foundation.

References

1. A. Sasaki et al. AIP Advances, 12, 025309 (2022).
2. A. Sasaki et al. J. Appl. Phys. 107, 113303 (2010).
3. “EUV Lithography”, edited by V. Bakshi (SPIE Press, 2018).
4. T. Higashiguchi et al. Opt. Express 21, 31837 (2013).
5. H. Mizoguchi et al. Proc. SPIE 11609, 1160919 (2021).
6. K. Nishihara et al. Phys. Plasmas 15, 056708 (2008).
7. A. Bar-Shalom et al. J. Quant. Spectrosc. Radiat. Transfer, 71, 169 (2001).
8. H. Ohashi et al. Phys. Scr. T156, 014013 (2013).
9. R.V. Jensen et al. Nucl. Fusion, 17, 1187 (1977).

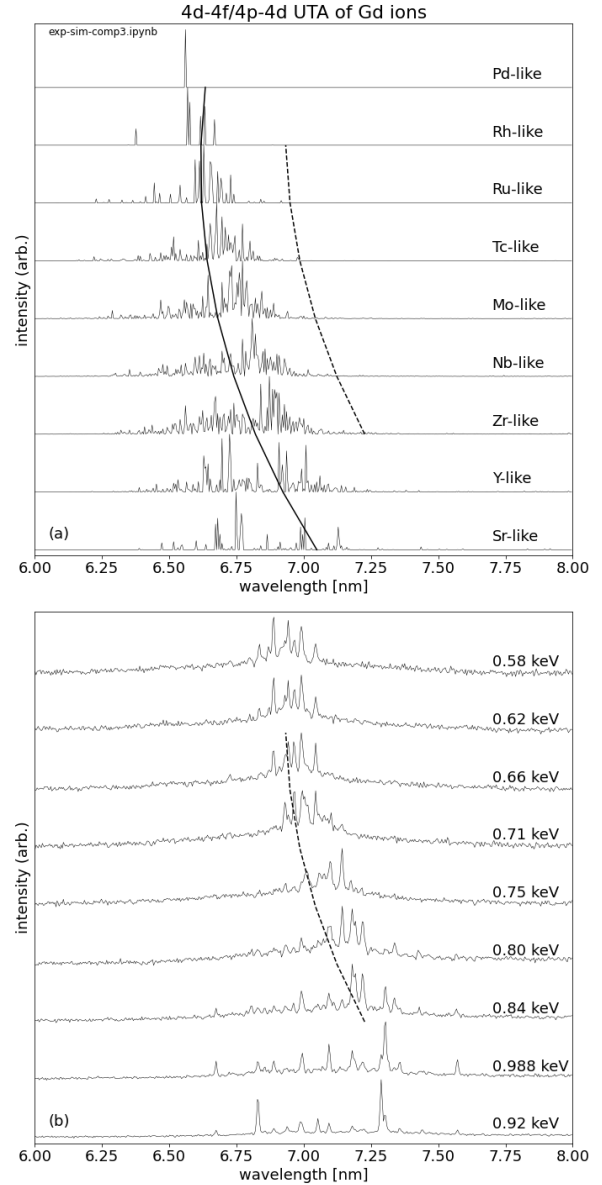


Figure 3. (a) Calculated EUV spectrum (thin lines) of combined 4d–4f/4p–4d transition of Pd-like to Sr-like Gd ions using the HULLAC code. (b) EUV spectrum observed using EBIT [8] (thin lines), measured at energies of electron beam tuned below the ionization limit of Pd-like to Sr-like ion. Thick solid line in (a) shows the transition wavelength calculated using the screening theory. Thick dotted line is obtained by applying the screening theory to the observed spectrum.

Enhancement of high-order harmonic generation in a double-jet arrangement and its application to EUV resist materials



NAMBA Shinichi¹ and Thanh-Hung DINH²

¹ Graduate School of Advanced Science and Engineering, Hiroshima University

² X-ray Laser Group, Department of Advanced Photon Research

High-order harmonic generation (HHG) is an extremely nonlinear optical process that occurs when atoms are placed in a strong driving laser field, resulting in the emission of photons at integer multiples of the driving-field frequency. An exciting advancement of HHGs is their ability to generate ultrafast (0.1–10 fs) coherent X-rays (from the extreme ultraviolet (EUV) to the soft X-ray region) from a tabletop scale apparatus. HHG has paved the way for the exploration of the electron dynamics in atoms and molecules, in the attosecond time scale [1, 2]. Since the first experiment of HHG, the underlying physics has been intensively studied from several different viewpoints: classical, semiclassical, and quantum mechanical. The interest then shifted to: (1) generation of short-wavelength harmonics using a long-wavelength drive laser and (2) generation of a single attosecond pulse, which provides readily understandable information on the X-ray and atom interaction. So far, there has been a keen demand to increase the photon flux of such high harmonics for practical applications such as multiphoton ionization of atoms and molecules and single-shot coherent diffractive imaging. In addition, the development of compact and intense HHG sources has received greater focus, along with the investigation of their potential applications, especially in the field of current EUV lithography (EUVL) and beyond.

In this study, we examine the optimal conditions for double-jet arrangements to obtain an intense, low-divergence HHG beam at photon energies of approximately 100 eV. We focus on the parametric responses of the 59th harmonic line of the 800 nm drive laser, because it lies near 13.5 nm (91.9 eV), which is usable for coherent lithography and diagnostic applications, and for seeding X-ray lasers and free electron lasers (FELs). By using such a high harmonic beam, we can attempt to evaluate the response of photoresist materials exposed to intense ultrashort EUV pulses, as a touchstone for the next-generation EUV-FEL lithography.

Experiments using a Ti:sapphire laser system were conducted at the Kansai Photon Science Institute. Pulses with 800 nm central wavelength, 80 fs duration, 30 mJ energy, 10 Hz repetition rate, and 20 mm beam diameter were focused by a lens with a focal length of 4000 mm to a double-jet arrangement. In the focus, the beam waist was $\approx 200 \mu\text{m}$ and the laser intensity was up to 1 PW/cm^2 . The laser beam passed through two gas jets, as shown in Fig. 1. The first He gas jet (Jet1) produced the weak seed HHG pulse as an oscillator and subsequently, the seed pulse was amplified in the second He jet (Jet2). He gas was supplied through fast solenoid valves to minimize the gas flow and background pressure in the vacuum chamber to suppress the EUV absorption of the ambient gas. The gas jet tubes were fitted to the gas valves and were made of Mo to avoid laser damage. Holes of 1 mm diameter (for gas supply) were drilled into the tube with 3 mm diameter, as can be seen in the inset of Fig. 1. The 40 mm

long Rayleigh length of the focused beam was much longer than the 3 mm tube length of the gas jets and 25 mm maximal distance between the jets used in the measurements. The gas jet valves were mounted on motorized translation stages to precisely set the gas jet positions along the focused laser beam and set the distance between them. The HHG beam was monitored by an X-ray charge-coupled device (CCD) camera (back illuminated, $13 \mu\text{m}$ pixel, 1 sq. in. detection area) for beam spatial profile measurements. Spectral measurements were obtained using an EUV spectrometer of the grazing-incidence type, with a 1200 grooves/mm flatfield grating. A spherical mirror was installed in front of the entrance slit to measure the HHG beam divergences. The fundamental laser light was blocked by a thin Zr filter.

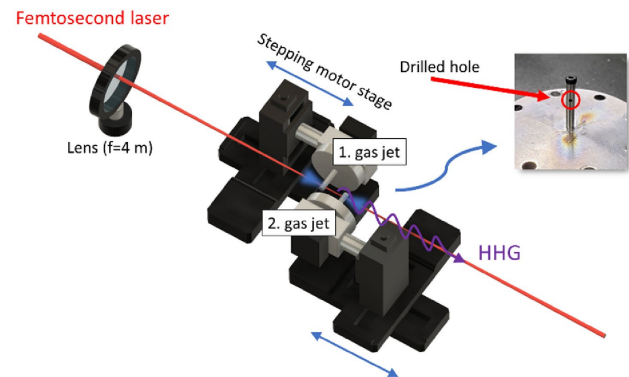


Fig. 1. Experimental setup shows the two-jet sequence used for the experiments. Their position and distance were adjustable by the motorized stages. The inset shows a photograph of the Mo tube used as a gas jet nozzle [3].

To optimize the harmonic source and understand the underlying processes, the distance between the two gas jets was scanned to investigate the correlations (delay) between the seed EUV pulse produced in Jet1 and the gain medium of Jet2. We observed a nonlinear response of the 59th harmonic line, as shown in Fig. 2. The intensity of the 59th harmonic line was in the saturation regime, at approximately 30 mJ, as shown in Fig. 2(a), which made the generation of the harmonic line robust and insensitive to the energy fluctuation of the pump laser. Additionally, the wavelength of the harmonic line remained almost intact under saturation, and only a small blueshift of the line could be observed at pulse energies beyond saturation because of the strong ionization of the gas. Comparing Figs. 2(b) and 2(c), the influence of the parametric interaction could be observed even in the saturation regime of 30 mJ. Indeed, the intensities of the harmonic lines were much stronger in Fig. 2(c) than the intensities that can be expected from the constructive superposition of the weak seed (Jet1) and the amplifier (Jet2)

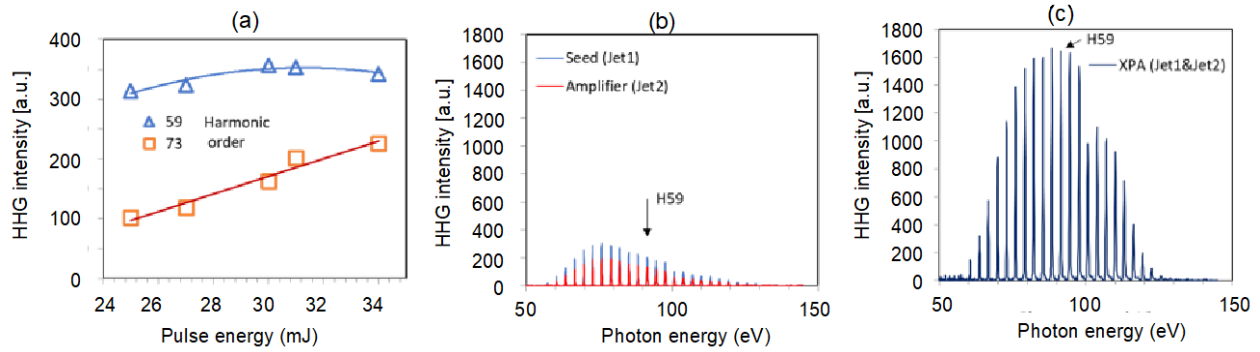


Fig. 2. Measurements of HHG for 0.2 bar He gas in Jet1, 0.25 bar He gas in Jet2, and jet distance of 10 mm. (a) The harmonic line of H59 is saturated under the experimental conditions of appropriate energy of the pump laser pulse, while near the cutoff, the intensity of the harmonic line H73 increases. (b) The two gas jets alone generate weak harmonic spectra (laser energy: 30 mJ). (d) When both jets operate simultaneously, the intensities of the generated harmonic lines are much stronger than the coherent constructive superposition of lines from the two jets operating separately, showing the presence of the parametric amplification process [3].

spectral lines generated independently in the two He gas jets, which are plotted in Fig. 2(b). The effect was especially strong near 110 eV. Here, the intensities of the harmonic lines from the independent jets were below 100 (CCD counts), whereas they could be over 1000 counts when the two jets operated together. Further properties of the HHG source, such as the beam profile, beam divergence, and small-signal gain, and discussions on the underlying physics can be found in Ref. [3].

order harmonics around 13.5 nm after they pass through two Zr filters and are reflected by a Mo/Si multilayer flat mirror. The exposure time was varied from 30 to 300 seconds to regulate the dose absorption. Figure 3(c) is an atomic force microscopy (AFM) image of a single-line pattern after development of an in-house-developed metal resist. The line was very well shaped at a width of less than 2 μm , benefiting from the high quality of the HHG beam.

In summary, we reported the characterization of parametric amplification in HHG around 100 eV using He gas in a double gas-jet arrangement. By employing a single He gas jet, a conventional weak, large-divergence high-harmonic beam was generated. With the double-jet scheme, at the optimal jet distance, the 59th harmonic intensity with small beam divergence drastically increased owing to the parametric amplification. By using the developed high-harmonic beam, we could evaluate the sensitivity of photoresist materials exposed to ultrashort EUV pulses as a touchstone for next-generation EUV-FEL lithography [6]. In a future study, we plan to optimize both the length and pressure of each gas jet to further boost the HHG output. Furthermore, by slightly tuning the fundamental wavelength of a Ti:sapphire laser, the 59th order harmonic energy can be shifted to a suitable seed pulse for Ni-like silver plasma X-ray lasers (89.2 eV, 13.9 nm) to provide fully spatially and temporally coherent bright beams.

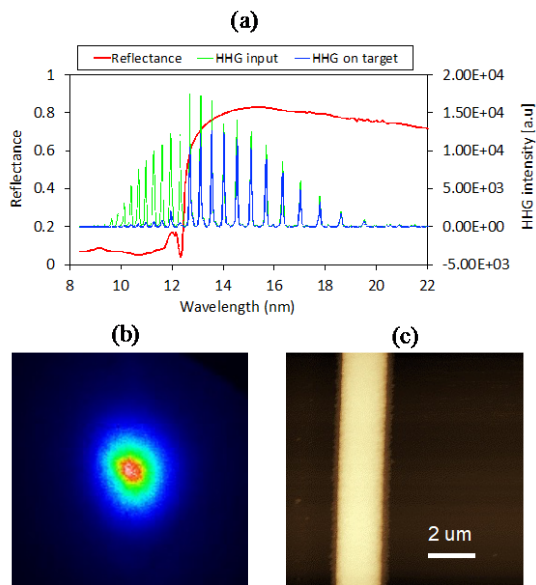


Fig. 3. Features of the HHG beam used for the evaluation of the resist. (a) Spectrum of the HHG beam and (b) typical beam profile of the high harmonics around 13.5 nm. (c) An AFM image of a well-shaped single line-pattern after development of an in-house-developed metal resist [4, 5].

To evaluate the sensitivity of the resist materials, we employed a Mo/Si multilayer spherical mirror with a curvature of 500 mm and set the grazing incidence angle to $\sim 10^\circ$ to collect a broad EUV spectrum from the HHG source and then focus on the target surface. A Zr filter with a thickness of 200 nm was used to block the fundamental laser light. Reflectance of the mirrors and transmittance of the filters were measured in advance using synchrotron radiation at the 11D beamline of the High Energy Accelerator Research Organization (KEK)-photon factory (PF). Typical spectra of the focused HHG beam, which are displayed as the blue lines in Fig. 3(a), were calculated from the measured results of the input HHG spectra (green line) and mirror reflectance (red line). Figure 3(b) is the 2D image of the high-

Acknowledgments

The authors thank the co-researchers listed below: J. Seres, E. Seres of Vienna University of Technology, C. Serrat of Polytechnic University of Catalonia, N. Hasegawa, M. Ishino, M. Nishikino, and H. Yamamoto of the QST. The authors also acknowledge the support from the Japan Society for the Promotion of Science (JP19K15402, JP20H00141, JP21H03750) and the JKA Foundation (KEIRIN RACE).

References

1. F. Krausz and M. Ivanov, *Mod. Phys.*, **81**, 163–234, (2009).
2. K. Midorikawa, *Jpn. J. Appl. Phys.*, **50**, 090001 (2011) and references therein.
3. J. Seres *et al.*, *J. Opt. Soc. Am. B*, **39**, 1263 (2022) and references therein.
4. S. Namba *et al.*, *The 6th Asia-Pacific Conference on Plasma Physics*, 9-14 Oct., 2022.
5. T.-H. Dinh *et al.*, *The 43rd Annual Meeting of The Laser Society of Japan*, 18-20 Jan., 2023.
6. H. Yamamoto *et al.*, *The 39th International Conference of Photopolymer Science and Technology*, 27-30 Jun., 2022

Application of mid-infrared microscopic imaging techniques to histopathological analysis

AOYAMA Makoto¹⁾, MORIOKA Takamitsu^{2,3)}, YAMAKAWA Koichi¹⁾

¹⁾ Medical Laser Applications Group, Department of Advanced Photon Research

²⁾ Department of Radiation Effects Research, NIRS

³⁾ Institute for Quantum Life Science



The QST has developed various “quantum beams” for material sciences, some of which are beginning to be applied in life sciences. Spectroscopy has contributed greatly to scientific understanding in the physical sciences, as it can provide information on the structures of the elements and molecules that comprise every subject in both the physical and biological sciences. Infrared (IR) spectroscopy has been widely applied to detect the vibrational characteristics of chemical functional groups in a diverse range of materials [1-3]. Vibrational microscopic imaging techniques using mid-infrared (MIR) spectroscopy allow the detection and characterization of the molecular components of biological specimens. As many molecular functional groups have resonant wavelengths in this spectral range (Fig. 1), the MIR absorption spectra provide image

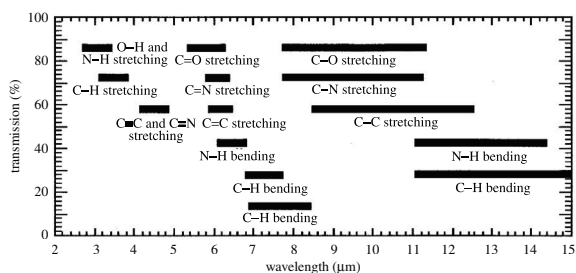


Fig.1. Correlation of various group molecular vibrations.
R. W. Waynant et al., Philos T Roy Soc A 359, 635,2001

contrasts that identify the molecular components. The advantage of this technique is the production of unique images that show the spatial distributions of proteins, lipids, carbohydrates, cholesterols, nucleic acids, and phospholipids. In addition, MIR imaging is advantageous because of its efficiency and adaptability in noninvasive investigations of the chemical compositions of cells and tissues using a procedure that is reagentless and does not require staining. Therefore, MIR imaging is a useful tool in medical research.

Pathology is the study and diagnosis of disease through the examination of organs, tissue, and cells. Disease diagnosis by pathology generally involves gross and microscopic visual examination of tissue and cells, with specialized stains employed to visualize specific proteins. Certain visualization techniques such as special staining, immunohistochemistry, and electron microscopy, have expanded the means by which pathologists can diagnose various diseases. However, it is difficult to visually detect biochemical changes using these techniques, which require complicated processes and considerable amounts of time. Therefore, a simple analytical method is desirable. MIR spectroscopy has the potential to be applied as a visualization tool to aid pathologists in assessing tissue specimens.

The purpose of this study is to investigate the discrimination between normal tissue and malignant tumors or noncancerous

lesions in various organs using an MIR laser. We constructed the MIR microscopic system for the analysis of tissue specimens. The schematic of the system is shown in Fig. 2. The beam from the MIR laser was focused onto a spot on the specimen. The transmitted and reflected beam intensities were measured using a detector. To obtain an MIR microscopic mapping image, the focused spot scans across the specimens in one direction while scanning one pixel in the orthogonal direction using an XY stage. The results of two different tissue specimens measured using the MIR microscopic system are described here. The first measurements produced a mapping image and the spectra of a specimen with a simple structure consisting of normal tissue and a malignant tumor. Furthermore, the measured results of a specimen with a noncancerous microlesion consisting of abundant stroma and dysplastic nuclei were presented.

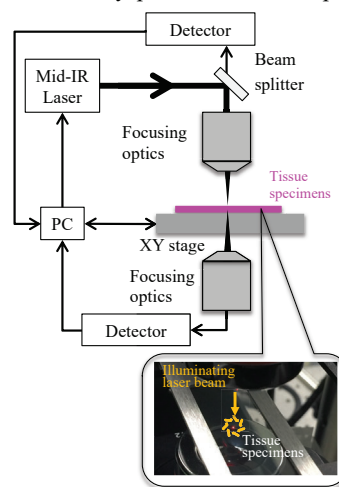


Fig.2. Mid-IR microscopic imaging system.

Tissue specimens of a simple structure consisting of a malignant lung tumor and normal lung tissue of a mouse were analyzed and their absorbances were compared with the absorbance obtained from an unstained tissue specimen (Fig. 3). Fig. 3a shows an optical micrograph of the H&E (Hematoxylin Eosin)-stained tissue specimen containing a malignant lung tumor and normal lung tissue. Fig. 3b illustrates the MIR spectra of the normal lung tissue and malignant lung tumor from two different sites in the normal and tumor areas and shows that the spectral patterns in the tumor (red lines) differ from those in the normal tissue (green lines). The majority of changes in absorbance were observed in two different regions (blue double-headed arrows, Fig. 3b). Microscopic mapping of the malignant lung tumor was performed to investigate the absorbance of the tumor cells. The tumor area for mapping was determined by examining the MIR microscopic field and comparing it with the corresponding histopathological view (Fig. 3a). Fig. 3c displays

the MIR absorbance map of segments of three main components of the malignant lung tumor and normal lung changes: malignant lung tumor (yellow and orange) and normal lung tissue (green), and the slide glass area without tissue sections (red).

The results for the specimens with noncancerous microlesions are shown in Fig. 4. Fig. 4a shows an optical micrograph of the

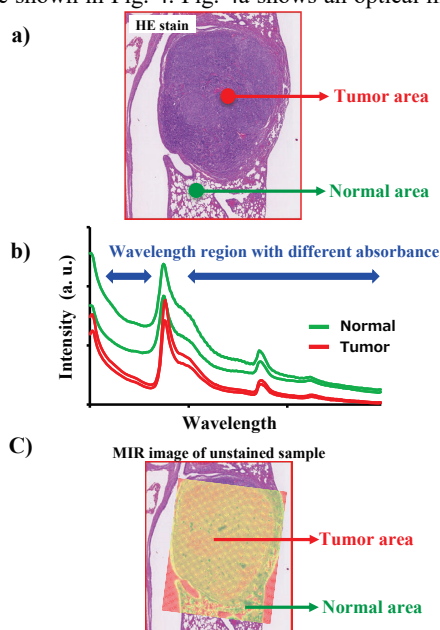


Fig.3. Spectra and visible images of tissue specimen, obtained through MIR microscopy of lung-tumor sample.

- Optical micrograph of an H&E-stained tissue specimen of normal lung and malignant lung tumor.
- Corresponding absorbance MIR spectra of the unstained tissue at two different sites in normal and malignant areas.
- Microscopic and MIR images of normal and malignant area in the unstained specimen.

H&E-stained tissue specimens. The specimens show benign colonic hyperplasia with abundant stroma, dysplastic nuclei, and normal colonic tissue. These different histological areas were analyzed through comparisons with the absorbance obtained from an unstained tissue specimen. The MIR spectra in Fig. 4b demonstrate that the spectral patterns differ between dysplastic nuclei in hyperplastic lesions (red lines), cytoplasm in normal tissue (green lines), and stroma (blue lines). The greatest change in absorbance is observed in the region marked by the black double-headed arrows (Fig. 4b). Next, microscopic mapping was conducted for these tissues to obtain information on the absorbance of each area using the wavelength, demonstrating different absorbances. The area including these tissues was determined by examining the MIR microscopic field and comparing it with the corresponding histopathological view (Fig. 4a). Fig. 4c illustrates the MIR absorbance maps of this area as measured by the wavelength with different absorbances in each region. The color classification result is based on the MIR absorbance colors of the dysplastic nucleus in red, cytoplasm in green, and stroma in blue. The analysis using our constructed MIR microscopic system also permits the detailed detection of noncancerous microlesions.

This study indicates that the MIR spectroscopic technique is useful for diagnosing and discriminating the differences between not only normal tissue and malignant tumors but also noncancerous microlesions. Although MIR spectroscopy has several advantages, it is not yet known whether the spectral information from the proposed device can satisfy the pathological diagnostic requirements and assist pathologists in diagnoses. Thus, further investigation and improvements to the proposed

MIR spectroscopy are necessary for these approaches to become applicable to routine histopathological analysis. In addition, *in-vivo* diagnostic tools using MIR lasers are required in many medical fields. These include endoscopy for guidance in surgical interventions to delineate lesion margins, replacing random

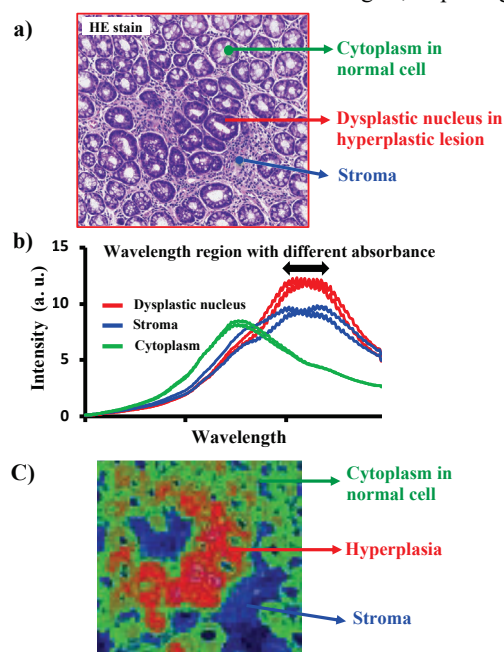


Fig.4. Spectra and visible images of tissue specimen, obtained through MIR microscopy of colonic hyperplasia sample.

- Optical micrograph of an H&E-stained tissue specimen of colonic hyperplasia.
- Corresponding absorbance MIR spectra of the unstained tissue at two sites in the nucleus, cytoplasm, and stroma.
- MIR imaging of colonic hyperplastic lesion in the unstained specimen.

biopsies of suspicious tissue with targeted biopsies, which would reduce unnecessary tissue excisions and risks with biopsy, and using a detection device at a significantly earlier stage of carcinogenesis. Future improvements in MIR laser technology and data analysis will further extend the biomedical applicability and result in the implementation of these innovative techniques in the medical field.

Collaborators

K. Ogawa⁴, T. Imaoka^{2,6}, A. Yokoya^{5,6}, and S. Kakinuma²)
 2) Department of Radiation Effects Research, 4) Light Touch Technology Inc., 5) Tokai Quantum Beam Science Center, 6) Group of Quantum and Cellular Systems Biology, QST Advanced Study Laboratory.

Acknowledgments

We thank M. Ogawa, M. Okabe, M. Fujita, and M. Ootawara from the Department of Radiation Effects Research for assistance in the preparation of histological samples.

This research was supported by QST President's Strategic Grant (Creative Research).

References

- Meier R.J. 2005. *Chem Soc Rev* 34:743-52
- Grasselli JG, Mehicic M, Mooney JR. 1986. *Fresen Z Anal Chem* 324:537-43
- Waynant RW, Ilev IK, Gannot I. 2001. *Philos T Roy Soc A* 359:635-44

Research Activities at the Synchrotron Radiation Research Center

WATANUKI Tetsu

Synchrotron Radiation Research Center



A wide range of X-ray techniques are being developed at the Synchrotron Radiation Research Center (SRRC) to investigate the structural, electronic, and magnetic properties of matter, primarily using two QST beamlines, BL11XU and BL14B1, at the large synchrotron radiation facility, SPring-8. Hard X-ray nondestructive *in-situ* techniques have been investigated to enable ground-breaking measurements using techniques such as single atomic-layer magnetic microscopy, element/orbital-specific excited-state analysis, coherent X-ray nanoscale imaging, and time-resolved studies of samples under extreme conditions such as extremely high pressures of hydrogen gas.

The SRRC consists of the Coherent X-ray Research Group, High-Pressure Science and Stress Research Group, Magnetism Research Group, Condensed Matter Theory Group, and a beamline operation office (Table 1). The research activities of each group are summarized below. Additionally, work has been continuing, from last year, to upgrade the monochromator of BL11XU for reducing beam instabilities and enhancing beam quality.

The equipment developed at SRRC is available for public use and we accepted 37 research proposals in FY2022, as a member institute of the Advanced Research Infrastructure for Materials and Nanotechnology in Japan (ARIM) project [1]. As part of the ARIM project, we have been developing a unified structure for the data generated by the custom-made analysis equipment at our facility with the goal of enabling advanced utilization of data.

Synchrotron and free-electron laser (FEL) X-ray facilities are being constructed at a rapid pace worldwide. The **Coherent X-ray Research Group** is conducting research to ensure state-of-the-art synchrotron/FEL research. Advanced measurement and analysis techniques are being developed for the effective utilization of novel advanced light sources. The application of spatially coherent X-rays has facilitated the visualization of inhomogeneity inside matter.

An apparatus for Bragg coherent X-ray diffraction imaging (Bragg-CDI) is being developed and will be applied to the study of inhomogeneous structures of submicrometer-sized crystalline fine particles of functional materials. This technique has been upgraded for application under high-temperature conditions and has been applied to measure the phase transition of a 500-nm-sized BaTiO₃ single particle [2].

Ultrafast and intense pulses from a soft X-ray FEL source such as SACLA (BL1) facilitate the investigation of processes such as vibration, dissociation, and charge transfer within single molecules. Coulomb explosion imaging (CEI) is one of the most powerful techniques to reveal how electrons move between different atoms within a molecule. The use of CEI has revealed the charge-transfer dynamics in CH₃I and the fragmentation dynamics of 1-iodopropane and 2-iodopropane [3].

A surface X-ray diffractometer coupled with a molecular-beam-epitaxy chamber was used for *in-situ* measurements of the crystal growth of GaN on several types of substrates under the approval of the QST-ARIM project.

The research objectives of the **High-Pressure Science and Stress Research Group** are (i) the development of experimental techniques for *in-situ* measurements under extreme conditions, including high-pressure conditions and in compressed hydrogen gas environments; (ii) fundamental and applied studies of advanced functional materials using the above-mentioned techniques; and (iii) studies on the effects of synchrotron X-ray irradiation on tumors. The research group members focus on the high-pressure synthesis of novel hydrogen-rich compounds and the study of the nano- to mesoscale structures of functional materials, in collaboration with the Coherent X-ray Research Group.

Atomic pair distribution functions (PDFs) are powerful tools for studying the local structures of functional materials. Studying the temperature variations in the local structure is essential for understanding the properties of functional materials. We improved the nitrogen-gas flow-type temperature-control system. This system has been applied to many functional materials such as negative-thermal-expansion oxides, and has contributed to the elucidation of their functional manifestation mechanisms [4]. Metal-hydrogen systems are another research target of this group. The rotation dynamics of complex ions with nine-fold hydrogen coordination, which were synthesized under high pressure, were studied using quasielastic neutron scattering and first-principles molecular dynamics calculations [5]. We clarified that the YH₃ high-pressure phase could be recovered under ambient conditions and investigated the recovery mechanism using *in-situ* synchrotron radiation X-ray diffraction measurements [6]. Additionally, studies have been conducted to investigate the effects of irradiation on tumors, using nanoparticles containing high-Z elements. The effect of X-ray irradiation on tumor spheroids, in which iodine was introduced to enhance the radiation effect, was investigated using synchrotron radiation X-rays ($E = 33.2$ keV) above the iodine K-absorption edge.

The **Magnetism Research Group** develops advanced X-ray spectroscopic techniques such as nuclear resonant scattering (NRS), resonant inelastic X-ray scattering (RIXS), X-ray magnetic circularly polarized emission (XMCPPE), and measurement techniques utilizing measurement informatics, to unveil the key properties of functional materials and devices, ranging from high- T_c superconducting oxides to spintronic devices. For NRS, synchrotron-based high-pressure Mössbauer spectroscopy of EuH₂ utilizing an energy-domain technique, was conducted using a nuclear resonance energy analyzer. The measured spectra suggested that there was little or no hydrogen absorption after the synthesis of *Pnma* EuH₂ in the pressure range up to 5 GPa [7]. This study successfully demonstrated that the relationship between the isomer shift and inverse volume derived from the spectra could be applied to the estimation of the isomer shift change owing to the volume contraction of Eu hydride phases under further extended hydrogen pressure. A RIXS station provides high-energy resolution for both incident and scattered (emitted) X-rays and is used in various advanced X-ray

spectroscopies. We applied high-energy-resolution X-ray absorption spectroscopy to study the electronic structure of Pt catalysts in polymer electrolyte fuel cells under operando conditions [8] and that of a possible candidate for the next-generation solar cell absorber $\text{Cu}_2\text{ZnSnSe}_4$ [9]. XMCPE is a novel magnetic spectroscopy technique operated in the hard X-ray regime with the distinctive feature of a large flipping ratio (25%) for the $K\alpha$ emission of 3d transition metal elements. The magnetic domains in grain-oriented electrical steel were observed using an XMCPE magnetic microscope. Measurement informatics aims to improve the efficiency of measurement and analysis using machine-learning techniques. Modern synchrotron radiation experiments generate tremendous amounts of experimental data, owing to the advances in spatial and temporal resolution techniques. Measurement informatics is helpful for both the generation and analysis of such large volumes of experimental data. This technique is expected to be a part of high-throughput autonomous experiments for the discovery of novel materials.

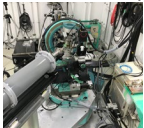
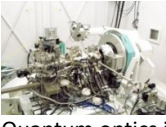





The *Condensed Matter Theory Group* has developed advanced simulation methods based on quantum mechanics to investigate the theory of condensed matter using supercomputers. Additionally, the methods are applied to perform numerical simulations to understand various properties of materials, such as magnetism, high- T_c superconductivity, and catalytic activity, with the support of X-ray experiments such as those from SPring-8. The present activities of this group include (i) the development of advanced simulation techniques based on first-principles path

integral ring-polymer molecular dynamics to investigate the nuclear quantum effects of hydrogen-containing materials such as clathrate hydrates [10]; (ii) the development of a numerically exact diagonalization method to investigate time-resolved spectroscopies of antiferromagnetic Mott insulators, which can provide insights into their electronic dynamics; (iii) the development of a theoretical framework and computational codes to analyze material properties probed by X-ray spectroscopies such as X-ray magnetic circular dichroism (XMCD), RIXS, and XMCPE [11]; and (iv) theoretical investigations using large-scale numerical exact diagonalization of quantum spin systems, which exhibit novel quantum phases such as spin nematic liquids [12].

References

1. <https://www.qst.go.jp/site/arim/> (Accessed: 9 March 2023)
2. N. Oshime *et al.*, Jpn. J. Appl. Phys. **61**, SN1008 (2022).
3. J. W. McManus *et al.*, Phys. Chem. Chem. Phys. **24**, 22699 (2022).
4. L. Hu *et al.*, Chem. Mater., **33**, 7665 (2021).
5. Y. Ohmasa *et al.*, Phys. Rev. Res. **4**, 033215 (2022).
6. R. Kataoka *et al.*, Mat. Today Comm. **31**, 103265 (2022).
7. R. Masuda *et al.*, Hyperfine Interact. **244**, 5 (2023).
8. N. Yamamoto *et al.*, J. Power Sources **557**, 232508 (2023).
9. W. Xu *et al.*, Condens. Matter **8**, 8 (2023).
10. T. Ikeda, Chem. Phys. Lett. **811**, 140252 (2023).
11. H. Kobayashi *et al.*, EPL **140**, 36002 (2022).
12. T. Sakai *et al.*, Phys. Rev. **B** 106, 064433 (2022).

Table 1. Groups at the Synchrotron Radiation Research Center.

Group	Coherent X-ray Research Group	High Pressure Science and Stress Research Group	Magnetism Research Group	Condensed Matter Theory Group
Members	K. Ohwada (GL), J. Harries, T. Sasaki, N. Oshime	H. Saitoh (GL), A. Machida, A. Shiro, Y. Nakahira	T. Inami (GL), T. Mitsui, T. Ueno, K. Fujiwara, (K. Ishii, H. Iwasawa)	(T. Sakai (GL)), T. Ikeda, K. Tsutsui, T. Nomura
Typical techniques & apparatuses	Coherent X-ray scattering  Surface X-ray diffraction  Quantum optics in EUV region	High-pressure and high-temperature X-ray diffraction  Pair distribution function analysis 	Mössbauer spectroscopy  Resonant inelastic X-ray scattering  X-ray magnetic circularly polarized emission	First-principles molecular dynamics simulations, numerical calculations 
Research objective	Ferroelectrics, nitride semiconductors, superfluorescence	Hydrogen-containing materials, negative-thermal-expansion materials, irradiation effects on tumor	Magnetism, spintronics, high- T_c superconductivity, measurement informatics	Hydrogen-containing materials, high- T_c superconductivity, catalysis, magnets
Beamline Operation Office/ Y. Katayama(Section Manager), K. Sugawara, Y. Teraoka, Y. Shimada, A. Shimada, Y. Asai				

Local structural studies using atomic pair distribution function at low temperatures

MACHIDA Akihiko



High Pressure Science and Stress Research Group, Synchrotron Radiation Research Center

1. Introduction

Structural information about a functional material provides important information for understanding its properties. Functional materials cannot be explained by an ideal system, and many of them are inherently inhomogeneous with respect to their composition or structure. X-ray diffraction (XRD) is the most popular method for investigating crystal structures. A long-range structural order can be obtained by analyzing the XRD profile. However, this method is insufficient for analyzing inhomogeneous or heavily disordered structures. An atomic pair distribution function (PDF) represents the interatomic distribution within a material and is a function in real space. The PDF profile corresponds to the probability of finding atom pairs at a distance r ; therefore, PDF analysis¹⁾ is one of the methods suitable for analyzing the local structure in the sub-nanometer to several nanometers scale. This method is generally applied to the structural analysis of nanocrystalline and crystalline materials, as well as noncrystalline materials such as liquids and amorphous materials. Recently, it has been recognized as a powerful tool for investigating the structures of crystalline materials with inhomogeneity or significant disorder.

The PDFs are obtained by Fourier transformation of the total scattering data of the specimens. The rapid acquisition (RA)-PDF measurement²⁾ system in experimental hut 1 of BL22XU at SPring-8 was developed and has been applied to investigate the local structure of various functional materials, such as hydrogen-absorbing alloys³⁻⁶⁾, negative thermal expansion materials⁷⁻¹¹⁾, catalysts^{12,13)}, and cement materials¹⁴⁾. To investigate hydrogen-absorbing alloys, *in-situ* XRD and X-ray total scattering measurements under hydrogen gas up to 1 MPa are available⁵⁾. The hydrogen absorption and desorption properties of hydrogen-absorbing materials, such as maximum hydrogen concentration, absorption/desorption pressure, and hydrogenation reaction rate, vary with temperature. Hence, it is necessary to perform XRD and X-ray total scattering measurements in an environment in which both the hydrogen gas pressure and temperature are controlled. In addition, the local structure of some materials after phase transition differs from the structural model obtained by crystal structural analysis. XRD and X-ray total scattering measurements at low or high temperatures provide essential information for understanding their physical properties. Therefore, we have been developing a measurement system for temperature variations.

2. Rapid-acquisition PDF system with cold nitrogen gas flow apparatus

A nitrogen gas flow apparatus capable of control in the temperature range of 100–400 K was installed in experimental hut 1. This apparatus was mounted on a diffractometer to measure the temperature variations of the XRD or X-ray total scattering patterns of the sample in a capillary. At low temperatures, frost adhered to the capillary, and the X-ray

scattering from the frost (ice) mixed with that from the sample. This excess scattering made analysis difficult. Therefore, a copper wire with good thermal conductivity was wrapped around the capillary so that the frost adhered to the copper wire. Figure 1 shows a photograph of the sample at low temperatures. It can be seen that the copper wire is covered with frost, but there is almost no frost on the capillary.



Figure 1. Photograph of the sample capillary wrapped with a copper wire at low temperature.

Usually, a polyimide capillary with an inner diameter of 1.0 mm (1.2 mm) and outer diameter of 1.1 mm (1.59 mm) is used for *ex-situ* (*in-situ*) X-ray total scattering measurement in BL22XU. During the measurement, the capillary oscillated within a range of 90 or 60°. Therefore, the cold nitrogen gas emitted from the nozzle did not affect the entire circumference of the capillary. To confirm the sample temperature and temperature inhomogeneity in the capillary, the temperature variation in the XRD pattern of Si powder (NIST SRM640d) was measured. An imaging plate was used as the detector for measurements. XRD measurements were performed with a sample-to-detector distance of 730 mm and exposure time of 30 s. Figure 2 shows the XRD patterns of the higher-angle side of the Si powder at 100,

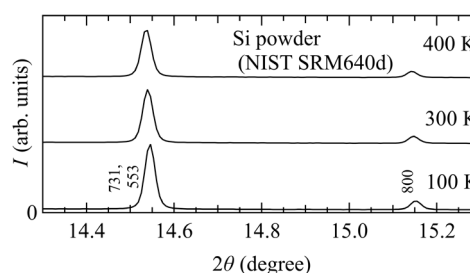


Figure 2. Temperature variation of XRD profiles of the higher-angle side of Si powder. The wavelength of incident X-rays is 0.01789 nm.

300, and 400 K after subtracting the scattering from the polyimide capillary. In the measured temperature range, the linewidths of the diffraction profiles showed no significant broadening and no asymmetry up to the higher-angle side. Therefore, the sample temperature inside the capillary was sufficiently uniform. The sample temperature estimated from the lattice constant was approximately 10 K higher than the set temperature at 200 K and approximately 25 K lower at 400 K.

The PDF profile was transformed from the total scattering data measured at a sample-to-detector distance of 300 mm. Figure 3 shows the result of the curve fitting for the PDF profile of the Si powder at 100 K (set temperature) using the PDFgui program¹⁵. The PDF profile is reproduced by the structural model of silicon well, and this result indicates that the analysis is sufficient, even for data obtained from low-temperature measurements.

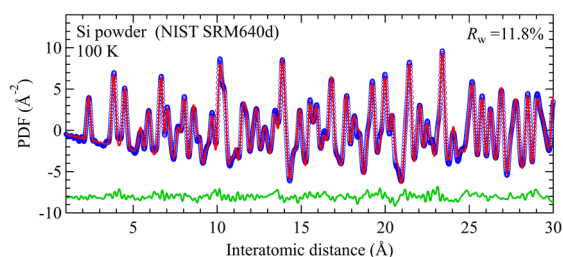


Figure 3. Results of PDF analysis of Si powder at the set temperature of 100 K.

3. Application to the local structural studies of negative-thermal-expansion materials

Most materials increase in length and volume owing to thermal expansion with increasing temperature. Negative-thermal-expansion materials are substances that contract as the temperature increases, and are attracting attention as functional materials that can cancel the thermal expansion that interferes with precise positioning. Prof. Azuma's group at the Tokyo Institute of Technology investigated negative-thermal-expansion oxides and revealed their local structures using our PDF system⁷⁻¹¹. Recently, our system contributed to obtaining the temperature variation of the PDFs of the giant negative-thermal-expansion material Ca_2RuO_4 at 100–400 K¹¹. Ca_2RuO_4 exhibited negative thermal expansion over a wide temperature range of 200 K below 345 K. PDF analysis was used to elucidate variations in the local lattice distortion as the temperature increased and revealed the existence of a peculiar large disorder in Ca_2RuO_4 , related to the giant negative thermal expansion over a wide temperature range.

Acknowledgments

The authors thank Dr. Maejima for his help in installing the nitrogen gas-flow apparatus. PDF measurements of negative-

thermal-expansion materials were performed in collaboration with Prof. Azuma's group at the Tokyo Institute of Technology.

References

1. T. Egami and S. J. L. Billinge, *Underneath the Bragg Peaks: Structural Analysis of Complex Materials*: Pergamon Press Elsevier: Oxford, England, 2003.
2. P. J. Chupas, X. Qiu, J. C. Hanson, P. L. Lee, C. P. Grey, and S. J. L. Billinge, *J. Appl. Crystallogr.* **36**, 1342 (2003).
3. H. Kim, K. Sakaki, H. Ogawa, Y. Nakamura, J. Nakamura, E. Akiba, A. Machida, T. Watanuki, and T. Proffen, *J. Phys. Chem. C*, **117**, 26543 (2013).
4. K. Sakaki, N. Terashita, H. Kim, E. H. Majzoub, A. Machida, T. Watanuki, S. Tsunokake, Y. Nakamura, and E. Akiba, *J. Phys. Chem. C*, **118**, 6697 (2014).
5. K. Sakaki, H. Kim, A. Machida, T. Watanuki, Y. Katayama, and Y. Nakamura, *J. Appl. Crystallogr.* **51**, 796 (2018).
6. H. Kim, H. Schreuders, K. Sakaki, K. Asano, Y. Nakamura, N. Maejima, A. Machida, T. Watanuki, B. Dam, *Inorg. Chem.*, **59**, 6800 (2020).
7. K. Nakano, K. Oka, T. Watanuki, M. Mizumaki, A. Machida, A. Agui, H. J. Kim, J. Komiyama, T. Mizokawa, T. Nishikubo, Y. Hattori, S. Ueda, Y. Sakai, and M. Azuma, *Chem. Mater.*, **28**, 6062 (2016).
8. T. Nishikubo, Y. Sakai, K. Oka, M. Mizumaki, T. Watanuki, A. Machida, N. Maejima, S. Ueda, T. Mizokawa, and M. Azuma, *Appl. Phys. Express*, **11**, 061102 (2018).
9. Y. Sakai, T. Nishikubo, T. Ogata, H. Ishizaki, T. Imai, M. Mizumaki, T. Mizokawa, A. Machida, T. Watanuki, K. Yokoyama, Y. Okimoto, S. Koshihara, H. Das, and M. Azuma, *Chem. Mater.*, **31**, 4748 (2019).
10. T. Nishikubo, Y. Sakai, K. Oka, T. Watanuki, A. Machida, M. Mizumaki, K. Maebayashi, T. Imai, T. Ogata, K. Yokoyama, Y. Okimoto, S. Koshihara, H. Hojo, T. Mizokawa, and M. Azuma, *J. Am. Chem. Soc.*, **141**, 19397 (2019).
11. L. Hu, Y. Zhu, Y.-W. Fang, M. Fukuda, T. Nishikubo, Z. Pan, Y. Sakai, S. Kawaguchi, H. Das, A. Machida, T. Watanuki, S. Mori, K. Takenaka, and M. Azuma, *Chem. Mater.*, **33**, 7665 (2021).
12. Y. Ide, S. Tominaka, H. Kono, R. Ram, A. Machida, and N. Tsunoji, *Chem. Sci.*, **9**, 8637 (2018).
13. Y. Ide, S. Tominaka, Y. Yoneno, K. Komaguchi, T. Takei, H. Nishida, N. Tsunoji, and A. Machida, *Chem. Sci.*, **10**, 6604 (2019).
14. S. Bae, H. Jee, H. Suh, M. Kanematsu, A. Shiro, A. Machida, T. Watanuki, T. Shobu, S. Morooka, G. Geng, and H. Suzuki, *Constr. Build. Mater.*, **237**, 117714 (2020).
15. C. L. Farrow, P. Juhas, J. W. Liu, D. Bryndin, E. S. Bozin, J. Bloch, T. Proffen, and S. J. L. Billinge, *J. Phys.: Condens. Matter*, **19**, 335219 (2007).

Ultrafast dynamics of molecules and nanoparticles studied at SACLA BL1

James R HARRIES

Coherent X-ray Research Group, Synchrotron Radiation Research Centre



Understanding how electrons move within molecules on the femtosecond timescale is at the heart of chemistry, and vital foundational knowledge in fields ranging from energy science to medicine. A technique termed Coulomb Explosion Imaging (CEI) is commonly used to provide near instantaneous ‘images’ of the positions and charge states of all atoms within a molecule, and the soft X-ray beamline (BL1) at SACLA is an ideal source of photons for this technique – providing intense and ultrafast pulses of radiation (pulse width < 100 fs, peak intensity > 10¹⁴ W/cm²) at photon energies ranging from around 20 eV to around 150 eV in first order. Using higher order radiation also gives access to for example the carbon and oxygen K-edges. In CEI the absorption of multiple photons at a particular atomic site leads to the rapid location of charge at that site and the subsequent ‘explosion’ of the molecule or particle due to the large electrostatic forces. By detecting the charge states and momenta of the emitted ions, information can be obtained on the state of the molecule at the time of explosion. With some experimental setups the momenta of emitted electrons can be simultaneously studied. On its own, this technique can be used to study explosion from the electronic ground states of molecules, but its true power is currently being demonstrated by using an earlier pulse of radiation to initiate dynamics in a molecule prior to explosion. By varying the time delay between the ‘pump’ and ‘probe’ pulses, the evolution of the dynamics of the molecule can be followed. At BL1, the technique of CEI can thus be used to study processes such as vibration, dissociation, and charge transfer – how electrons move between different atoms within a molecule.

In this work we have used a technique whereby the momenta of ions produced following Coulomb explosion are detected using an imaging detector and an electrostatic focusing setup with voltages tuned for velocity mapping. Multiple ions can be detected from each event, and covariance analysis is used to study the correlations between different ion species to reveal information on the dynamics of the explosion process and also on any dynamics triggered by an initial pump pulse.

Here we describe in brief the results from two separate experiments performed at BL1, and also briefly discuss future prospects. The experiments were performed as part of a large international collaboration.

1) Charge transfer dynamics in CH₃I [1]

In this experiment gas phase CH₃I molecules were pumped with intense infra-red (IR) pulses at a photon wavelength of 800 nm. Following a variable delay, XUV pulses were used to selectively ionize the I atoms (the chosen photon energy of 95 eV is resonant with excitation of I 4d electrons). Figure 1 shows example results whereby three different processes (I, II, and III) can be identified by studying the kinetic energy released when I⁵⁺ ions are detected. Similar plots for other combinations of fragments, including CH₃²⁺ fragments and I charge states up to I¹⁰⁺ can be found in [1].

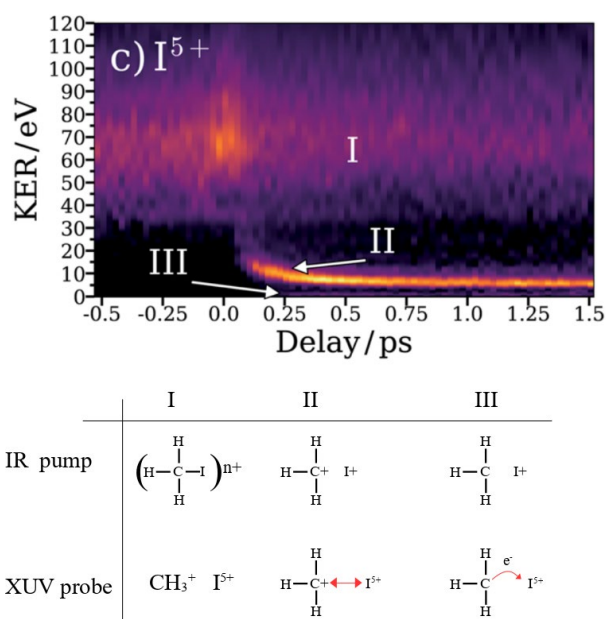


Figure 1 Example results showing the kinetic energy release (KER) as a function of pump-probe delay for I⁵⁺ (adapted from reference 1)

In channel I, high kinetic energy release is observed when the XUV probe interacts with an intact molecule. Enhancement is seen near $\Delta t=0$ (where Δt is the delay between the pump and probe pulses) due to the IR pump leading to multiple ionisations prior to the probe pulse, so that the probe pulse then initiates a Coulomb explosion with high kinetic energy release. At negative delays the neutral molecule is ionized by the XUV pulse alone, and at positive delays this channel is suppressed due to the pump pulse depleting the ground state.

When the initial IR pump leads to dissociation of the molecule into CH₃⁺ and I⁺ fragments, structure at lower kinetic energy release with a time dependence is seen (channel II). In this channel, the two fragments begin to separate (relatively slowly) following the initial dissociation. When the XUV probe leads to a change in charge state of the I⁺ fragment to I⁵⁺, the Coulomb force between the fragments increases, leading to higher observed kinetic energies. This change is time dependent – at longer time delays the I⁺ to I⁵⁺ ionization no longer affects the strength of the force between the fragments due to the increased spatial separation between them.

Channel III is revealed as structure at very low kinetic energy release. Here, the initial IR pump leads to a neutral CH₃ fragment and an I⁺ ion, which start to separate. If the XUV probe creates I⁵⁺ ions at a short enough delay, charge transfer can occur between the fragments (an electron moves from CH₃ to I⁵⁺) and this channel is not observed. The onset of this channel thus

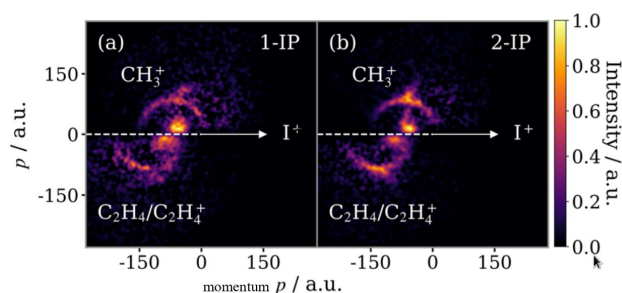


Figure 2 Newton diagrams for the breakup of (a) 1-iodopropane and (b) 2-iodopropane. Adapted from reference 2.

correlates with the ending of this process, and a comparison for different I charge states reveals a charge-state dependence, with charge transfer occurring for longer times (larger separations) for higher charge states. Good agreement was seen with a classical over-the-barrier model for electron transfer. Comparison of the different channels for different ion states and a detailed analysis provides knowledge of dynamics on the potential energy surfaces created by the pump pulse, and this is presented in detail in reference 1.

2) Fragmentation dynamics of 1-iodopropane and 2-iodopropane [2]

In this work the Coulomb explosion of the isomers 1- and 2-iodopropane into the three fragments I^+ , CH_3^+ and CH_2CH_4 (or $CH_2CH_4^+$) was studied in detail. Of interest is the competition between ‘concerted’ and ‘sequential’ pathways. In ‘concerted’ breakup, the three fragments are formed within a time less than a typical vibration period, whereas in ‘sequential’ breakup, the breakup occurs in two steps separated by a time delay during which rotational and molecular dynamics proceed in the molecular fragment. Figure 2 shows example results, where Newton diagrams are plotted. The I^+ momentum is constrained to the positive x-axis, and the CH_3^+ momentum is plotted above the x-axis. Shown below the x-axis is the inferred momentum of the third fragment, either $C_2H_4^+$ or C_2H_4 . In sequential breakup, the molecule has time to rotate between the two dissociation events, revealing ‘arc’-shaped structure for both molecular fragments. For ‘concerted’ breakup, structure is seen perpendicular to the I^+ momentum vector, since rotation does not occur.

By comparing the analysis of the data recorded with detailed simulations, it was possible to study the isomer-specific dynamics of this three body breakup.

3) Future prospects

Pump-probe Coulomb Explosion Imaging is a powerful tool for studying photo-induced dynamics in small molecules and nanoparticles. We are currently working to extend the technique

by using superfluid helium nanodroplets to encapsulate the molecules prior to the pump-probe studies [3]. This ‘freezes’ and isolates the molecules at a temperature of 0.15 K, and will offer the following benefits to the experiments:

- 1) Molecules are cooled to their lowest vibrational and rotational states, allowing pure ground states to be studied
- 2) Signal from helium can potentially be used as a control signal for diffractive imaging
- 3) Detecting fragments with a helium atom attached eliminates background signal

Acknowledgments

The work described here was carried out by a large international collaboration (see author lists of [1] and [2]). Project leaders for the experiments which led to the two publications discussed were Ruaridh Forbes (Stanford) and Kiyoshi Ueda (Tohoku). The experiments were approved by JASRI, and funding sources included JSPS kakenhi, MEXT, and various international funding sources for travel. The development of the helium droplet machine is funded by a QST President's Strategic Grant (Creative Research).

References

1. *Multi-channel photodissociation and XUV-induced charge transfer dynamics in strong-field-ionized methyl iodide studied with time-resolved recoil-frame covariance imaging*. Felix Allum, Nils Anders, Mark Brouard, Philip Bucksbaum, Michael Burt, Briony Downes-Ward, Sven Grundmann, James R Harries, Yudai Ishimura, Hiroshi Iwayama, Leon Kaiser, Edwin Kukk, Jason Lee, Xiaojing Liu, Russell S. Minns, Kiyonobu Nagaya, Akinobu Niozu, Johannes Niskanen, Jordan O’Neal, Shigeki Owada, James Pickering, Daniel Rolles, Artem Rudenko, Shu Saito, Kiyoshi Ueda, Claire Vallance, Nicholas Werby, Joanne Woodhouse, Daehyun You, Farzaneh Ziaee, Taran Driver, Ruaridh Forbes, *Faraday Discussions* **2020-11**, doi:10.1039/D0FD000115E
2. *Disentangling sequential and concerted fragmentations of molecular polycations with covariant native frame analysis*. Joseph W. McManus, Tiffany Walmsley, Kiyonobu Nagaya, James R. Harries, Yoshiaki Kumagai, Hiroshi Iwayama, Michael N.R. Ashfold, Mathew Britton, Philip H. Bucksbaum, Briony Downes-Ward, Taran Driver, David Heathcote, Paul Hockett, Andrew J. Howard, Edwin Kukk, Jason W.L. Lee, Yusong Kiu, Dennis Milesevich, Russell S. Minns, Akinobu Niozu, Johannes Niskanen, Andrew J. Orr-Ewing, Shigeki Owada, Daniel Rolles, Patrick A. Robertson, Artem Rudenko, Kiyoshi Ueda, James Unwin, Claire Vallance, Michael Burt, Mark Brouard, Ruaridh Forbes, Felix Allum. *Phys.Chem.Chem.Phys.*, **24** 22699 (2022)
3. “A new superfluid helium droplet machine”, J R Harries, A Iguchi, S Kuma. Atomic Collision Society 2022 (conference presentation), S Kuma and T Azuma, *Cryogenics* **88**, 78 (2017)

Energy Domain Synchrotron-Radiation-Based Mössbauer Spectroscopy of EuH₂ under a Few GPa Pressure



FUJIWARA Kosuke, MITSUI Takaya, SETO Makoto

Magnetism Research Group, Synchrotron Radiation Research Center

Hydrogen is the smallest atom, and is stored in various materials¹. Recently, various hydrides of rare-earth atoms have been discovered under high-pressure hydrogen conditions. These novel hydrides showed various properties. For example, LaH₁₀ exhibited superconductivity at over 200 K under a hydrogen pressure of more than 100 GPa².

Europium (Eu) metal also forms various hydrides. The structure of Eu metal is $Im\bar{3}m$, that is, body-centered cubic. It forms a dihydride EuH₂, whose structure is orthorhombic $Pnma$ ³, under a hydrogen pressure of approximately 0.1 MPa, that is, 1 atm. This was the only Eu hydride identified in the 20th century. Recently, other forms of hydride have been synthesized under high hydrogen pressures of up to 20 GPa³⁻⁵. In many cases of hydride formation in metals and alloys, the typical process from one hydride to the other by increasing the hydrogen pressure is gradual hydrogen storage by the formation of a solid solution with hydrogen or the coexistence of two phases by spinodal decomposition. However, the hydrogen storage process of Eu at extended pressures is complicated: there are six hydride phases in addition to the initial $Pnma$ phase, and a tetragonal $I4/mmm$ phase is finally formed over 16 GPa. ¹⁵¹Eu energy-domain synchrotron radiation-based Mössbauer spectroscopy (ESRMS)⁶ has been performed to study the electronic state of the Eu atom in these hydride phases and it reveals that Eu was in the 2+ state in EuH₂, the first stage $Pnma$ hydride, and formed a 3+ state in the $I4/mmm$ hydride. Furthermore, the 2+ and 3+ states coexisted in some hydride phases.

This complicated hydride formation process might include more hydrogen storage than that in dihydrides. However, it is difficult to estimate the detailed hydrogen content because these hydrides are synthesized in a diamond anvil cell (DAC). The hydrogen content of the sample in a DAC is sometimes estimated by the volume expansion obtained through X-ray diffraction based on the general empirical rule that the absorption of one H atom into a rare-earth metal lattice induces a volume of $4 \pm 0.5 \text{ \AA}^3$. However, when the metal stores hydrogen gradually, depending on the hydrogen pressure, the lattice expansion by hydrogen storage and lattice contraction by pressure cannot be clearly decoupled. Therefore, another method to estimate the degree of hydrogen storage is required.

When a metal stores hydrogen, its electronic states are modulated. Here, the “isomer shift” in Mössbauer spectroscopy is affected by the electronic density at the probe nucleus and thus, it might provide a useful clue about the degree of hydrogen storage. However, the isomer shift is also affected by the lattice expansion and contraction. The isomer shift δ in the velocity unit is given by the following equation⁷:

$$\delta = \frac{c}{E_\gamma} \cdot \frac{2\pi}{5} Z e^2 (R_e^2 - R_g^2) (\rho_A - \rho_S), \quad (1)$$

where c is the speed of light, E_γ is the energy of nuclear resonance, Z is the atomic number of the element of the probe nuclide, e is the elementary charge, R_e^2 is the square of the nuclear radius of the nuclear excited state concerning the resonance, R_g^2 is the square of the nuclear radius of the nuclear ground state concerning the resonance, ρ_A is the electronic density at the probe nucleus of the sample under study, and ρ_S is the electronic density at the probe nucleus of the energy-standard material, which is often EuF₃ in ¹⁵¹Eu Mössbauer spectroscopy. The electronic state of the sample under study contributes only to ρ_A . Even if there is no change in the electronic states, caused by the electron transfer between the metal and hydrogen, the isomer shift would change through the volume change in hydrogen storage. As the simplest model, we assume that the local density ρ_A is proportional to the inverse of the volume; thus, the dependence of the isomer shift on the inverse of the lattice volume is expressed as a linear function.

In this article, we report the ESRMS of Eu hydride in the pressure region of the initial $Pnma$ hydride, EuH₂, which is below 7 GPa at room temperature³, to evaluate the relationship between the isomer shift and volume contraction. The existence of additional hydrogen storage in this pressure region is also discussed.

The experiments were performed at BL11XU of SPring-8, the beamline of the National Institutes for Quantum Science and Technology (QST), using the ESRMS system installed in the beamline. The samples under study were a piece of Eu metal in hydrogen fluid as a pressure medium in a DAC, or EuH₂ in helium fluid as a pressure medium in another DAC. Both samples were synthesized using a high-pressure gas-loading apparatus at the Japan Synchrotron Radiation Research Institute (JASRI). The energy standard for the ESRMS system was EuF₃ at 80 K. The details of the experimental apparatus are provided in Ref. 8.

The typical ESRMS spectra of the two samples are shown in Fig. 1. The measurement time was typically half a day for each spectrum. All observed spectra were understood by one Eu²⁺ component without hyperfine splitting, which agrees with Refs. 3 and 5. The isomer shifts of both samples increased with increasing pressure. The results of this experiment and those from previous literature are compared in Fig. 2. The volume of the Eu hydride lattice was estimated using the 3rd order Birch-Murnaghan equation of state:

$$P(V) = \frac{3B_0}{2} \left[\left(\frac{V_0}{V} \right)^{\frac{2}{3}} - \left(\frac{V_0}{V} \right)^{\frac{5}{3}} \right] \left\{ 1 + \frac{3}{4} (B'_0 - 4) \left[\left(\frac{V_0}{V} \right)^{\frac{2}{3}} - 1 \right] \right\}, \quad (2)$$

where P and V are the pressure and volume, respectively; B_0 is the bulk modulus; V_0 is the reference volume; and B'_0 is the derivative of the bulk modulus with respect to pressure. We used

the following parameters³: $B_0 = 39.9$ GPa, $V_0 = 42.6 \text{ \AA}^3$, and $B'_0 = 4$.

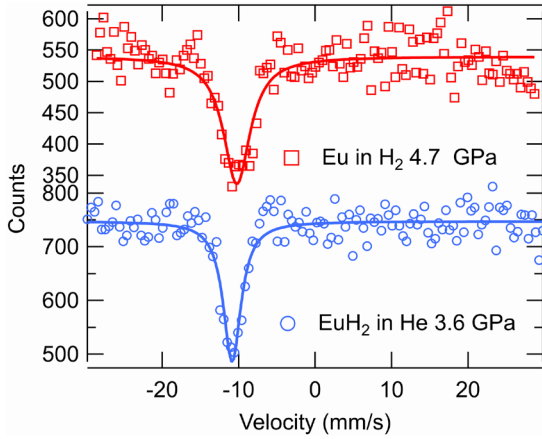


Fig. 1 Typical ESRMS spectra of Eu hydrides, reproduced from Ref. 8. Open symbols are experimental data and the lines are the fitting curve by the Lorentzian function.

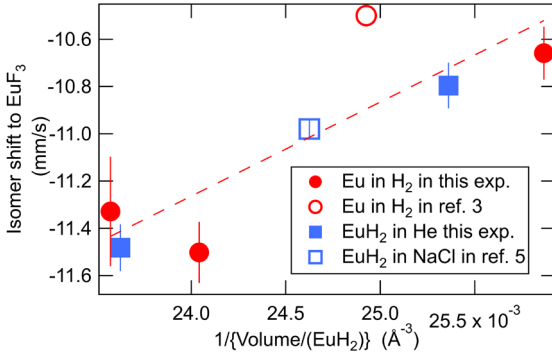


Fig. 2 Relation between the isomer shift of samples and the inverse of the volume of EuH_2 lattice, reproduced from Ref. 8. Filled symbols are the experimental data and the open symbols are those in Refs. 3 and 5. Circles represent the data of Eu metal in the H_2 fluid pressure medium and squares represent that of EuH_2 in the inactive pressure medium. The line is obtained by fitting the linear function using the data in this experiment and refs.

When the pressure increases, one sample, the Eu metal in the hydrogen fluid as the pressure medium, might store more hydrogen, while the other, the EuH_2 in the helium fluid as the pressure medium, would never store more hydrogen. Therefore, if there was some gradual hydrogen storage by increasing the hydrogen pressure, there might be some difference between their isomer shift trends. However, we cannot observe a clear systematic difference between the isomer shifts shown in Fig. 2. This result implies that there is little or no gradual hydrogen storage in this pressure range.

According to the semi-empirical model of isomer shift by Miedema¹¹, hydrogen absorption causes a decrease in the isomer shift in the Eu^{2+} region^{12, 13}. In Fig. 2, we cannot observe a decreasing trend of the isomer shift with the increase in the inverse volume, although there is a non-negligible dispersion of isomer shifts from the fitting curve by the linear function in Fig. 2: $(\text{Isomer shifts in mm/s}) = (4 \pm 1) \times 10^2 ((\text{mm/s}) \cdot \text{\AA}^3) \times (\text{Inverse volume in \AA}^{-3}) - 21 \pm 3 (\text{mm/s})$. This also

supports the absence of gradual hydrogen absorption.

As described in the beginning of this report, there are various hydride phases under a hydrogen pressure higher than that used in this experiment. If we assume that the electronic structure is not strongly modified in these hydride phases at which Eu shows a $2+$ state, the effect of volume on the ^{151}Eu isomer shift in these phases would be similar to that in this experiment. Therefore, we can investigate the existence of gradual hydrogen absorption at higher hydrogen pressures using the linear dependence of the isomer shift on the inverse volume obtained in this experiment.

Acknowledgments

The authors would like to thank the Accelerator Group of SPring-8 for their support, especially with the operation of several electron bunch modes and top-up injection operation. This work was supported by QST through the QST Advanced Characterization Nanotechnology Platform under the remit of "Nanotechnology Platform" of the Ministry of Education, Culture, Sports, Science and Technology (MEXT), Japan and the QST Advanced Research Infrastructure for Materials and Nanotechnology under the remit of "Advanced Research Infrastructure for Materials and Nanotechnology" of the MEXT, Japan (Proposal Nos. A-JPMXP09A21QS0023, JPMXP1222QS 0002). The synchrotron radiation experiments were performed using a QST experimental station at QST beamline BL11XU with the approval of the JASRI (Proposal Nos. 2021B3581, 2022A3581). This research was also supported by joint-use research program of Institute for Integrated Radiation and Nuclear Sciences, Kyoto University (KURNS) (Proposal No. R3P7-11).

References

1. Fukai, Y.: The Metal-Hydrogen System second edition, Springer-Verlag Berlin Heidelberg (2005).
2. Drozdov, A. P., Kong, P. P., Minkov, V. S., Besedin, S. P., Kuzovnikov, M. A., Mozaffari, S., Balicas, L., Balakirev, F. F., Graf, D. E., Prakapenka, V. B., Greenberg, E., Knyazev, D. A., Tkacz, M., Erements, M. I.: *Nature* **569**, 528-531 (2019).
3. Matsuoka, T., Fujihisa, H., Hirao, N., Ohishi, Y., Mitsui, T., Masuda, R., Seto, M., Yoda, Y., Shimizu, K., Machida, A., Aoki, K.: *Phys. Rev. Lett.* **107**, 025501 (2011). See also Matsuoka, T., Fujihisa, H., Hirao, N., Ohishi, Y., Mitsui, T., Masuda, R., Seto, M., Yoda, Y., Shimizu, K., Machida, A., Aoki, K.: *Phys. Rev. Lett.* **122**, 179901(E) (2019).
4. Saitoh, H., Machida, A., Matsuoka T., Aoki, K.: *Solid State Comm.* **205**, 24-27 (2015).
5. Kuno, K., Matsuoka, T., Masuda, R., Mitsui, T., Seto, M., Machida, A., Fujihisa, H., Hirao, N., Ohishi, Y., Shimizu, K., Sasaki, S.: *J. Alloys Compd.* **865**, 158637 (2021).
6. Seto, M., Masuda, R., Higashitaniguchi, S., Kitao, S., Kobayashi, Y., Inaba, C., Mitsui, T., Yoda, Y.: *Phys. Rev. Lett.* **102**, 217602 (2009).
7. Gülich, P., Bill, E., and Trautwein, A. X.: *Mössbauer Spectroscopy and Transition Metal Chemistry Fundamentals and Applications*, Springer-Verlag Berlin Heidelberg (2011).
8. Masuda, R., Hirao N., Fujiwara, K., Mitsui, T., Fujihara, T., Yamashita, H., Tajima, H., Kurokuzu, M., Kitao, S., Seto, M.: *Hyperfine Interact.* **244**, 5 (2023).
9. Miedema, A. R., van der Woude, F.: *Physica* **100B**, 145-156 (1980).
10. de Vries, J. W. C., Thiel, R. C., Buschow, K. H. J.: *Physica* **121B**, 100-108 (1983).
11. Niessen, A. K., de Boer, F. R., Boom, R., de Châtel, P. F., Mattens, W. C. M., Miedema, CALPHAD **7**, 51-70 (1983).

Comparative theoretical study on X-ray magnetic circularly polarized emission

KOBAYASHI Hiroki

Condensed Matter Theory Group, Synchrotron Radiation Research Center



The mechanism of characteristic X-ray emission is well known: Characteristic X-rays are emitted when a core hole is annihilated by the transition of an electron from a higher energy level to a core level. Because each element has a unique set of core levels, characteristic X-rays have specific energies for each element. The spectroscopy of characteristic X-rays is known as X-ray emission spectroscopy (XES). Recently, Inami reported, for the first time, that the intensity of characteristic X-ray emission from magnetized materials differs between right- and left-handed circular polarizations [1]. We refer to this novel X-ray magneto-optical effect as the X-ray magnetic circularly polarized emission (XMCPE).

The mechanism of XMCPE in the $K\alpha$ emission of $3d$ transition-metal (TM) systems is as follows. First, an incident X-ray photon creates a $1s$ core hole by exciting a $1s$ electron into a free electron state. Subsequently, the $1s$ core hole is annihilated by a $2p \rightarrow 1s$ transition, emitting a characteristic X-ray photon. In $3d$ TM systems, the $2p$ states are usually split into $2p_{1/2}$ (L_2) and $2p_{3/2}$ (L_3) by the $2p$ spin-orbit coupling, regardless of the magnetic state, which leads to $K\alpha_2$ and $K\alpha_1$ XES peaks, respectively. Furthermore, in ferromagnetic $3d$ TM systems, the magnetic polarization of the $2p$ states is induced by that of the $3d$ states through the $2p$ - $3d$ Coulomb interaction (exchange part). Therefore, electron transitions from the polarized $2p$ states to the $1s$ state have different transition probabilities, and the emitted X-rays have different intensities between right- and left-handed circular polarizations.

The first XMCPE experiment described in Ref. [1] was performed for magnetized Fe. We previously analyzed the XMCPE spectra in ferromagnetic Fe, using the Keldysh Green's function technique for nonequilibrium states [2]. According to this analysis, electron excitations that remain in the spin-polarized $3d$ conduction bands in the final states, that is, many-body effects, appear as significant characteristic tail structures on the low-energy sides of the $K\alpha$ emission peaks.

Previous XMCPE experiments and theoretical analyses have only been performed for Fe [1-3]. Therefore, to further promote the XMCPE technique as a powerful tool for studying ferromagnetic materials, it is necessary to investigate the XMCPE in ferromagnetic materials other than Fe. In this study, we calculated the XMCPE with $K\alpha$ emission for ferromagnetic Fe, Co, and Ni, using our method [2].

We found that the calculated XMCPE spectra had characteristic tail structures that appeared on the low-energy side of the $K\alpha$ emission peaks for all three ferromagnets. These tail structures originated from the energy loss of emitted X-rays due to electron excitations in $3d$ bands. A comparison of these three ferromagnets shows that Fe, Co, and Ni have broad, intermediate, and narrow tail structures, respectively, in the XMCPE spectra. As will be explained, this difference in tail structure broadness arises from the difference in the spin-polarized $3d$ electron states among the three ferromagnets [4].

In the theoretical calculation, we first performed first-

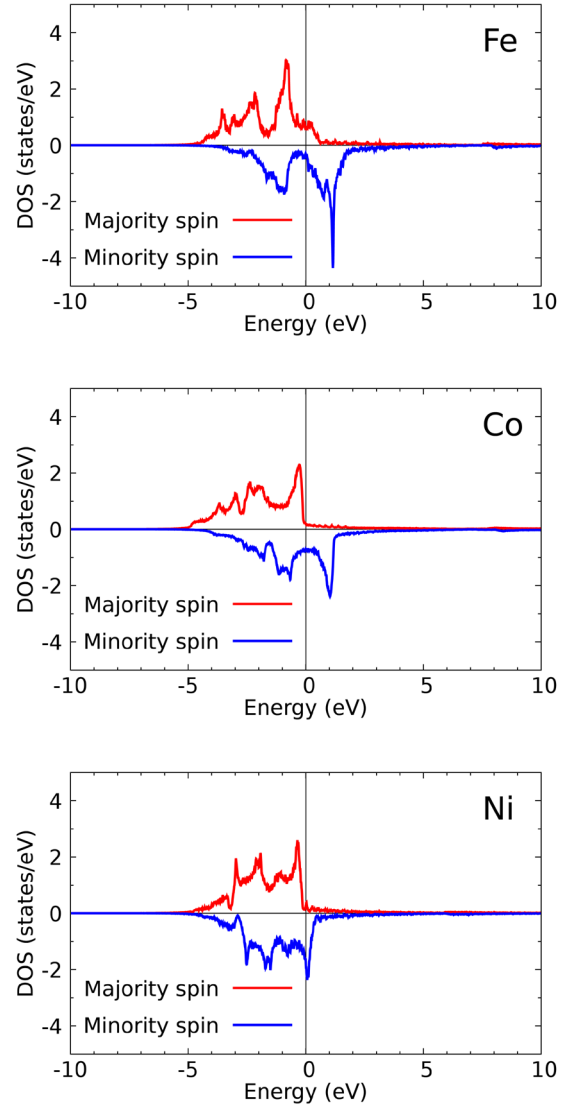


Fig. 1: Calculated spin-polarized $3d$ partial DOS for Fe (upper panel), Co (middle panel), and Ni (lower panel). Red and blue lines represent the DOS for majority and minority spin states, respectively. The Fermi level is set to 0 eV.

principles band-structure calculations for Fe, Co, and Ni without spin polarization, and then constructed tight-binding models based on the maximally localized Wannier functions. Considering only the on-site Coulomb interactions for the $3d$ orbitals, we obtained multiorbital Hubbard models. The $3d$ on-site Coulomb interactions are parameterized by the intra-orbital

term U , inter-orbital term U' , and exchange term (Hund's coupling) J . The calculated $3d$ partial density of states (DOS) for each $3d$ TM in the ferromagnetic state are shown in Fig. 1.

In Fig. 2, we present the calculated XMCPE spectra, which are the difference spectra between the right- and left-handed circularly polarized emission intensities, for Fe, Co, and Ni, where the bare part $I^{(0)}$ and the many-body correction part $I^{(1)}$. In the upper panel of Fig. 2 for Fe, the experimental data from Ref. [3] are plotted for comparison with the theoretical data and the calculated spectrum is in good agreement with the experimental spectrum. Note that, in all cases of Fe, Co, and Ni, the difference spectra have characteristic tail structures on the low-energy side of the $K\alpha$ peaks. These tail structures originate from $I^{(1)}$. By comparing the spectra, it is found that the tail structures were broad, intermediate, and narrow for Fe, Co, and Ni, respectively. It can be understood that this difference originates from the differences in the $3d$ electron states, considering that $I^{(1)}$ includes the dynamical correlation function $\Pi(\omega)$:

$$\Pi(\omega) = \int d\varepsilon D^+(\varepsilon)D^-(\varepsilon + \omega),$$

where $D^{+/-}(\varepsilon)$ is the $3d$ occupied/unoccupied DOS. $\Pi(\omega)$ describes the $3d$ electron excitations across the Fermi level. Thus, the width of the tail structure is determined by the energy range of the $3d$ electron transitions from an occupied state to an unoccupied state. To confirm the difference in these electron excitation energies, we closely examined the $3d$ DOS. As seen in Fig. 1, the minority spin states of Fe and Co have a relatively large $3d$ unoccupied DOS over a relatively wide energy range. In contrast to Fe and Co, the minority spin states in Ni have only a small amount of $3d$ unoccupied DOS over a narrow energy width. Therefore, the range of electron excitations in the $3d$ bands in Ni is restricted to be much narrower than those in Fe and Co.

From above, the spectral tail broadness shows a notable material dependence, reflecting the difference in the $3d$ electronic states among the three ferromagnets because the electron excitations in $3d$ bands mainly determine $I^{(1)}$, which dominates the total XMCPE spectral structure. In Fe, there are sufficient $3d$ unoccupied DOS above the Fermi level; therefore, $3d$ electron excitations across the Fermi level are allowed. In addition, the $3d$ unoccupied DOS have a relatively broad bandwidth. In Ni, the majority spin states are filled, and the minority spin states have only slight $3d$ unoccupied DOS, in contrast to that of Fe. In addition, the $3d$ unoccupied DOS have a narrow bandwidth. These features of Ni greatly restrict the possible energy range of electron excitations in the $3d$ bands. Therefore, the XMCPE spectra of Fe have broad tail structures, while that of Ni have the narrow tail structures.

Although our calculations for Co and Ni were only predictive, we calculated the XES spectra in Ref. [4] and demonstrated that the calculated spectra agreed with the experimental spectra. The consistency of our calculated XES spectra with those of existing experiments lends credence to the predictive calculations [4].

In conclusion, the results of the present comparative theoretical study suggest that the XMCPE spectra show remarkable material dependence and that XMCPE spectroscopy is a powerful tool for characterizing various magnetic materials.

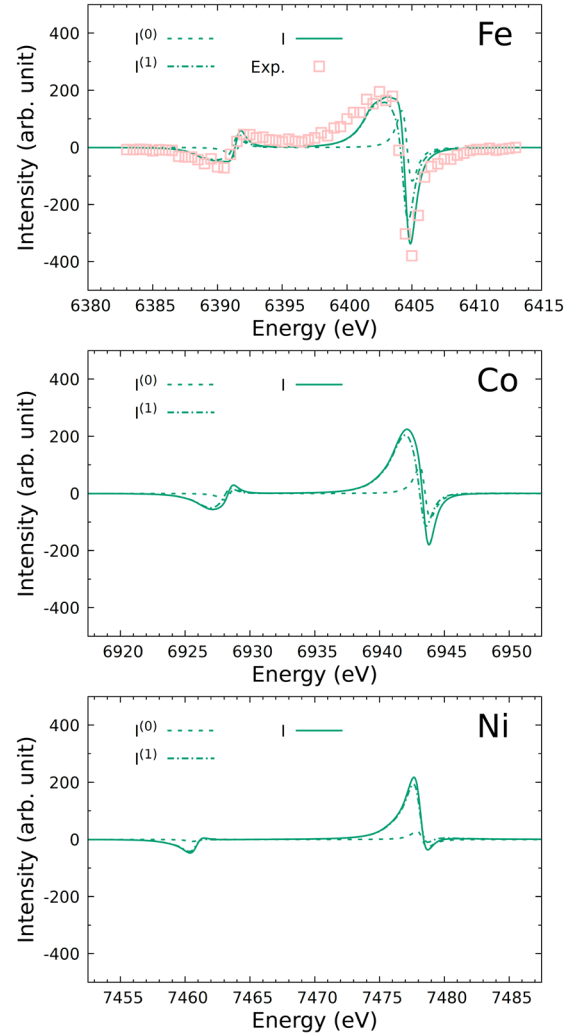


Fig. 2: Calculated XMCPE spectra for Fe (upper panel), Co (middle panel), and Ni (lower panel). In each panel, dotted and dashed lines represent the bare part $I^{(0)}$ and the many-body correction part $I^{(1)}$, respectively. The total spectra $I (= I^{(0)} + I^{(1)})$ are shown by solid lines. In the upper panel (for Fe), the experimental data are plotted [3].

Acknowledgments

The author is grateful to Dr. T. Inami, Dr. T. Nomura, and Dr. A. Koide for their invaluable comments.

References

- [1] T. Inami, *Phys. Rev. Lett.* **119**, 137203 (2017).
- [2] A. Koide T. Nomura, and T. Inami, *Phys. Rev. B* **102**, 224425 (2020).
- [3] K. Sugawara, T. Inami, T. Nakada, Y. Sakaguchi, and S. Takahashi, *J. Appl. Phys.* **130**, 113901 (2021).
- [4] H. Kobayashi, A. Koide, T. Nomura, and T. Inami, *EPL* **140**, 36002 (2022).

Research Activities at the Institute of Quantum Life Science at KPSI



SHIKAZONO Naoya

Institute of Quantum Life Science

Quantum life science has emerged to explore new frontiers in biology from the perspective of dynamics and functions of cellular processes at the quantum level. The Institute of Quantum Life Science at the National Institutes for Quantum Science and Technology (QST) was established in April 2019 to pioneer a new field in life sciences. Investigations at the Institute of Quantum Life Science are expected to follow two approaches: The first approach is to determine whether quantum mechanics plays an essential role in biological systems. The second approach is to apply quantum science and its technologies for measuring physical and chemical parameters (i.e., temperature, pressure, and pH) inside a cell at an unprecedented minute level to gain information on the structure and dynamics of biomolecules. Using the above two approaches, the goal of the Institute of Quantum Life Science is to discover the essential principles of life and apply the knowledge attained during the course of investigation to medical sciences and social activities (Fig. 1). The field of quantum life science is envisaged to produce unanticipated discoveries that will expose the existence of quantum phenomena in nature, ultimately leading to their exploitation, which in turn, would benefit society. At the Kansai Photon Science Institute (KPSI), three research teams with the Institute of Quantum Life Science are conducting research using experiments and computer simulations (Fig. 1).

The Molecular Modeling and Simulation Team aims to understand the *in-vivo* function of biomolecules at the atomic level. The team uses computer simulations and bioinformatics based on experimental results such as crystallographic and scattering data obtained using various types of radiation (X-rays, neutrons, and electrons) and cryo-electron microscopy. The main objective of their study is to determine how the dynamics of protein/DNA/RNA complexes relate to essential cellular functions such as transcription, translation, replication, and repair. The team is now trying to quantitatively predict the dynamics and stability of supramolecular complexes such as chromosomes. This year, the research team carried out a simulation to elucidate the initial step of nucleosome reconstitution, which is considered to be involved in many vital cellular processes such as transcription, replication, and chromatin remodeling. Nucleosomes are fundamental structural units of chromosomes. In a nucleosome, DNA wraps around the octameric histone core, which are composed of two sets of histone H3, H4, H2A, and H2B proteins. The key step in nucleosome reconstitution is the dissociation of the H2A–H2B dimers from the nucleosome and their reassembly. However, the molecular mechanism underlying the displacement of the H2A–H2B dimer from the nucleosome is unknown. Therefore, the research team conducted detailed molecular dynamics simulations to reveal the molecular process. First, they generated various distinct conformations of H2A–H2B and DNA, which represent fully wrapped and partially unwrapped nucleosome structures. They found that the docking domain of H2A and C-terminal of H4 were the main contributors to the displacement. Furthermore, they clarified that there were

multiple paths for displacement that were dependent on the level of DNA wrapping around the histone core. This suggested that external factors such as histone chaperones could regulate the path of the H2A–H2B dimer displacement by modulating the intranucleosomal interactions between DNA and histones and/or between H2A–H2B dimer and H3–H4 dimer in the nucleosome. Importantly, the essential residues for intranucleosomal interactions coincided with the sites of mutations and post-translational modifications of histones, which were known to play essential roles in assembling and/or reassembling the nucleosome. Their results provide important insights into how the H2A–H2B dimer displacement and nucleosome reconstitution proceed along various paths that are based on the interactions within the nucleosome [1]. More details of these of these processes are described in the subsequent report.

The main goal of the DNA Damage Chemistry Team is to clarify the nature of DNA damage induced by various agents, particularly ionizing radiation. The team aims to utilize new experimental techniques that can reveal the structure and/or spatial distribution of DNA damage at the nanometer scale. The focus of this team is currently on “clustered DNA damage,” in which two or more DNA lesions are located within one to two helical turns of DNA (within several nanometers of the DNA). Repair of clustered DNA damage is considered to be challenging; thus, it is potentially a detrimental type of damage induced by ionizing radiation. However, its presence and microstructure remain elusive, as few experimental methods have been able to obtain data on the spatial distribution of DNA lesions. This research team established a novel approach for detecting the level of DNA damage localization through direct visualization. Atomic force microscopy (AFM) has a resolution at the nanometer/sub-nanometer scale; thus, DNA can be directly visualized using AFM. They labeled DNA damage (abasic sites) by attaching aldehyde reactive probes with biotin to abasic sites and then attaching streptavidin to biotin. The large molecular size of streptavidin enabled the detection of the site of damage using AFM. Abasic sites were directly induced or further revealed by removing the damaged bases by DNA glycosylases after irradiation. Using this method, the complex nature of clustered DNA damage could be visualized. They found that various types of clustered DNA damage were generated: clusters that contained two base lesions, more than two base lesions, and double-strand breaks (DSBs) that accompanied base lesions [2]. They further verified that the repair ability of clustered DNA damage was compromised. X-ray induced clusters with more than two base lesions could be repaired, but the repair rate was slightly lower than that of other types of clustered DNA damage. Fe-ion induced clusters with base damages could also be repaired, but their repair rates were lower than those with isolated base damage. The repair of DSBs with base damage was markedly retarded. Surprisingly, the number of DSBs increased after 1 h of incubation, following which they decreased slowly. A detailed description is provided in the following report. The research team further developed a

Institute of Quantum Life Science

Using cutting-edge quantum technologies and advanced computer simulations, the Institute aims to contribute to the (1) elucidation of the basic principles of life, and in longer term, (2) improving the everyday life of the society.

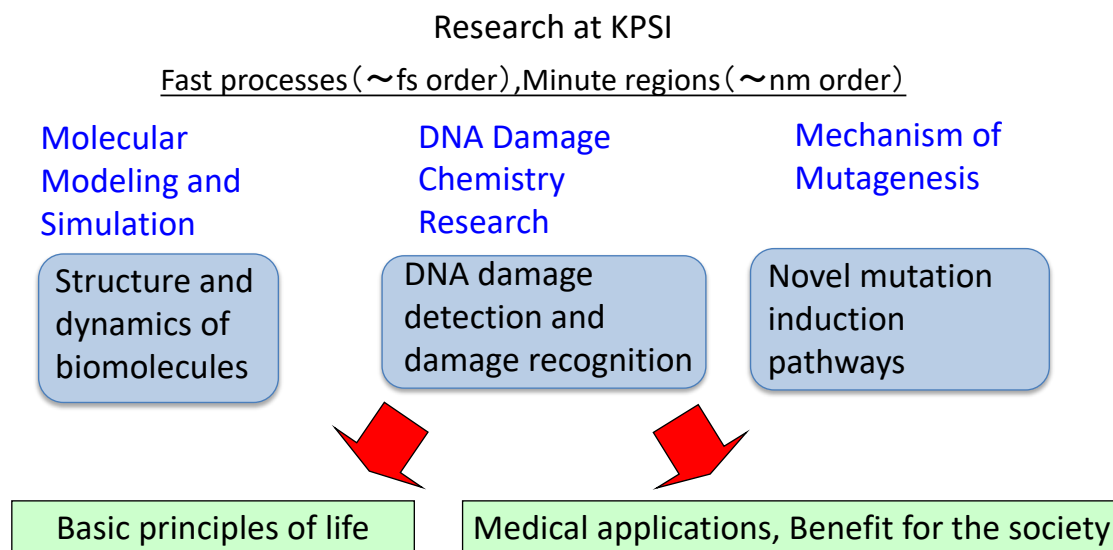


Figure 1.

promising method for detecting clustered DNA damage using fluorescence resonance energy transfer (FRET). In this method, aldehyde/ketone moieties such as those at the abasic sites in irradiated DNA were labeled by aminooxyl fluorophores. Fluorescence anisotropy facilitated the estimation of the apparent base-pair separations between lesions in a cluster produced by an ion track and revealed that the yield of clustered abasic sites increased upon increasing the linear energy transfer (LET) of radiation. Both AFM and FRET approaches confirmed that these novel analyses had the potential to discover qualitative and quantitative differences in clustered DNA damage produced by various types of ionizing radiation.

The goal of the Mechanism of Mutagenesis Team is to elucidate the underlying mechanisms causing mutations, which are highly relevant to carcinogenesis and the evolution of life. One aspect of this team's research focuses on events at very early stages (around a femtosecond to picosecond), within a space in the scale of nanometers, after energy transfer from ionizing radiation, particularly ions. Using Monte Carlo simulations, the research team demonstrated that, when water was exposed to densely ionizing ion particles, some of the secondary electrons ejected from the water molecules were trapped within the electric potential created by the ionized water molecules. This result led to the realization that the radial dose near the track of a densely ionizing ion particle was much higher than that previously considered. This highly localized energy deposition is likely to produce a high yield of clustered DNA damage and thus, has important implications regarding the drastic effect of ion particles on cells. The research team took a further step to determine whether this unique type of energy deposition would be relevant to the biological effects of radiation. As most of the deposited energy is eventually converted to heat, extreme heat in a very localized space may lead to the generation of a strong pressure wave, which has the potential to damage nearby DNA. As water

constitutes 60–70% of a cell, the research team first conducted a molecular-dynamic simulation of water, in which extreme heat was introduced within a very localized volume at time zero. They found that after several picoseconds, the density of water molecules around the site of the injected heat was markedly reduced. This result strongly suggests that a pressure wave was produced by energy deposition. The team is currently investigating the relationship between the amount of deposited energy (=heat) and density of water around the injected heat.

Quantum life science is related to the interactions between dynamical phenomena at extremely short time scales and minute length scales; that is, from atto to femtosecond energy transfer processes at the (sub)nanometer scale. Over the long term, the field of quantum life science is expected to produce unparalleled discoveries based on the significance of quantum phenomena in biological systems. To achieve such goals, the research of the three teams of the Institute of Quantum Life Sciences at the KPSI is ongoing.

References

1. Ishida, H. and Kono, H. Free Energy Landscape of H2A-H2B Displacement From Nucleosome. *J. Mol. Biol.* 434, 167707 (2022)
2. Nakano, T., Akamatsu, K., Tsuda, M., Tujimoto, A., Hirayama, R., Hiromoto, T., Tamada, T., Ide, H., Shikazono, N. Formation of clustered DNA damage in vivo upon irradiation with ionizing radiation: Visualization and analysis with atomic force microscopy. *Proc. Natl. Acad. Sci. USA.* 119 (13) e2119132119 (2022)
3. Moribayashi, K., Matsubara, H., Yonetani, Y., Shikazono, N. Multi-scale simulations aiming to advance heavy ion beam cancer therapy. *Proc. AIP Conf. Series.* Accepted.

Important Residues for Stabilizing Nucleosome Core Particles

ISHIDA Hisashi and KONO Hidetoshi

Molecular Modeling and Simulation Team, Institute for Quantum Life Science



Our team is interested in the regulation of genomic DNA function at the molecular level. Computer simulation is one of the most powerful and useful methods to elucidate the mechanism of the genomic DNA function, because no other experimental method can capture the structure and dynamics of molecules in such detail.

The genomic DNA of eukaryotes is compactly stored in the nucleus and folded into chromatin, which is a high-order structure. However, decomposition of the chromatin structure is required for gene expression in cellular processes such as transcription, replication, repair, and recombination. The nucleosome is the fundamental structural unit of chromatin and is composed of two each of H3, H4, H2A, and H2B histone proteins and 146 or 147 bps DNA wrapped 1.75 times around the octameric histone core.

The nucleosome has been experimentally shown to be highly dynamic and undergoes structural changes such as DNA breathing, nucleosome unwrapping, rewrapping, gapping, sliding, assembly, disassembly, and histone exchange. The transient detachment of one or both H2A–H2B dimers from the nucleosome and reassembly with the aid of RNA polymerase II and/or histone chaperones appears to be involved in many vital cellular processes such as transcription, replication, and remodeling.

For the H2A–H2B displacement from the nucleosome, the H2A–H2B dimer should be separated from the two H3–H4 heterodimers. In the H2A–H2B dimer, H2A has a long disordered

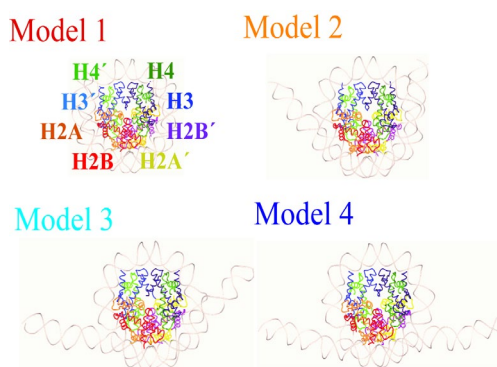


Fig. 1 Four models with distinct DNA wrapping states for the analysis of the H2A–H2B dimer displacement from the nucleosome.

H2A (orange) and H2B (red), and H3 (blue) and H4 (green) bind to each other to form H2A–H2B and H3–H4 heterodimers, respectively. Two H3–H4 heterodimers further bind together to form a (H3–H4)₂ tetramer. Two H2A–H2B heterodimers bind on both sides of the (H3–H4)₂ tetramer to form the histone octamer, H2A–H2B–H4–H3–H3′–H4′–H2B′–H2A′, where the prime is used to distinguish two copies of each histone protein. H2A interacts with the opposite H2A′. In the nucleosome, DNA wraps the H2A–H2B–H4–H3–H3′–H4′–H2B′–H2A′ and H2A–H2A′, which forms ~ 1.7 turns of a left-handed superhelix.

C-terminal tail. A domain in the C-terminal tail, the docking domain, stabilizes the intranucleosomal interactions between H2A and H3–H4. However, it is not yet well known at the atomic level how the dynamic disruption of the intranucleosomal interfaces for the H2A–H2B displacement from the wrapped or unwrapped DNA occurs and how the dynamic disruption is affected by the functionally important residues.

To understand how the disruption occurs and depends on the DNA wrapping, we examined the H2A–H2B dimer displacement from the nucleosome by all-atom molecular dynamics simulations [1]. We conducted adaptively biased molecular dynamics (ABMD) simulations on nucleosomes in which DNA is tightly wrapped to unwrapped states, resulting in four models (Fig. 1).

For each of the four models, we carried out umbrella sampling simulations of distinct H2A–H2B dimer displacement from the nucleosome to obtain

the free-energy curves (FEC) of the H2A–H2B displacement against the distance d between the two centers of mass of the H2A–H2B and H2A′–H2B′ dimers. (Fig. 2). Fig. 2 shows that the free energies rapidly increased from the minimums (denoted by crosses in the figure), –41.1, –38.9, –37.1, and –30.6 kcal/mol at $d = 37$ Å for models 1–4, respectively. This indicated that the H2A–H2B displacement was more likely to occur from the nucleosome with unwrapped DNA (models 2, 3, and 4) than from the nucleosome with wrapped DNA (model 1).

Important residues that contributed to the free energy were found to be involved in the mutations and posttranslational modifications (PTMs), which are important for assembling and/or reassembling the nucleosome at the molecular level and are found in cancer cells at the phenotypic level.

(1) H2A–H2B – H2A′–H2B′ dimer interaction

Asn38 and Glu41 of H2A were found to be important residues for the interaction between H2A–H2B and H2A′–H2B′ (Fig. 3(a)).

These mutations

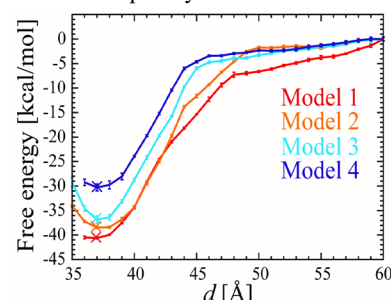


Fig. 2 Free-energy curves of the H2A–H2B dimer displacement against d .

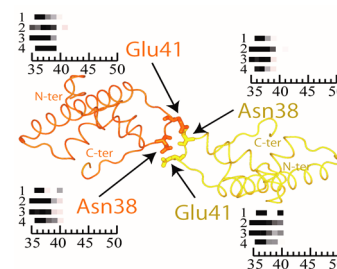


Fig. 3(a) Important residues at H2A–H2B – H2A′–H2B′ dimers interface. Bar graph shows frequency of interaction between the dimer (high: black; white: low) against the reaction coordinate for each of the four models.

would perturb the interface at the first stage of the H2A–H2B displacement at $d \sim 41$ Å and have an impact on the free-energy component for the interaction of ~ 5 kcal/mol.

(2.1) H2A docking domain – H3' α N and α 2 helices interaction

Lys56 and Thr58 in H3' α N, Ala98 in H3 α 2, and Arg81 and Thr101 in the H2A docking domain were found to be important residues for the interaction between the H2A docking domain and the H4' C-terminal domain (Fig. 3(b)).

These mutations would disrupt the H2A docking domain – H3' α N-helix interface at $d = \sim 42$ – 45 Å and have an impact on the free-energy component for the interface of ~ 5 kcal/mol.

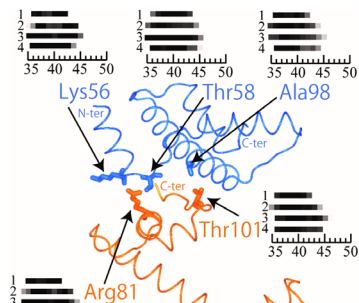


Fig. 3(b) Important residues at the H2A–H2B – H3' interface.

(2.2) H2A docking domain – H4' C-terminal interaction

Arg99, Val100, and Thr101 in the H2A docking domain and Lys97, Tyr98, and Gly99 of the H4' C-terminal were found to be important residues for the interaction between the H2A docking domain and H4' C-terminal, in this study (Fig. 3(c)).

In humans, Arg99 in H2A, which interacts with the H4 C-terminal tail, is substituted for lysine in H2A isoforms encoded by the H2AC7, H2AC18, H2AC12, H2AC14, and H2AC20 genes, and these H2A isoforms are involved in carcinogenesis [2]. Lys99Arg of the H2A isoform encoded by HIST1H2AH in rats has shown a significant effect on cell proliferation [3].

These mutations can disrupt the interface between the H4 C-terminal and the H2A docking domain up to $d = \sim 49$ Å and affect the free-energy component for the interaction at ~ 6 kcal/mol.

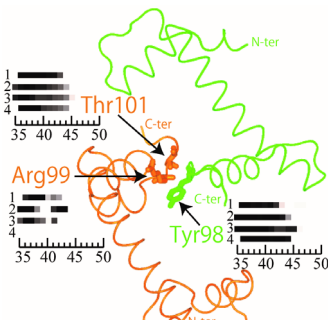


Fig. 3(c) Important residues at the H2A–H2B – H4' C-terminal interface.

(2.3) H2B α 2 helix – H4' C-terminal interaction

Ser61 and Asp65 in H2B α 2 and Tyr98 in the flexible H4' C-terminal were found to be important residues for the interaction between H2B and H4' C-terminal (Fig. 3(d)).

Mutations in Ser61 and Asp65 of the H2B α 2 helix (corresponding to Ser64 and Asp68 in humans) have frequently been found in cancer patients [4] [5]. Our simulation showed that

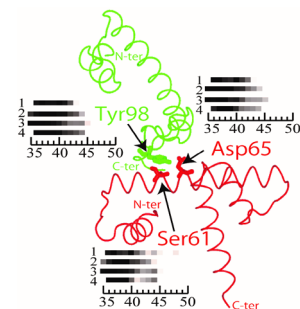


Fig. 3(d) Important residues at the H2B – H4' C-terminal interface.

the H4' C-terminal also maintained a persistent interaction with the H2B α 2 helix up to $d = \sim 48$ Å. These mutations would perturb the H2B – H4' C-terminal interactions and have an impact on the free-energy component for the interaction at ~ 7 kcal/mol.

(3) H2A–H2B – H3–H4 interaction

Glu73, Tyr80, Arg89, and Arg96 in H2B and Asp68, Tyr72, Lys77, and Arg92 in H4 were found to be important residues for the interactions in the H2A–H2B – H3–H4 (Fig. 3(e)).

The Glu73 and Arg96 contacts of H2B with H4 were maintained for a long time during the H2A–H2B displacement process, indicating their importance. In humans, Glu76Lys in H2B α 2 [4] [5] [6] [7] and Arg99Cys in H2B α 3 [5], corresponding to Glu73 and Arg96, respectively in this study, have been found in cancer-associated histone mutations. Glu76Lys disrupts histone octamer formation and nucleosome structure [4]. Mutations at Asp68 in H4 α 2 and Arg92 in H4 α 3 have also frequently been found in cancer-associated histone mutation [4] [5] [6].

These residues are well correlated with those that maintain the H2B – H4 contact during H2A–H2B displacement up to $d = \sim 52$ Å. Mutations in such residues can perturb this interaction and affect the free-energy component for the interaction at ~ 13 kcal/mol.

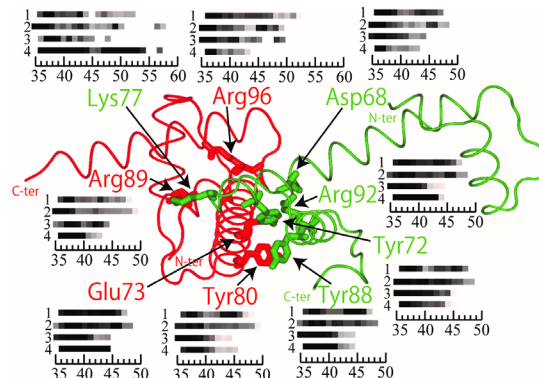


Fig. 3(e) Important residues at the H2A–H2B – H3–H4 interface.

Summary

The residues shown in Fig. 3 correspond well with the mutated sites found in cancer cells, suggesting that the loss of nucleosome stability is strongly associated with dysfunction of gene regulation.

Acknowledgements

This work was supported by the Ministry of Education, Culture, Sports, Science and Technology (MEXT) of Japan, part of the “Program for Promoting Researches on the Supercomputer Fugaku” (Biomolecular dynamics in a living cell) (hp210177), the HPCI system provided by the Kyoto University (Project ID: hp210060), and JSPS KAKENHI (JP18K06173 to H. Ishida and JP18H05534 to H. Kono)

References

1. H. Ishida and H. Kono, *J. Mol. Biol.* (2022) 434:167707
2. R. Singh, et al. *Nucleic Acid Res.* (2018) 46:8665
3. S. Bhattacharya, et al. *Epigenetics Chromatin.* (2017) 10:48
4. R. Bennett, et al. *Cancer Discov.* (2019) 9:1438
5. BA. Nacev, et al. *Nature* (2019) 567:473
6. S. Amatori, et al. *Clin. Epigenetics.* (2021) 13:71
7. Y. Arimura, et al. *Nucleic Acids Res.* (2018) 46:10007

Single-molecule evaluation of radiation-induced clustered DNA damage and its repair with atomic force microscopy

NAKANO Toshiaki

DNA Damage Chemistry Team, Institute for Quantum Life Science



1. Abstract

Radiation-induced multiple locally damaged sites in DNA (clustered DNA damage) are thought to be closely related to the biological effects of radiation. A method has been established to evaluate the complexity of clustered DNA damage in genomic DNA extracted from TK6 cells irradiated with low-dose ionizing radiation using atomic force microscopy (AFM). This was realized by isolating and concentrating the DNA molecules with lesions from all the irradiated DNA molecules (including intact ones). This study aims to estimate the level of damage clustering, *in-vivo*. We found that ionizing radiation causes clustered DNA damage in TK6 cells, whereas Fenton's reagents do not induce this damage, highlighting the importance of clustered DNA damage as a signature of ionizing radiation. We further observed that Fe-ion beams (high-LET radiation) produce various types of clustered DNA damage with higher complexity, consisting of more than two lesions, which are quite few in the case of X-rays. Surprisingly, analyses of DNA damage repair revealed that non-double-strand-break (non-DSB) clustered DNA damage was repaired efficiently in TK6 cells after irradiation with either X-rays or Fe-ion beams. The repair efficiency of complex DSBs, which are frequently produced after Fe-ion beam irradiation, is low.

2. Introduction

Radiation causes not only DNA scissions but also various types of oxidative damage, the amount of which varies greatly depending on the type of radiation. These lesions in chromosomal DNA may lead to biological effects such as cell death, mutation, and ultimately, cancer. Types of induced DNA damage include base damage, abasic (AP) sites, single-strand breaks (SSB), double-strand breaks (DSB), and DNA-protein crosslinks (DPC). Endogenously generated DNA lesions, as well as oxidative DNA damage induced by Fenton reaction with hydrogen peroxide in cells, are chemically identical to the individual lesions induced by ionizing radiation. However, even when there is no significant difference in the type of damage or total amount of damage caused by radiation and hydrogen peroxide, the biological effects of these two treatments differ greatly. From these observations, it can be concluded that DNA damage clustering is the signature of ionizing radiation, whereas endogenous and chemical-agent-induced DNA damage is mainly isolated. Clustered DNA damage has been postulated to be mainly responsible for the detrimental effects of ionizing radiation because the repair of clustered DNA damage is compromised (1).

In-vitro studies using chemically synthesized DNA lesions have revealed that clustered DNA damage is often resistant to repair. The extent of repair is governed by the extent of separation between the lesions, type of lesions, and number of lesions within a cluster. Furthermore, the hierarchy of damage excision is

proposed to depend on the type of lesion. Compromised repair of lesions of a cluster is further supported by the findings *in-vivo*, where replication inhibition or mutation induction is readily observed depending on the configuration of lesions in a cluster.

In addition to the enzymatic conversion method described above, estimation of the localization of DNA damage has been attempted using fluorescence resonance energy transfer (FRET) between fluorescent dyes that are labeled to AP sites (2). Although this method clearly demonstrates the overall average extent of damage clustering, it does not reveal the complexity of clustered DNA damage. Previously, we developed a method to observe radiation-induced clustered DNA damage in plasmid DNA *in-vitro*. By labeling DNA damage sites with biotin and subsequently with avidin, we directly visualized DNA damage using atomic force microscopy (AFM). We found that a higher fraction of clustered DNA damage was generated upon increasing the LET and that DSB accompanying the base damage/AP site at the DNA ends was produced. A great amount of information on the yield and especially, complexity of clustered DNA damage was obtained using this novel AFM technique (3). The proportion of various types of X-ray-induced clustered DNA damage demonstrated by AFM was further compared with that calculated by simulation, and they showed good agreement (4). However, it has not been possible to study the complexity of cellular DNA damage. In this study, we aim to use AFM to measure the DNA damage caused by DNA within cells.

3. Methods

Visualization of DNA damage in chromosomal DNA of TK6 cells by AFM

The amount of DNA damage produced in cells is expected to be considerably low when the same dose is applied *in-vitro*, as we irradiate the plasmids under low scavenging conditions relative to those of the cells in our previous study. It has been reported that the yield of DNA damage in $1 \times TE$ is approximately 1/20 of that in cells. Therefore, to visualize clustered DNA damage in genomic DNA by AFM, selective enrichment of the damaged DNA is necessary. In this study, to enrich the damaged DNA, we explore the possibility of labeling damaged DNA with biotin and then pulling it down with avidin-coated magnetic beads, as avidin is known to have an extremely high affinity for biotin. However, as the size of the avidin-coated magnetic beads is widely distributed, additional steps to replace the magnetic beads with streptavidin monomers are required to directly visualize the level of damage clustering of the enriched damaged DNA, through AFM. We first prepared biotin-labeled oligonucleotides as a model of damaged DNA bound by ARP-biotin and attempted to recover the DNA using reversibly elutable streptavidin monomer-immobilized magnetic beads. Biotin-labeled double-stranded DNA was highly enriched under our experimental conditions. Next, we tried to release the magnetic

beads from the biotin-labeled DNA. After heat treatment at 90 °C for 2 min, the magnetic beads were released from the recovered biotin-labeled DNA, but streptavidin was not. After heat treatment at 95 °C for 5 min, streptavidin was successfully released, but the DNA was denatured. Proteinase K treatment was required to completely remove streptavidin from biotin-labeled DNA without any denaturation of DNA. The recovery rates of the DNA damaged by the beads were approximately 30%. Under our experimental conditions, the base damage and clustered DNA damage that occurred in the chromosomal DNA of TK6 cells were observed by AFM. The analysis of clustered DNA damage using a DNA-containing model clustered damage revealed that two biotin–streptavidin tags at the defined damage sites with a separation of 3bp could be clearly distinguished (5).

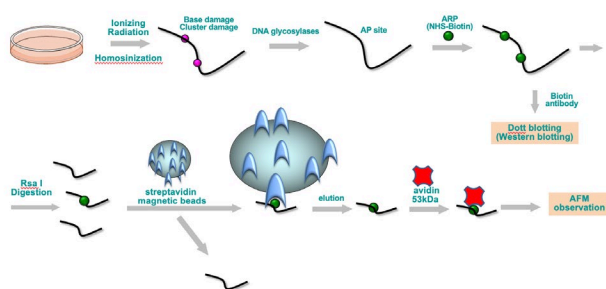


Fig. 1 Outline of DNA damage analysis

4. Results and discussions

Damage caused by hydrogen peroxide, X-rays, Fe-ion beams

AFM analysis revealed that the enriched damaged DNA contained isolated base damage, two-lesion clusters, complex DSB (DSB+ base damage), and complex clusters. As the damage enrichment step did not recover all the damaged DNA fragments, we took an approach to first determine the fraction of each type of damage, and then the number of base damages contained in each damage type, to obtain an accurate yield of each type of damage. Knowing these two values enabled us to calculate the yield of each type of damage from the total base damage yield quantified by slot blotting. In the case of Fenton's reaction, the fraction of isolated base damage was 90%, and the fraction of complex DSB was approximately 8%. These DNA damage fractions did not significantly change with varying concentrations of H₂O₂ from 0.25 to 1 mM. We do not know why complex DSB were found in a relatively high fraction after H₂O₂ treatment. The yields of isolated damage and complex DSB were estimated to be 1.2 and 15.2 per 10⁶ bp per 0.5 mM of H₂O₂, respectively. Regarding the irradiation of ionizing radiation, the overlap of radiation tracks in the dose range used in this study was negligible, and the damage was very likely induced by a single radiation track. Indeed, the fraction of clustered DNA damage, which included complex DSB and two-lesion clusters, did not seem to be strongly dose-dependent. In the chromosomal DNA from X-ray irradiated TK6 cells, in addition to isolated base damage and complex DSB, two-lesion clusters were observed. The average fractions of isolated damage, two-lesion clusters, and complex DSB were 83.5, 12.2, and 5.3%, respectively, after X-ray irradiation. In the case of Fe-ion beams, the types of DNA damage generated were isolated base damage (60.3%), two-lesion

clusters (20.2%), complex clusters (4.8%), and complex DSB (5.3%). The ratio of isolated damage to clustered damage was 11.0:1.0 for X-rays and 2.1:1.0 for Fe-ion beams. Our analysis demonstrated that Fe-ion beams produced clustered DNA damage more preferentially than X-rays did. Densely ionizing Fe-ion beams produced more clustered DNA damage than sparsely ionizing X-rays (5).

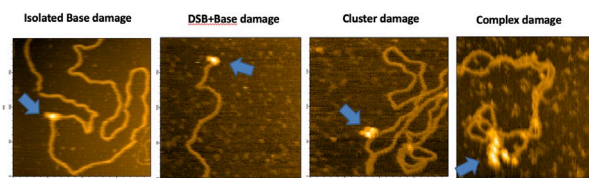


Fig. 2 AFM imaging of DNA damage in TK6 cells irradiated with Fe-ion beams.

Repair of DNA damage caused by X-rays and Fe-ion beams

Next, we examined the repair efficiency of each type of damage induced by ionizing radiation. Irradiated cells were incubated for up to 18 h, and the fraction of each type of damage and the amount of damage were monitored. The amount of each damage was calculated by multiplying the fraction with the total amount of base damage determined from the slot blot experiments. After irradiation with 40 Gy of X-rays, the fraction of clustered DNA damage slightly decreased with increasing incubation time. At 1 h after irradiation, approximately half of the isolated base damage was repaired, and the resultant damage further decreased to 20% or less at 6 h. Surprisingly, the two-lesion clusters and the complex DSB were repaired at a rate similar to that of isolated base damage. Approximately 60% of the induced complex DSB were repaired by 6 h, and 90% of the total DSB were repaired slowly by 18 h. Total DSB were repaired at a rate similar to that of complex DSB. After 18 h of incubation, the amount of isolated base damage was almost the same as that of the unirradiated control, although some complex clusters remained. In the case of Fe-ion beams at 40 Gy, similar to X-rays, the isolated damage along with the two-lesion clusters were repaired efficiently. One hour after irradiation, 50% of these types of damages were repaired, and the unrepaired fraction decreased to 20% or less at 6 h. However, a small number of two-lesion and complex clusters remained even after 18 h of incubation. Interestingly, the number of complex DSBs increased slightly after 1 h. The total DSB was repaired more slowly than in the case of X-rays, and even after 18 h of incubation, approximately 40% of the total and complex DSB terminals remained unrepaired (5).

Acknowledgments

We wish to thank Dr. K. Akamatsu and Dr. N. Shikazono (QST) for their helpful discussions.

References

- [1] T. Nakano *et al.*, *Free Radic. Biol. Med.*, **107**, 136-145 (2017).
- [2] K. Akamatsu *et al.*, *Anal. Biochem.*, **536**, 78-89 (2017).
- [3] X. Xu *et al.*, *Nucleic Acids Res.*, **48**(3), e18 (2020).
- [4] Y. Matsuya *et al.*, *Int. J. Mol. Sci.*, **21**(5), 1701 (2020).
- [5] T. Nakano *et al.*, *PNAS*, **119**, e2119132119 (2022).

Publication Lists

Original Papers

1. Study on FeCr thin film for a spintronic material with negative spin polarization.

Hirofumi Suto, Tomoya Nakatani, Yohei Kota, Asam Nagarjuna, Hitoshi Iwasaki, Kenta Amemiya, Takaya Mitsui, Seiji Sakai, Songtian Li, Yohei Kota, Yuya Sakuraba, Journal of Magnetism and Magnetic Materials, 557, 169474-1 - 169474-9, 2022, DOI:10.1016/j.jmmm.2022.169474

2. Multi-channel dissociative ionization of ethanol in intense ultraviolet laser fields: Energy correlation between photoelectron emission and fragment recoil.

Ikuta Tomoya, Hosaka Kouichi, Akagi Hiroshi, Kannari Fumihiko, Itakura Ryuji, Physical Review A, 106(2), 023106-1 - 023106-9, 2022, DOI:10.1103/PhysRevA.106.023106

3. Dispersive XAFS Study on the Laser-Induced Reduction of a Rh³⁺ Ion Complex: Presence of a Rh⁺ Intermediate in Direct Photoreduction.

Morihisa Saeki, Daiju Matsumura, Ryuzo Nakanishi, Takumi Yomogida, Takuya Tsuji, Hiroyuki Saitoh, Hironori Oba, Journal of Physical Chemistry C, 126, 5607 - 5616, 2022, DOI:10.1021/acs.jpcc.1c10160

4. AnaBHEL (Analog Black Hole Evaporation via Lasers) Experiment: Concept, Design, and Status.

Pisin Chen, Gerard Mourou, Marc Besancon, Yuji Fukuda, Jean-Francois Glicenstein, Jiwoo Nam, Ching-En Lin, Kuan-Nan Lin, Shu-Xiao Liu, Yung-Kun Liu, Masaki Kando, Kotaro Kondo, Stathes Paganis, Alexander Pirozhkov, Hideaki Takabe, Boris Tuchming, Wei-Po Wang, Naoki Watamura, Jonathan Wheeler, Hsin-Yeh Wu, Photonics, 9, 1003, 2022, DOI:https://doi.org/10.3390/

5. Spectral-temporal Measurement Capabilities of Third-order Correlators.

S. Bock, T. Oksenhendler, T. Püschel, R. Gebhardt, U. Helbig, R. Pausch, T. Ziegler, C. Bernert, K. Zeil, A. Irman, T. Toncian, H. Kiriya, M. Nishiuchi, A. Kon, U. Schramm, Optics Express, 31(6), 9923 - 9934, 2023

6. ハイパワーレーザーの基礎.

桐山 博光, 日本加速器学会誌, 19(4), 177 - 186, 2023

7. 超高強度レーザーによる量子ビーム科学.

桐山 博光, 宮坂 泰弘, 眞柴 雄司, 中新 信彦, 近藤 康太郎, 今 亮, 福田 祐仁, 西内 満美子, ピロジコフアレキサンダー, 匂坂 明人, 小倉 浩一, 神門 正城, フォトニクスニュース, 8(2), 4 - 9, 2023

8. J-KAREN-P ベタワットレーザーシステムとその利用研究のリモート化と自動化への取り組み.

桐山 博光, 桐山, 眞柴 雄司, 眞柴, 宮坂 泰弘, 宮坂, 中新 信彦, 中新, 近藤 康太郎, 近藤, 今 亮, 福田 祐仁, 西内 満美子, レーザー研究, 50(12), 678 - 682, 2022

9. Measurement Method for Laser-Accelerated Multi-hundred-MeV Protons Utilizing Multiple Coulomb Scattering in an Emulsion Cloud Chamber.

Takafumi Asai, Chihiro Inoue, Satoshi Jinno, Nobuko Kitagawa, Satoshi Kodaira, Kunihiro Morishima, Yuji Fukuda, Tomoya Yamauchi, Masato Kanasaki, Japanese Journal of Applied Physics, 62(016506), 1 - 6, 2023

10. 原子核乾板を利用した高エネルギーレーザー加速陽子線計測手法の 230MeV 加速器陽子線に対する実証実験.

浅井 孝文, 井上 千裕, 神野 智史, 北川 暢子, 小平 聡, 森島 邦博, 福田 祐仁, 山内 知也, 金崎 真聡, ESI-NEWS, 40(5), 1 - 8, 2022

11. 多段シンチレータを用いた多核種 GeV イオン計測器の開発—レーザーイオン加速実験における活用とその展望—.

南 卓海, 時安 敦史, 郡 英輝, 安部 勇輝, 岩崎 滉, 田口 智也, 小田 和昌, 鈴木 蒼一郎, 浅井 孝文, 境 健太郎, 姫野 公輔, 田中 周太, 諫山 翔伍, 金崎 真聡, 小平 聡, 福田 祐仁, 蔵満 康浩, ESI-NEWS, 40(4), 1 - 9, 2022

12. Mass-resolved ion measurement by particle counting analysis for characterizing relativistic ion beams driven by lasers.

Minami Takumi, Tokiyasu Atsushi, Kohri Hideki, Abe Yuki, Iwasaki Kou, Taguchi Tomoya, Oda Kazumasa, Suzuki Soichiro, Asai Takafumi, Tanaka Shuta, Isayama Shogo, Kanasaki Masato, Kodaira Satoshi, Fukuda Yuji, Kuramitsu Yasuhiro, Review of Scientific Instruments, 93(11), 3530-1 - 3530-5, 2022, DOI:10.1063/5.0101872

13. Laser-driven multi-MeV high-purity proton acceleration via anisotropic ambipolar expansion of micron-scale hydrogen clusters.

Satoshi Jinno, Masato Kanasaki, Takafumi Asai, Ryutaro Matsui, Alexander Pirozhkov, Ogura Koichi, Sagisaka Akito, Miyasaka Yasuhiro, Nakanii Nobuhiko, Kando Masaki, Nobuo Kitagawa, Kunihiro Morishima, Saroshi Kodaira, Yasuaki Kishimoto, Tomoya Yamauchi, Mitsuru Uesaka, Hiromitsu Kiriyama, Yuji Fukuda, *Scientific Reports*, 12, 16753-1 - 16753-9, 2022, DOI:10.1038/s41598-022-18710-x

14. A multi-stage scintillation counter for GeV-scale multi-species ion spectroscopy in laser-driven particle acceleration experiments.

Y. Abe, H. Kohri, A. Tokiyasu, T. Minami, K. Iwasaki, T. Taguchi, T. Asai, M. Kanasaki, S. Kodaira, S. Fujioka, Y. Kuramitsu, Y. Fukuda, *Review of Scientific Instruments*, 93, 063502-1 - 063502-8, 2022, DOI:10.1063/5.0078817

15. Controllable electron self-injection in laser wakefield acceleration with asymmetric gas-jet nozzle.

Zhenzhe Lei, Zhan Jin, Alexei Zhidkov, Naveen Pathak, Yoshio Mizuta, Kai Huang, Nakanii Nobuhiko, Daito Izuru, Kando Masaki, Tomonao Hosokai, *Progress of Theoretical and Experimental Physics*, 2023(3), 033J01-1 - 033J01-13, 2023, DOI:10.1093/ptep/ptad030

16. Precise pointing control of high-energy electron beam from laser wakefield acceleration using an aperture.

Nobuhiko Nakanii, Kai Huang, Kotaro Kondo, Hiromitsu Kiriyama, Masaki Kando, *Applied Physics Express*, 16, 026001-1 - 026001-5, 2023, DOI:10.35848/1882-0786/acb892

17. Enhanced diagnostics of radiating relativistic singularities and BISER by nonlinear post-compression of optical probe pulse.

A.V.Kotov, T.Zh. Esirkepov, A.A.Soloviev, A. Sagisaka, K. Ogura, A. Bierwage, M. Kando, H. Kiriyama, M.V.Starodubtsev, E.A.Khazanov, S.Yu.Mironov, A.S. Pirozhkov, *Journal of Instrumentation*, 17(7), P07035, 2022, DOI:10.1088/1748-0221/17/07/P07035

18. Enhanced ion acceleration from transparency-driven foils demonstrated at two ultraintense laser facilities.

Nicholas P. Dover, Tim Ziegler, Stefan Assenbaum, Constantin Bernert, Stefan Bock, Florian-Emanuel Brack, Thomas E. Cowan, Emma J. Ditter, Marco Garten, Lennart Gaus, Ilja Goethel, George S. Hicks, Hiromitsu Kiriyama, Thomas Kluge, James K. Koga, Akira Kon, Kotaro Kondo, Stephan Kraft, Florian Kroll, Hazel F. Lowe, Josefine Metzkes-Ng, Tatsuhiko Miyatake, Zulfikar Najmudin, Thomas Püschel, Martin Rehwald, Marvin Reimold, Hironao Sakaki, Hans-Peter Schlenvoigt, Keiichiro Shiokawa, Marvin E. P. Umlandt, Ulrich Schramm, Karl Zeil, Mamiko Nishiuchi, *Light Science and Applications*, 12, 71, 2023, DOI:10.1038/s41377-023-01083-9

19. フェムト秒レーザー生成プラズマ駆動イオン源からのイオンビーム輸送.

榊 泰直, 宮武 立彦, *プラズマ・核融合学会誌*, 98(6), 267 - 271, 2022

20. Characteristics of laminar ion beams accelerated via a few-joule laser pulse.

Morita Toshimasa, *Physical Review Research*, 4(4), 043020, 2022, DOI:10.1103/PhysRevResearch.4.043020

21. Characterization of plasma mirror system at J-KAREN-P facility.

Akira Kon, Mamiko Nishiuchi, Yuji Fukuda, Kotaro Kondo, Koichi Ogura, Akito Sagisaka, Yasuhiro Miyasaka, Nicholas P. Dover, Masaki Kando, Alexander S. Pirozhkov, Izuru Daito, Liu Chang, Il Woo Choi, Chang Hee Nam, Tim Ziegler, Hans-Peter Schlenvoigt, Karl Zeil, Ulrich Schramm, Hiromitsu Kiriyama, *High Power Laser Science and Engineering*, 10, e25, 2022, DOI:10.1017/hpl.2022.15

22. Nanoscale subsurface dynamics of solids upon high-intensity femtosecond laser irradiation observed by grazing-incidence x-ray scattering.

L.Randolph, M.Banjafar, T.R.Preston, T.Yabuuchi, M.Makita, N.P.Dover, S.Göde, Y.Inubushi, G.Jakob, J.Kaa, A. Kon, J.K.Koga, D.Ksenzov, T.Matsuoka, M.Nishiuchi, M.Paulus, Ch.Rödel, F.Schon, K.Sueda, Y.Sentoku, T.Togashi, M.Vafae-Khanjani, M.Bussmann, T.E.Cowan, M.Kläui, C.Fortmann-Grote, A.P.Mancuso, T.Kluge, C.Gutt, M.Nakatsutsumi, *Physical Review Research*, 4(3), 33038, 2022, DOI:10.1103/PhysRevResearch.4.033038

23. Strange layer structure of dipolar spins formed on the spin-ice lattice.

- Yonetani Yoshiteru, *Chemical Physics Letters*, 817, 140406, 2023, DOI:10.1016/j.cplett.2023.140406
- 24. Exciton quantum dynamics in the molecular logic gates for quantum computing.**
Yonetani Yoshiteru, *Chemical Physics*, 570, 111860, 2023, DOI:10.1016/j.chemphys.2023.111860
- 25. Demonstration of a spherical plasma mirror for the counter-propagating kilojoule-class petawatt LFEX laser system.**
Sadaaki Kojima, Yuki Abe, Eisuke Miura, Tetsuo Ozaki, Kohei Yamanoi, Kohei Yamanoi, Yubo Wang, Jinyuan Dun, Shuwang Guo, Tamaki Maekawa, Ryunosuke Takizawa, Hiroki Morita, Shouji Asano, Yasunobu Arikawa, Hiroshi Sawada, Katsuhiko Ishii, Ryohei Hanayama, Shinichiro Okihara, Yoneyoshi Kitagawa, Yasuhiro Kajimura, Alessio Morace, Hiroyuki Shiraga, Keisuke Shigemori, Atsushi Sunahara, Natsumi Iwata, Takayoshi Sano, Yasuhiko Sentoku, Tomoyuki Johzaki, Masaharu Nishikino, Akifumi Iwamoto, Kenichi Nagaoka, Hitoshi Sakagami, Shinsuke Fujioka, Yoshitaka Mori, *Optics Express*, 30(24), 43491 - 43502, 2022, DOI:10.1364/OE.475945
- 26. Enhancement of gain coefficient of Li-like Ion 3d-4f soft x-ray laser oscillation by a single resonator.**
Namba Shinichi, Wang Jiahao, Hikari Ohiro, Jiawei Zhang, Kishimoto Maki, Kotaro Yamasaki, Hasegawa Noboru, Thanhhung Dinh, Ishino Masahiko, Takeshi Higashiguchi, Nishikino Masaharu, *Atoms*, 10(4), 128-1 - 128-6, 2022, DOI:10.3390/atoms10040128
- 27. Modeling the wavelength of unresolved transition arrays in the extreme ultraviolet region from Sn to Hf ions by combining theoretical and experimental spectral data.**
Sasaki Akira, Murakami Izumi, Sakaue Hiroyuki, Fujii Keisuke, Nishikawa Takeshi, Ohashi Hayato, Nakamura Nobuyuki, *AIP advances*, 12, 025309, 2022, DOI:10.1063/5.0077130
- 28. Beat-frequency-resolved two-dimensional electronic spectroscopy: disentangling vibrational coherences in artificial fluorescent proteins with sub-10-fs visible laser pulses.**
Tsubouchi Masaaki, Ishii Nobuhisa, Kagotani Yuji, Shimizu Rumi, Fujita Takatoshi, Adachi Motoyasu, Itakura Ryuji, *Optics Express*, 31(4), 6890 - 6906, 2023, DOI:10.1364/OE.480505
- 29. Mid-infrared pulse generation using multi-plate white-light generation and optical parametric amplification in LiGaS₂ crystals.**
Nakagawa Kotaro, Ishii Nobuhisa, Kanemitsu Yoshihiko, Hirori Hideki, *Applied Physics Express*, 16, 032001, 2023, DOI:10.35848/1882-0786/acbd83
- 30. Mid-infrared light-induced photoacoustic wave in water and its application.**
Tsubouchi Masaaki, Endo Tomoyuki, Itakura Ryuji, *Photoacoustics*, 16(1), 012007, 2023, DOI:10.35848/1882-0786/acabab
- 31. Propagation effects on high-harmonic generation from dielectric thin films.**
Yamada Shunsuke, Otobe Tomohito, David Freeman, Anatoli Kheifets, Kazuhiro Yabana, *Physical Review B*, 107(3), 035132, 2023, DOI:10.1103/PhysRevB.107.035132
- 32. High order harmonic generation in semiconductors driven at near- and mid-IR wavelengths.**
David Freeman, Yamada Shunsuke, Yamada Atsushi, Yabana Kazuhiro, Anatoli Kheifets, *Physical Review B*, 106, 075202, 2022, DOI:10.1103/PhysRevB.106.075202
- 33. Ultrashort near-infrared pulse generation by non-collinear optical parametric amplification in LiInS₂.**
Imasaka Kotaro, Ogawa Kanade, Ishii Nobuhisa, Maruyama Momoko, Itakura Ryuji, *Optics Continuum*, 1(9), 1956 - 1962, 2022, DOI:10.1364/OPTCON.467462
- 34. Wavelength dependence of laser-induced excitation dynamics in silicon.**
Prachi Venkat, Otobe Tomohito, *Applied Physics A*, 128, 810, 2022, DOI:10.1007/s00339-022-05928-9
- 35. Real-time observation of the Woodward-Hoffmann rule for 1,3-cyclohexadiene by femtosecond soft X-ray transient absorption.**
Sekikawa Taro, Saito Nariyuki, Kurimoto Yutaro, Ishii Nobuhisa, Mizuno Tomoya, Kanai Teruto, Itatani Jiro, Saita Kenichiro, Taketsugu Tetsuya, *Physical Chemistry Chemical Physics*, 25(12), 8497 - 8506, 2023, DOI:10.1039/d2cp05268g

36. 100-mJ class, sub-two-cycle, carrier-envelope phase-stable dual-chirped optical parametric amplification.

Xu Lu, Xue Bing, Ishii Nobuhisa, Itatani Jiro, Midorikawa Katsumi, Eiji J. Takahashi, Optics Letters, 47(13), 3371 - 3374, 2022, DOI:10.1364/OL.455811

37. Intense infrared lasers for strong-field science.

Chang Zenghu, Fang Li, Fedorov Vladimir, Geiger Chase, Ghimire Shambhu, Heide Christian, Ishii Nobuhisa, Itatani Jiro, Joshi Chandrashekhar, Kobayashi Yuki, Kumar Prabhat, Marra Alphonse, Mirov Sergey, Petrushina Irina, Polyanskiy Mikhail, Reis David, Tochitsky Sergei, Vasilyev Sergey, Wang Lifeng, Wu Yi, Zhou Fangjie, Advances in Optics and Photonics, 14(4), 652 - 782, 2022, DOI:10.1364/AOP.454797

38. パルス内差周波発生法と光パラメトリック増幅による位相安定高強度マルチテラヘルツパルス発生.

神田 夏輝, 石井順久, 板谷 治郎, 松永 隆佑, レーザー研究, 50(6), 286 - 290, 2022

39. Mass Resolved Momentum Imaging of Three Dichloroethylene Isomers by Femtosecond Laser Induced Coulomb Explosion.

Yoriko Wada, Hiroshi Akagi, Takayuki Kumada, Ryuji Itakura, Tomonari Wakabayashi, Photochem, 2(3), 798 - 809, 2022, DOI:10.3390/photochem2030051

40. Development and clinical verification of a small intestine motility measurement system using an ileus tube.

Shinji Hosokawa, Akihiro Naganawa, Takeshi Seki, Kiyoshi Oka, Noriaki Manabe, Ken Haruma, Junji Yoshino, Advanced Biomedical Engineering, 11, 228 - 236, 2022, DOI:10.14326/abe.11.228

41. Search for the Majorana Nature of Neutrinos in the Inverted Mass Ordering Region with KamLAND-Zen.

S.Abe, S.Asami, M.Eizuka, S.Futagi, A.Gando, Y.Gando, T.Gima, A.Goto, T.Hachiya, K.Hata, S.Hayashida, K.Hosokawa, K.Ichimura, S.Ieki, H.Ikeda, K.Inoue, K.Ishidoshiro, Y.Kamei, N.Kawada, Y.Kishimoto, M.Koga, M.Kurasawa, N.Maemura, T.Mitsui, H.Miyake, T.Nakahata, K.Nakamura, K.Nakamura, R.Nakamura, H.Ozaki, T.Sakai, H.Sambonsugi, I.Shimizu, J.Shirai, K.Shiraishi, A.Suzuki, Y.Suzuki, A.Takeuchi, K.Tamae, K.Ueshima, H.Watanabe, Y.Yoshida, S.Obara, A.K.Ichikawa, D.Chernyak, A.Kozlov, K.Z.Nakamura, S.Yoshida, Y.Takemoto, S.Umehara, K.Fushimi, K.Kotera, Y.Urano, B.E.Berger, B.K.Fujikawa, J.G.Learned, J.Maricic, S.N.Axani, J.Smolsky, Z.Fu, L.A.Winslow, Y.Efremenko, H.J.Karwowski, D.M.Markoff, W.Tornow, S.Dell'Oro, T.O'Donnell, J.A.Detwiler, S.Enomoto, M.P.Decowski, C.Grant, A.Li, H.Song, Physical Review Letters, 130(5), 051801-1 - 051801-7, 2023, DOI:10.1103/PhysRevLett.130.051801

42. KamLAND's search for correlated low-energy electron antineutrinos with astrophysical neutrinos from IceCube.

S.Abe, S.Asami, M.Eizuka, S.Futagi, A.Gando, Y.Gando, T.Gima, A.Goto, T.Hachiya, K.Hata, K.Hosokawa, K.Ichimura, S.Ieki, H.Ikeda, K.Inoue, K.Ishidoshiro, Y.Kamei, N.Kawada, Y.Kishimoto, T.Kinoshita, M.Koga, M.Kurasawa, N.Maemura, T.Mitsui, H.Miyake, T.Nakahata, K.Nakamura, R.Nakamura, H.Ozaki, T.Sakai, H.Sambonsugi, I.Shimizu, J.Shirai, K.Shiraishi, A.Suzuki, Y.Suzuki, A.Takeuchi, K.Tamae, H.Watanabe, Y.Yoshida, Obara Shuhei, A.K.Ichikawa, S.Yoshida, S.Umehara, K.Fushimi, K.Kotera, Y.Urano, B.E.Berger, B.K.Fujikawa, J.G.Learned, J.Maricic, S.N.Axani, J.Smolsky, J.Lertprasertpong, L.A.Winslow, Z.Fu, J.Oullet, Y.Efremenko, H.J.Karwowski, D.M.Markoff, W.Tornow, A.Li, J.A.Detwiler, S.Enomoto, M.P.Decowski, C.Grant, H.Song, T.O'Donnell, S.Dell'Oro, Astroparticle Physics, 143, 102758, 2022, DOI:10.1016/j.astropartphys.2022.102758

43. Abundances of Uranium and Thorium Elements in Earth Estimated by Geoneutrino Spectroscopy.

S. Abe, S. Asami, M. Eizuka, S. Futagi, A. Gando, Y. Gando, T. Gima, A. Goto, T. Hachiya, K. Hata, K. Hosokawa, K. Ichimura, S. Ieki, H. Ikeda, K. Inoue, K. Ishidoshiro, Y. Kamei, N. Kawada, Y. Kishimoto, M. Koga, M. Kurasawa, N. Maemura, T. Mitsui, H. Miyake, T. Nakahata, K. Nakamura, K. Nakamura, R. Nakamura, H. Ozaki, T. Sakai, H. Sambonsugi, I. Shimizu, Y. Shirahata, J. Shirai, K. Shiraishi, A. Suzuki, Y. Suzuki, A. Takeuchi, K. Tamae, H. Watanabe, Y. Yoshida, O. Shuhei, A. K. Ichikawa, S. Yoshida, S. Umehara, K. Fushimi, K. Kotera, Y. Urano, B. E. Berger, B. K. Fujikawa, J. G. Learned, J. Maricic, S. N. Axani, Z. Fu, J. Smolsky, L. A. Winslow, Y. Efremenko, H. J. Karwowski, D. M. Markoff, W.

Tornow, A. Li, J. A. Detwiler, S. Enomoto, M. P. Decowski, C. Grant, H. Song, T. O'Donnell, S. Dell'Oro, *Geophysical Research Letters*, 49(16), e2022GL099566, 2022, DOI:10.1029/2022GL099566

44. Search for supernova neutrinos and constraint on the galactic star formation rate with the KamLAND data.

S. Abe, S. Asami, M. Eizuka, S. Futagi, A. Gando, Y. Gando, T. Gima, A. Goto, T. Hachiya, K. Hata, K. Hosokawa, K. Ichimura, S. Ieki, H. Ikeda, K. Inoue, K. Ishidoshiro, Y. Kamei, N. Kawada, Y. Kishimoto, M. Koga, M. Kurasawa, N. Maemura, T. Mitsui, H. Miyake, T. Nakahata, K. Nakamura, K. Nakamura, R. Nakamura, H. Ozaki, T. Sakai, H. Sambonsugi, I. Shimizu, J. Shirai, K. Shiraishi, A. Suzuki, Y. Suzuki, A. Takeuchi, K. Tamae, H. Watanabe, Y. Yoshida, S. Obara, A. Ichikawa, S. Yoshida, S. Umehara, K. Fushimi, K. Kotera, Y. Urano, B. E. Berger, B. K. Fujikawa, J. G. Learned, J. Maricic, S. N. Axani, L. A. Winslow, Z. Fu, J. Smolsky, Y. Efremenko, H. J. Karwowski, D. M. Markoff, W. Tornow, A. Li, J. A. Detwiler, S. Enomoto, M. P. Decowski, C. Grant, H. Song, T. O'Donnell, S. Dell'Oro, *The Astrophysical Journal*, 934(1), 85, 2022, DOI:10.3847/1538-4357/ac7a3f

45. Temperature dependence of Yb valence in an Au-Al-Yb intermediate-valence quasicrystal investigated by Yb L_3 -edge X-ray absorption near-edge structure spectroscopy.

Tetsu Watanuki, Masaichiro Mizumaki, Shinji Watanabe, Naomi Kawamura, Kiyofumi Nitta, Akihiko Machida, Tsutomu Ishimasa, *Materials Transactions*, 63(10), 1380 - 1383, 2022, DOI:10.2320/matertrans.MT-M2022064

46. Spin-orbital liquid state and liquid-gas metamagnetic transition on a pyrochlore lattice.

Nan Tang, Yulia Gritsenko, Kenta Kimura, Subhro Bhattacharjee, Akito Sakai, Mingxuan Fu, Hikaru Takeda, Huiyuan Man, Kento Sugawara, Yosuke Matsumoto, Yasuyuki Shimura, Jiajia Wen, Collin Broholm, Hiroshi Sawa, Masashi Takigawa, Toshiro Sakakibara, Sergei Zherlitsyn, Joachim Wosnitza, Roderich Moessner, Satoru Nakatsuji, *Nature Physics*, 19, 92-98, 2022, DOI:10.1038/s41567-022-01816-4

47. X-ray Two-beam Topography for Quantitative Derivation of Phase Shift by Crystalline Dislocations.

Yoshiki Kohmura, Kenji Ohwada, Nobuki Kakiuchi, Kei Sawada, Tadaaki Kaneko, Mizuki Junichiro, Masaichiro Mizumaki, Watanuki Tetsu, Tetsuya Ishikawa, *Physical Review Research*, 5, L012043, 2023, DOI:10.1103/PhysRevResearch.5.L012043

48. Polar-Nonpolar Transition-Type Negative Thermal Expansion with 11.1% Volume Shrinkage by Design.

Takumi Nishikubo, Takashi Imai, Yuki Sakai, Masaichiro Mizumaki, Shogo Kawaguchi, Norihiro Oshime, Ayumu Shimada, Kento Sugawara, Kenji Ohwada, Akihiko Machida, Tetsu Watanuki, Kosuke Kurushima, Shigeo Mori, Takashi Mizokawa, Masaki Azuma, *Chemistry of Materials*, 35(3), 870 - 878, 2023, DOI:10.1021/acs.chemmater.2c02304

49. Disentangling sequential and concerted fragmentations of molecular polycations with covariant native frame analysis.

J McManus, T Walmsley, K Nagaya, James Harries, Y Kumagai, H Iwayama, M Ashfold, M Britton, P Bucksbaum, B Downes-Ward, T Driver, D Heathcote, P Hockett, A Howard, E Kukk, J Lee, Y Liu, D Milesevic, R Minns, A Niozu, J Niskanen, A Orr-Ewing, S Owada, D Rolles, P Robertson, A Rudenko, K Ueda, J Unwin, C Vallance, M Burt, *Physical Chemistry Chemical Physics*, 24(37), 22699 - 22709, 2022, DOI:10.1039/D2CP03029B

50. The ferroelectric phase transition in a 500-nm-sized single particle of BaTiO₃ tracked by coherent X-ray diffraction.

Norihiro Oshime, Kenji Ohwada, Akihiko Machida, Nagise Fukushima, Shintaro Ueno, Ichiro Fujii, Satoshi Wada, Kento Sugawara, Ayumu Shimada, Tetsuro Ueno, Tetsu Watanuki, Kenji Ishii, Hidenori Toyokawa, Koichi Momma, Sangwook Kim, Shinya Tsukada, Yoshihiro Kuroiwa, *Japanese Journal of Applied Physics (Special Issues: Ferroelectric Materials and Their Applications)*, 61(SN), 1008, 2022, DOI:10.35848/1347-4065/ac7d94

51. 放射光単色 X 線を用いたアルミニウム単結晶の再結晶その場観察.

城 鮎美, 菖蒲 敬久, 岡田 達也, *材料*, 71(4), 354 - 360, 2022, DOI:10.2472/jsms.71.354

52. 高エネルギー放射光単色 X 線による二重露光応力測定.

鈴木 賢治, 山田 みなみ, 城 鮎美, 菅蒲 敬久, 豊川 秀訓, 佐治 超爾, 材料, 71(4), 347 - 353, 2022, DOI:10.2472/jsms.71.347

53. Hydrogen absorption reactions of a hydrogen storage alloy La-Ni₅ under high pressure.

Toyoto Sato, Hiroyuki Saitoh, Reina Utsumi, Yuki Nakahira, Obana Kazuki, Shigeyuki Takagi, Shin-ichi Orimo, *Molecules*, 28(3), 1256, 2023, DOI:10.3390/molecules28031256

54. In-operando Measurement of Internal Temperature and Stress in Lithium-ion Batteries.

Tatsumi Hirano, Takehiro Maeda, Tetsuyuki Murata, Takahiro Yamaki, Eiichiro Matsubara, Takahisa Shobu, Ayumi Shiro, Ryo Yasuda, Daiko Takamatsu, *SPring-8 / SACLA 利用研究成果集*, 11(1), 49 - 57, 2023, DOI:10.18957/rr.11.1.49

55. Insight on the mechanical properties of hierarchical porous calcium-silicate-hydrate pastes according to the Ca/Si molar ratio using in-situ synchrotron X-ray scattering and nanoindentation test.

Sumin Im, Hyeonseok Jee, Heongwon Suh, Manabu Kanematsu, Satoshi Morooka, Hongbok Choe, Nishio Yuhei, Akihiko Machida, Jihoon Kim, Seungmin Lim, Sungchul Bae, *Construction and Building Materials*, 365, 130034, 2022, DOI:10.1016/j.conbuildmat.2022.130034

56. Heat-induced structural changes in magnesium alloys AZ₉₁ and AZ₃₁ investigated by in situ synchrotron high-energy X-ray diffraction.

Xiaojing Liu, Pingguang Xu, Ayumi Shiro, Shuoyuan Zhang, Takahisa Shobu, Eitaro Yukutake, Koichi Akita, Emil Zolotoyabko, Klaus-Dieter Liss, *Journal of Materials Science*, 57, 21446 - 21459, 2022, DOI:10.1007/s10853-022-07917-y

57. Improving electrochemical activity of P2-type Na_{2/3}Mn_{2/3}Ni_{1/3}O₂ by controlling its crystallinity.

Riki Kataoka, Noboru Taguchi, Kohei Tada, Akihiko Machida, Nobuhiko Takeichi, *Batteries & Supercaps*, 6(2), e202200462, 2023, DOI:10.1002/batt.202200462

58. Phase transformations and microstructure evolutions during depressurization of hydrogenated Fe-Mn-Si-Cr alloy.

Rama Srinivas Varanasi, Motomichi Koyama, Hiroyuki Saitoh, Reina Utsumi, Toyoto Sato, Shin-ichi Orimo, Eiji Akiyama, *International Journal of Hydrogen Energy*, 48, 10081 - 10088, 2022, DOI:10.1016/j.ijhydene.2022.11.274

59. Estimation of Grüneisen Parameter of Layered Superconductor LaO_{0.5}F_{0.5}BiS_{2-x}Se_x (x = 0.2, 0.4, 0.6, 0.8, 1.0).

Fysol Inba Abbas, Kazuhisa Hoshi, Nakahira Yuki, Miku Yoshida, Aichi Yamashita, Hiroaki Ito, Akira Miura, Chikako Moriyoshi, Chul-Ho Lee, Yoshikazu Mizuguchi, *Journal of the Physical Society of Japan*, 92, 014703-1 - 014703-7, 2023, DOI:10.7566/JPSJ.92.014703

60. Pressure cells for in situ neutron total scattering: Time and real-space resolution during deuterium absorption.

Kazutaka Ikeda, Hidetoshi Ohshita, Toshiya Otomo, Kouji Sakaki, Hyunjeong Kim, Yumiko Nakamura, Akihiko Machida, Robert B. Von Dreele, *Journal of Applied Crystallography*, 55(6), 1631 - 1639, 2022, DOI:10.1107/S1600576722010561

61. Hydrogen vibration excitations of ZrH_{1.8} and TiH_{1.84} up to 21 GPa by incoherent inelastic neutron scattering.

Takanori Hattori, Mitsutaka Nakamura, Kazuki Iida, Akihiko Machida, Asami Sano-Furukawa, Shin-ichi Machida, Hiroshi Arima, Hidetoshi Ohshita, Takashi Honda, Kazutaka Ikeda, Toshiya Otomo, *Physical Review B*, 106, 134309, 2022, DOI:10.1103/PhysRevB.106.134309

62. Glassy atomic vibrations and blurry electronic structures created by local structural disorders in high-entropy metal telluride superconductors.

Yoshikazu Mizuguchi, Hidetomo Usui, Rei Kurita, Kyohei Takae, Md. Riad Kasem, Ryo Matsumoto, Kazuki Yamane, Yoshihiko Takano, Yuki Nakahira, Aichi Yamashita, Yosuke Goto, Akira Miura, Chikako Moriyoshi, *Materials Today Physics*, 32, 101019, 2023, DOI:10.1016/j.mtphys.2023.101019

63. Rotation of Complex Ions with Ninefold Hydrogen Coordination Studied by Quasielastic Neutron Scattering and First-Principles Molecular Dynamics Calculations.

Yoshinori Ohmasa, Shigeyuki Takagi, Kento Toshima, Kaito Yokoyama, Wataru Endo, Shin-ichi Orimo, Hiroyuki Saitoh, Takeshi Yamada, Yukinobu Kawakita, Kazutaka Ikeda, Toshiya Otomo, Hiroshi Akiba, Osamu Yamamuro, *Physical Review Research*, 4(3), 033215, 2022, DOI:10.1103/PhysRevResearch.4.033215

64. Tuning of upper critical field in a vanadium-based A15 superconductor by the compositionally-complex-alloy concept.

Yuki Nakahira, Ryosuke Kiyama, Aichi Yamashita, Hiroaki Itou, Akira Miura, Chikako Moriyoshi, Yosuke Goto, Yoshikazu Mizuguchi, *Journal of Materials Science*, 57, 15990 - 15998, 2022, DOI:10.1007/s10853-022-07607-9

65. 回折法を利用した LPSO 型マグネシウム合金における階層的変形機構に関する研究.

城 鮎美, 菖蒲 敬久, 萩原 幸司, 渡邊 真史, *SPring-8/SACLA 利用研究成果集*, 10(5), 438 - 446, 2022, DOI:10.18957/rr.10.5.438

66. Effect of magnesium silicate hydrate (M-S-H) formation on the local atomic arrangements and mechanical properties of calcium silicate hydrate (C-S-H): In situ X-ray scattering study.

Gyeongryul Kim, Sumin Im, Hyeonseok Jee, Heongwon Suh, Seongmin Cho, Manabu Kanematsu, Satoshi Morooka, Taku Koyama, Yuhei Nishio, Akihiko Machida, Jihoon Kim, Sungchul Bae, *Cement and Concrete Research*, 159, 106869, 2022, DOI:10.1016/j.cemconres.2022.106869

67. Displacement of hydrogen position in di-hydride of V-Ti-Cr solid solution alloys.

Kouji Sakaki, Hyunjeong Kim, Eric Majzoub, Akihiko Machida, Tetsu Watanuki, Kazutaka Ikeda, Toshiya Otomo, Masataka Mizuno, Daiju Matsumura, Yumiko Nakamura, *Acta Materialia*, 234, 118055, 2022, DOI:10.1016/j.actamat.2022.118055

68. Repeatable Photoinduced Insulator-to-Metal Transition in Yttrium Oxyhydride Epitaxial Thin Films.

Yuya Komatsu, Ryota Shimizu, Ryuhei Sato, Markus Wilde, Kazunori Nishio, Takayoshi Katase, Daiju Matsumura, Hiroyuki Saitoh, Masahiro Miyauchi, Jonah R. Adelman, Ryan M. L. McFadden, Derek Fujimoto, John O. Ticknor, Monika Stachura, Iain McKenzie, Gerald D. Morris, W. Andrew MacFarlane, Jun Sugiyama, Katsuyuki Fukutani, Shinji Tsuneyuki, Taro Hitosugi, *Chemistry of Materials*, 34(8), 3616 - 3623, 2022, DOI:10.1021/acs.chemmater.1c03450

69. Neutron diffraction study on the site occupancy of hydrogen in Fe_{0.95}Si_{0.05} at 14.7 GPa and 800 K.

Yuichiro Mori, Hiroyuki Kagi, Sho Kakizawa, Kazuki Komatsu, Chikara Shito, Riko Iizuka-Oku, Katsutoshi Aoki, Takanori Hattori, Asami Sano-Furukawa, Ken-ichi Funakoshi, Hiroyuki Saitoh, *Journal of Mineralogical and Petrological Sciences*, 116(6), 309 - 313, 2021, DOI:10.2465/jmps.210825

70. ルビジウム化合物に対する高エネルギー分解能蛍光検出 X 線吸収微細構造 (HERFD-XAFS) 測定 - 生体内ウランの化学形の評価法の前検討として.

佐藤 遼太郎, 上原 章寛, 大澤 大輔, 石井 賢司, 松村 大樹, 沼子 千弥, 及川 将一, 武田 (本間) 志乃, *X 線分析の進歩*, 54, 193 - 201, 2023

71. Experimental and theoretical investigation of high resolution X-ray absorption spectroscopy (HR-XAS) at Cu K-edge for Cu₂ZnSnSe₄.

Wei Xu, Yujun Zhang, Kenji Ishii, Hiroki Wadati, Yingcai Zhu, Zhiying Guo, Qianshun Diao, Zhen Hong, Haijiao Han, Lidong Zhao, *Condensed Matter*, 8(1), 8, 2022, DOI:10.3390/condmat8010008

72. Energy domain Synchrotron-Radiation-Based Mössbauer Spectroscopy of EuH₂ under a Few GPa pressure.

Ryo Masuda, Naohisa Hirao, Kosuke Fujiwara, Takaya Mitsui, Taku Fujihara, Hiroyuki Tajima, Masayuki Kurokuzu, Shinji Kitao, Makoto Seto, *Hyperfine Interactions*, 244, 5, 2023, DOI:10.1007/s10751-022-01815-0

73. 電子ドープ型銅酸化物超伝導体 Nd_{1.82}Ce_{0.18}CuO₄ における電荷励起の温度依存性.

石井 賢司, 清水 裕友, 藤田 全基, 水木 純一郎, *SPring-8 / SACLA 利用研究成果集*, 11(1), 19 - 21, 2023, DOI:10.18957/rr.11.1.19

74. Investigation of Hydrogen Superoxide Adsorption during ORR on Pt/C Catalyst in Acidic Solution for PEFC by in-situ High Energy Resolution XAFS.

- Naoki Yamamoto, Daiju Matsumura, Yuto Hagihara, Kei Tanaka, Yuta Hasegawa, Kenji Ishii, Hirohisa Tanaka, *Journal of Power Sources*, 557, 232508, 2023, DOI:10.1016/j.jpowsour.2022.232508
- 75. Intrinsic coercivity in 4f-3d intermetallic magnets with valence fluctuations.**
Hiroaki Shidhido, Tetsuro Ueno, Kotaro Saito, Masahiro Sawada, Munehisa Matsumoto, *Journal of Magnetism and Magnetic Materials*, 562, 169748, 2022, DOI:10.1016/j.jmmm.2022.169748
- 76. Observation of buried magnetic domains in grain-oriented electrical steel.**
Toshiya Inami, Kento Sugawara, Takahiro Nakada, Yui Sakaguchi, Shin Takahashi, *IEEE Transactions on Magnetics*, 59(3), 6000406, 2023, DOI:10.1109/TMAG.2023.3237939
- 77. Rayleigh Scattering of Synchrotron Mössbauer Radiation using a Variable Bandwidth Nuclear Bragg Monochromator.**
Takaya Mitsui, Ryo Masuda, Shinji Kitao, Yasuhiro Kobayashi, Makoto Seto, *Journal of the Physical Society of Japan*, 91, 064001-1 - 064001-8, 2022, DOI:10.7566/JPSJ.91.064001
- 78. Acoustic wave velocities of ferrous-bearing MgSiO₃ glass up to 158 GPa with 2 implications for dense silicate melts at the base of the Earth's mantle.**
Izumi Mashino, Motohiko Murakami, Shinji Kitao, Takaya Mitsui, Ryo Masuda, Makoto Seto, *Geophysical Research Letters*, 49(19), e2022GL098279, 2022, DOI:10.1029/2022GL098279
- 79. First principles molecular dynamics study of proton disorder in C₁' phase of H₂ hydrate.**
Takashi Ikeda, *Chemical Physics Letters*, 811, 140252-1 - 140252-7, 2022, DOI:10.1016/j.cplett.2022.140252
- 80. Field-induced spin nematic Tomonaga-Luttinger liquid of the S = 1/2 spin ladder system with the anisotropic ferromagnetic rung interaction.**
Toru Sakai, Toru Sakai, Ryosuke Nakanishi, Takaharu Yamada, Rito Furuchi, Hiroki Nakano, Hirono Kaneyasu, Kiyomi Okamoto, *Physical Review B*, 106, 064433-1 - 064433-9, 2022, DOI:10.1103/PhysRevB.106.064433
- 81. Comparative theoretical study of x-ray magnetic circularly polarized emission from ferromagnetic Fe, Co and Ni.**
Kobayashi Hiroki, Koide Akihiro, Nomura Takuji, Inami Toshiya, *Europhysics Letters*, 140(3), 36002, 2022, DOI:10.1209/0295-5075/ac9d5f
- 82. Exciton-assisted low-energy magnetic excitations in a photoexcited Mott insulator on a square lattice.**
Kenji Tsutsui, Kazuya Shinjo, Shigetoshi Sota, Takami Tohyama, *Communications Physics*, 6, 41, 2023, DOI:10.1038/s42005-023-01158-4
- 83. S = 2 Quantum Spin Chain with the Biquadratic Exchange Interaction.**
Toru Sakai, Takaharu Yamada, Ryosuke Nakanishi, Rito Furuchi, Hiroki Nakano, Hirono Kaneyasu, Kiyomi Okamoto, Takashi Tonegawa, *Journal of the Physical Society of Japan*, 91, 074702-1 - 074702-5, 2022, DOI:10.7566/JPSJ.91.074702
- 84. Field-Induced Quantum Spin Nematic Liquid Phase in the S=1 Antiferromagnetic Heisenberg Chain with Additional Interaction.**
Toru Sakai, Hiroki Nakano, Rito Furuchi, Kiyomi Okamoto, *Journal of Physics Conference Series*, 2164, 012030-1 - 012030-4, 2022, DOI:10.1088/1742/6596/2164/1/012030
- 85. Magnetization Plateau of the Distorted Diamond Spin Chain with Anisotropic Ferromagnetic Interaction.**
Toru Sakai, Kiyomi Okamoto, Hiroki Nakano, Rito Furuchi, *AIP Advances*, 12, 035030-1 - 035030-4, 2022, DOI:10.1063/9.0000255
- 86. The Haldane Gap of the S = 1 Heisenberg Antiferromagnetic Chain.**
Hiroki Nakano, Hiroto Tadano, Norikazu Todoroki, Toru Sakai, *Journal of the Physical Society of Japan*, 91, 074701-1 - 074701-5, 2022, DOI:10.7566/JPSJ.91.074701
- 87. Uranium chelating ability of decorporation agents in serum evaluated by X-ray absorption spectroscopy.**
Akihiro Uehara, Daiju Matsumura, Takuya Tsuji, Haruko Yakumaru, Izumi Tanaka, Ayumi Shiro, Hiroyuki Saitoh, Hiroshi Ishihara, Shino Takeda, *Analytical Methods*, 14(24), 2439 - 2445, 2022, DOI:10.1039/d2ay00565d

- 88. Effect of closeness between a few atoms forming a cluster ion passing through water on the motion of secondary electrons and radial dose.**
Moribayashi Kengo, Radiation Physics and Chemistry, 208, 110870, 2023, DOI:10.1016/j.radphyschem.2023.110870
- 89. Fly casting with ligand sliding and orientational selection supporting complex formation of aGPCR and a middle sized flexible molecule.**
Junichi Higo, Kota Kasahara, Gert-Jan Bekker, Benson Ma, Sakuraba Shun, Shinji Iida, Narutoshi Kamiya, Ikuo Fukuda, Kono Hidetoshi, Yoshifumi Fukunishi, Haruki Nakamura, Scientific Reports, 12, 13792, 2022, DOI:doi.org/10.1038/s41598-022-17920-7
- 90. Free energy landscape of H2A-H2B displacement from nucleosome.**
Ishida Hisashi, Kono Hidetoshi, Journal of Molecular Biology, 434(16), 167707, 2022, DOI:10.1016/j.jmb.2022.167707
- 91. 高塩濃度下におけるヌクレオソーム DNA の解離.**
石田 恒, 河野 秀俊, HPCI 利用研究成果集, 7(2), 2022
- 92. SPRTN and TDP1/TDP2 independently suppress 5-aza-2'- deoxycytidine induced genomic instability in human TK6 cell line.**
Nakano Toshiaki, Moriwaki Takahito, Tsuda Masataka, Miyakawa Misa, Hanaichi Yuto, Sasanuma Hiroyuki, Hirota Koji, Kawanishi Masanobu, Ide Hiroshi, Tano Keizo, Bessho Tadayoshi, Chemical Research in Toxicology, 35(11), 2059 - 2067, 2022, DOI:10.1021/acs.chemrestox.2c00213
- 93. Exhaustive sampling of intrinsically disordered protein docking conformation with ALS simulation.**
Ikebe Jinzen, Kono Hidetoshi, HPCI 利用研究成果集, 7(1), 23 - 32, 2022
- 94. RNAPII driven post-translational modifications of nucleosomal histones.**
Wai Soon Chan, Amarjeet Kumar, Kono Hidetoshi, Trends in Genetics, 38(10), 1076 - 1095, 2022, DOI:10.1016/j.tig.2022.04.010
- 95. Unusual microwave heating of water in reverse micellar solution.**
Murakami Hiroshi, Scientific Reports, 13, 5025-1 - 5025-7, 2023, DOI:10.1038/s41598-023-31742-1
- 96. 軟 X 線レーザーによるアブレーション研究.**
石野 雅彦, 三上 勝大, チン タンフン, 錦野 将元, フォトニクスニュース, 8(2), 83 - 87, 2022
- 97. プラズマシミュレーションの新型コロナウイルス感染症のモデリングへの応用.**
佐々木明, プラズマ・核融合学会誌, 98, 407 - 414, 2022

Proceedings

- 1. Design, prototyping, and evaluation of soft X-ray high diffraction efficiency and wide acceptance angle laminar-type W/C multilayer diffraction grating for 200-900 eV range.**
羽多野 忠, 小池 雅人, ピロジコフ アレキサンダー, 林 信和, 垣尾 翼, 長野 哲也, Photon Factory Activity Report, 39, 2022
- 2. Design and preliminary fabrication and evaluation of small incident angle and high diffraction efficiency laminar-type diffraction grating optimized for the state analysis at the vicinity of Li-K emission.**
小池 雅人, 羽多野 忠, ピロジコフ アレキサンダー, 林 信和, 垣尾 翼, 長野 哲也, 寺内 正己, Photon Factory Activity Report, 39, 2022
- 3. A study of self-vetoing balloon vessel for liquid-scintillator detectors.**
S.Obara, Y.Gando, S.Ieki, H.Ikeda, K.Ishidoshiro, R.Nakamura, Journal of Physics: Conference Series, 2374(1), 12111, 2022, DOI:10.1088/1742-6596/2374/1/012111
- 4. X 線吸収スペクトルの主成分分析による血清中ウランに結合する配位子の結合割合評価.**
上原 章寛, 松村 大樹, 薬丸 晴子, 城 鮎美, 田中 泉, 辻 卓也, 齋藤 寛之, 石原 弘, 武田 志乃, Fundamental of Toxicological Sciences, 9, 119, 2022

5. Effect of the thermalization of secondary electron energies on plasma formation during the irradiation of heavy ions.

Moribayashi Kengo, Nuclear Inst. and Methods in Physics Research, B, 537, 129 - 132, 2023, DOI:10.1016/j.nimb.2023.02.014

6. Investigation of EUV emission from Sn to rare-earth plasmas in terms of the accuracy of the atomic data and completeness of atomic model.

A. Sasaki, Proceedings of SPIE Optical and EUV Nanolithography XXXVI, 124940, 2023

表彰

1. レーザー学会学術講演会第 43 回年次大会 優秀ポスター発表賞.

浅井 孝文 「高強度レーザーとサブミクロンサイズのクラスターターゲットとの相互作用による数百テスラ級自己生成磁場計測」

一般社団法人レーザー学会, 2023-01-19

2. 2022 年日本物理学会秋季大会 学生優秀発表賞.

南 卓海 「kJ 級ピコ秒レーザーの直接照射による large-area suspended graphene target を用いたイオン加速」

日本物理学会, 2022-11-17

3. 2022 年日本物理学会秋季大会 学生優秀発表賞.

浅井 孝文 「水素クラスターターゲットと高強度レーザーとの相互作用による準単色 multi-MeV 陽子線の繰り返し発生」

日本物理学会, 2022-11-17

4. IoP Outstanding Reviewer Awards 2021.

Alexander Pirozhkov Outstanding Reviewer for Plasma Physics and Controlled Fusion journal in 2021

IoP Publishing, 2022-04-26

5. The 11th Advanced Lasers and Photon Sources Conference (ALPS2022), The Best Student Poster Paper Award.

Watanabe Kento "Passive Coherent Beam Combining Based on Divided Pulse Sagnac Geometry"

The 11th Advanced Lasers and Photon Sources Conference (ALPS2022), 2022-04-21

6. The 41st JSST Annual International Conference on Simulation Technology, Student Presentation Award.

Kawanami Ryuta "Molecular dynamics study of microscopic mechanism of OH radical-induced DNA damage"

日本シミュレーション学会 (JSST), 2022-11-01

7. The 41st JSST Annual International Conference on Simulation Technology, Student Poster Presentation Award.

Terakawa Kazushi "Molecular Dynamics Study on Cluster Damaged DNA Containing Apurinic/Apyrimidinic Sites"

日本シミュレーション学会 (JSST), 2022-09-02

8. 第 69 回応用物理学会春季学術講演会ポスター賞受賞.

福家 聖也、佐々木 拓生、川合 良知、日比野 浩樹 「c 面サファイア上に成長させたグラフェン上における GaN リモートエピタキシーのその場 XRD 解析」

公益社団法人応用物理学会, 2022-05-27

9. 11th International Workshop on Sample Environment at Scattering Facilities (ISSE workshop 2022), Poster Award.

Fujiwara Kosuke "Installation of a multi-purpose 4-circle diffractometer for synchrotron Mossbauer source in BL11XU"

The International Society for Sample Environment, 2022-09-01

特許登録

- 1. イオン加速方法.**
福田 祐仁, 岸本 泰明, 松井 隆太郎
日本 7095196 (2022-06-27)
- 2. 血中物質濃度測定装置及び血中物質濃度測定方法.**
Yamakawa Koichi
日本 HK 1243902 (2022-04-08)
- 3. 組織識別装置、組織識別システム、組織識別方法、検査方法、内視鏡システム、組織識別プログラムおよび記録媒体.**
Yamakawa Koichi, Aoyama Makoto, Morioka Takamitsu, Imaoka Tatsuhiko, Ogawa Kanade
韓国 10-2439281 (2022-08-29)
- 4. 組織識別装置、組織識別システム、組織識別方法、検査方法、内視鏡システム、組織識別プログラムおよび記録媒体.**
Yamakawa Koichi, Aoyama Makoto, Morioka Takamitsu, Imaoka Tatsuhiko, Ogawa Kanade
EU 3792618 (2022-08-24)
- 5. Laser device, light source, and measurement device.**
Akahane Yutaka, Aoyama Makoto, Ogawa Kanade, Yamakawa Koichi
EU 18854859.8-1212 (2023-01-09)
- 6. Laser device, light source, and measurement apparatus.**
Akahane Yutaka, Aoyama Makoto, Ogawa Kanade, Yamakawa Koichi
米国 US 11482831 (2022-10-25)
- 7. 水素吸蔵材、水素化水素吸蔵材の製造方法および水素吸蔵合金の製造方法.**
齋藤 寛之, 谷上 真惟, 森本 勝太, 綿貫 徹
日本 7207685 (2023-1-10)
- 8. MAGNETIC MATERIAL OBSERVATION METHOD, AND MAGNETIC MATERIAL OBSERVATION APPARATUS.**
Toshiya Inami, Tetsu Watanuki, Tetsuro Ueno, Ryo Yasuda
米国 US11474169 (2022-10-18)
- 9. 磁性体観察方法および磁性体観察装置.**
稲見 俊哉, 綿貫 徹, 上野 哲朗, 安田 良
日本 7129109 (2022-08-24)

特許出願

- 1. 鉄含有擬立方晶マンガン基フェリ磁性ホイスラー合金、及び、これを用いた磁気抵抗記憶素子.**
境 誠司, Bentley Phillip David, 李 松田, 三井 隆也, 藤原 孝将, 増田 啓介, 三浦 良雄
特願 2023-027745 (2023-02-24)
- 2. 測定システム、プログラム、測定方法、及びレーザ加速自由電子レーザ装置.**
中新 信彦, 近藤 康太郎, 黄 開, 神門 正城, 細貝 知直, 金 展
特願 2023-27811 (2023-02-24)
- 3. イオン発生装置、イオン発生方法、およびイオン発生用ターゲット.**
小島 完興, 榊 泰直, 宮武 立彦, 近藤 公伯, 黒木 宏芳, 清水 祐輔, 原田 寿典, 井上 典洋
特願 2022-190747 (2022-11-29)
- 4. 光音響波発生装置、光音響波発生方法及び組成推定方法.**
坪内 雅明
特願 2022-091646 (2022-06-06)
- 5. X線回折測定方法およびX線回折測定装置.**
大和田 謙二, 町田 晃彦, 押目 典宏, 菅原 健人, 綿貫 徹
特願 2022-125870 (2022-08-05)
- 6. 表面造形方法及び表面造形装置.**
石野 雅彦, チン タンフン, 錦野 将元, 三上 勝大
特願 2023-041379 (2023-03-15)

The Kids' Science Museum of Photons

概要

きつづ光科学館ふおとんでは、2022年度も新型コロナウイルスの感染拡大防止対策として、年度当初より事前予約制や受け入れ人数の制限等の下でプラネタリウムの上映を行いました。また、月替わりのウェルカムボードとして偏光グラフィックス作品の作成・展示も行いました。

2022年7月23日からは、事前予約制等は継続しつつ、プラネタリウム上映に加えて館内展示ゾーンの一部の見学を再開しました。ご家族連れや近隣府県の保育園、幼稚園、小中高の学校関連、その他の見学ツアー主催団体にもご利用いただきました。また、関東地区の公立の展示館から、光をテーマとした特別展を企画するために、当館の展示物を参考にしたいとご来館いただいたりもしました。



梅美台小学校の見学

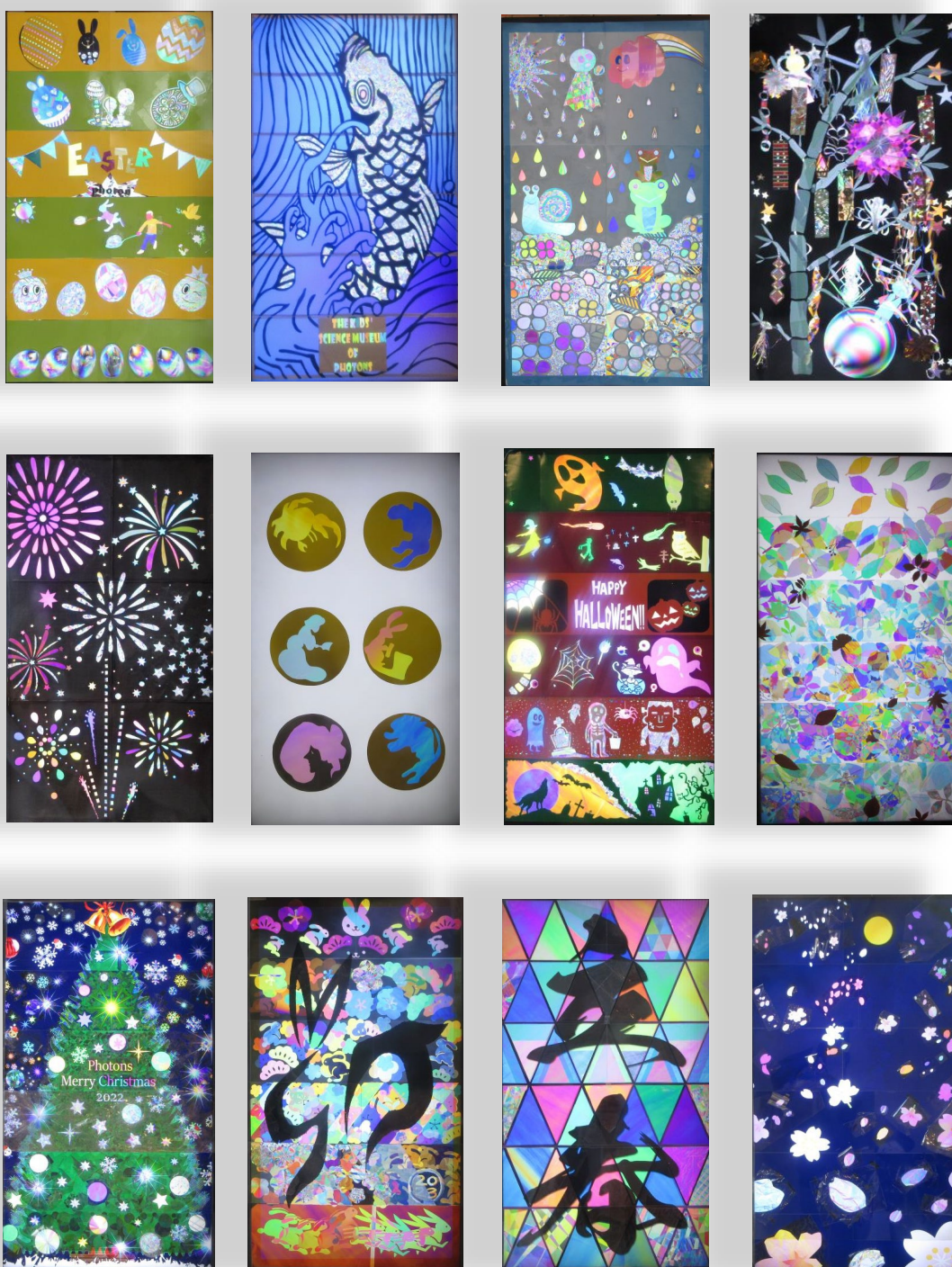
2023年3月1日からは、事前予約や入館人数、滞在時間の制限を無くしました。またプラネタリウムの上映も定員を約60名に緩和いたしました。一部の例外の展示装置は残りますが、新型コロナウイルスの感染拡大防止のため臨時休館することとなった2020年2月27日以来3年ぶりに通常運用に近い形での再開となりました。

来館者数および映像コンテンツ上映の実績

2022年度は、6,373人の方々にご来館いただきました。また、光の映像ホール（ドーム型全天周映像ホール）において、事前予約制や受け入れ人数の制限等の下でプラネタリウムの上映を行い、観覧者総数は5,662人でした。3月からは入館制限を無くし、プラネタリウムの定員も緩和した結果、多くの方にご来館いただきました。

来館者数および上映実績（2022年4月1日～2023年3月31日）

年 月	来館者数	上映回数	観覧者数
2022年4月	147人	30回	147人
5月	292人	22回	292人
6月	297人	21回	288人
7月	703人	38回	700人
8月	929人	41回	916人
9月	510人	30回	506人
10月	552人	26回	531人
11月	394人	28回	386人
12月	239人	23回	236人
2023年1月	278人	26回	277人
2月	373人	25回	344人
3月	1,659人	40回	1,039人
年度合計	6,373人	350回	5,662人



月替わりの偏光グラフィックス展示

Appendix

共同研究課題、施設共用課題

1) 木津地区

【共同研究課題】

共同研究先	共同研究課題名	担当研究グループ
東京大学	半古典 Vlasov 方程式に基づくレーザー加工シミュレータの研究開発	超高速光物性研究グループ
日本電信電話株式会社	アト秒パルスの波形計測と時間分解計測に関わる基盤技術開発	超高速光物性研究グループ
株式会社フォトラボ	レーザー誘起振動波計測技術の小型化に関する研究	X線レーザー研究グループ
理化学研究所	テラヘルツパルス光源による高分子高次構造の制御	超高速光物性研究グループ
筑波大学	光・電子融合第一原理ソフトウェア「SALMON」の開発及び利用研究	超高速光物性研究グループ
大阪大学	フェムト秒レーザー・物質相互作用の高速計測に関する研究	高強度レーザー科学研究グループ
大阪大学、東北大学	シンチレータを用いた相対論的イオン検出手法の開発	先端レーザー技術開発グループ
大阪大学	超高強度レーザーと固体物質からのガンマ線発生及び核物理に関する研究	高強度レーザー科学研究グループ
宇都宮大学、広島大学、東北大学	高輝度軟X線発生に関する基礎研究	X線レーザー研究グループ
京都大学	TW 級チタンサファイアレーザーを用いた量子ビーム発生と応用に関する研究	X線レーザー研究グループ
芝浦工業大学	レーザー誘起振動波計測技術の高度化に関する研究	X線レーザー研究グループ
NTT アドバンステクノロジー株式会社	高耐力軟X線光学素子に関する基礎研究	X線レーザー研究グループ
東京学芸大学	リラクサー強誘電体のドメイン形成に関する研究	X線レーザー研究グループ
ライトタッチテクノロジー株式会社	中赤外レーザーを用いた医療応用計測技術の開発	光量子科学研究部
奈良先端科学技術大学院大学	二次元層状半導体における光誘起状態制御に関する基盤技術開発	超高速光物性研究グループ
兵庫県立粒子線医療センター	量子メスに向けた粒子線照射計測及び制御技術に関する研究	高強度レーザー科学研究グループ
東北大学、株式会社島津製作所	極端紫外線領域の低入射角回折格子の開発	先端レーザー技術開発グループ

同志社大学	フェムト秒パルスレーザーの位相受動整合コヒーレント加算に関する研究	先端レーザー技術開発グループ
神戸大学、名古屋大学、日本原子力研究開発機構	固体飛跡検出器を用いた高エネルギーイオン検出手法開発	先端レーザー技術開発グループ
大阪大学、青山学院大学、九州大学	宇宙物理の手法に基づく粒子加速・電磁放射に関する研究	先端レーザー技術開発グループ
核融合科学研究所、京都工芸繊維大学、富山高等専門学校	凝縮相の量子・分子動力学計算に関する研究	X線レーザー研究グループ
大阪大学	レーザー電子加速の安定化・性能評価研究	高強度レーザー科学研究グループ
住友重機械工業株式会社	量子メス用レーザー加速入射器の炭素ビーム評価手法の開発	高強度レーザー科学研究グループ
日立造船株式会社	量子メス用レーザー加速入射器のターゲット駆動装置に関する研究開発	高強度レーザー科学研究グループ
日本電子株式会社	電子顕微鏡搭載用高感度軟 X 線回折格子分光器の開発	光量子科学研究部
株式会社日本防振工業	レーザー電子加速に資する防振・光軸安定化に関する研究	高強度レーザー科学研究グループ
大阪大学	レーザー駆動イオン加速ビームの安定性向上に関する研究	X線レーザー研究グループ
日本原子力研究開発機構	加速器質量分析におけるレーザーを用いた同重体分離の基礎研究	先端レーザー技術開発グループ
金属技研株式会社	レーザー加速による小型 X 線光源加速器の設計研究	高強度レーザー科学研究グループ
近畿大学	軟 X 線レーザー照射による酸化物表面の微細加工に関する研究	X線レーザー研究グループ
東京大学	強レーザー場誘起イオン化における光電子波動関数観測に関する基盤技術開発	超高速光物性研究グループ

【施設共用課題】

課題番号	利用区分	施設装置	利用課題
2022A-K01	公開	QUADRA-T レーザーシステム	高出力ピコ秒励起パルスを用いた光パラメトリック増幅の研究
2022A-K02	公開	kHz チタンサファイアレーザー	二次元層状半導体における光誘起状態制御に関する基盤技術開発
2022A-K03	公開	J-KAREN-P レーザー装置	高強度レーザー駆動非平衡輻射高 Z プラズマの形成過程と輻射特性の解明

2022A-K05	公開	J-KAREN-P レーザー装置	J-KAREN-P レーザーを用いた誘導コンプトン散乱の実験
2022A-K06	公開	J-KAREN-P レーザー装置	グラフェンを用いたレーザーイオン加速におけるエネルギーフロンティアの開拓
2022A-K07	公開	J-KAREN-P レーザー装置	高強度レーザーによるプロトンの航跡場加速実験
2022A-K08	公開	J-KAREN-P レーザー装置	極限的電磁波のトムソン散乱を用いた非平衡プラズマ診断
2022A-K10	公開	J-KAREN-P レーザー装置	多チャンネルシンチレーション検出器を用いた GeV イオンの質量分解分光法の開発

2) 播磨地区

【共同研究課題】

共同研究先	共同研究課題名	担当研究グループ
日本原子力研究開発機構	放射光による物質科学に関する研究	放射光科学研究センター
京都大学	同位体特定による局所状態解明のための先進的メスbauer分光法の開発研究	磁性科学研究グループ
東北大学、上智大学	X線吸収分光・発光分光による銅酸化物超伝導体の研究	磁性科学研究グループ
JEF テクノリサーチ株式会社	磁気円偏光発光を用いた方向性珪素鋼板の内部磁区観察のための研究開発	磁性科学研究グループ
SLAC National Accelerator Laboratory	角度分解光電子分光による銅酸化物高温超伝導体における電子・格子相互作用の解明(受託研究: 二国間交流事業共同研究/セミナー)	磁性科学研究グループ
京都大学、分子科学研究所、理化学研究所	コヒーレント X 線を利用したナノ粒子計測に関する研究	コヒーレント X 線利用研究グループ
広島大学	コヒーレント X 線を利用した強誘電体一粒子計測	コヒーレント X 線利用研究グループ
TDK 株式会社	放射光 X 線回折を用いた構造解析技術の開発	コヒーレント X 線利用研究グループ
産業技術総合研究所	水素雰囲気その場・時分割放射光 X 線全散乱を利用した水素吸蔵合金の構造変化の観測	高圧・応力科学研究グループ
京都大学	ナノ粒子を取り込んだがん細胞に及ぼす高エネルギー単色 X 線照射の影響に関する研究	高圧・応力科学研究グループ
物質・材料研究機構	原子二体分布関数法による機能性材料の先進的ナノ構造研究	高圧・応力科学研究グループ

【施設共用課題】

播磨地区では、2012年度より受託していた文部科学省ナノテクノロジープラットフォーム事業が2021年度に終了し、代わって文部科学省マテリアル先端リサーチインフラ事業を受託しています。当該事業では2022年度から放射光科学研究施設を成果公開型課題で利用する外部研究者に対して、特に専用ビームラインにおける研究支援を強化しています。課題は年2回、SPring-8を運営する公益財団法人高輝度光科学研究センターの一般課題募集時期（5月及び11月）に合わせて募集しています。

課題番号	利用区分	施設装置	利用課題
2022A-H01	公開	放射光メスバウアー分光装置	放射光メスバウアー4軸回折計の開発
2022A-H02	公開	放射光メスバウアー分光装置	高水素圧力下におけるEu水素化物の電子状態分析II
2022A-H03	公開	放射光メスバウアー分光装置	ペリドタイトガラスの超高压下における鉄の電子状態とその電気伝導度への影響：地球進化・内部構造におけるメルトの寄与の解明に向けて
2022A-H07	公開	高温高压プレス装置	高压下での新規La-Ni水素化物の形成過程の観測
2022A-H08	公開	高温高压プレス装置	高压合成技術を活用した熱化学式水素圧縮機用新規水素吸蔵合金の水素放出挙動の観察2
2022A-H09	公開	高温高压プレス装置	高压高温場でのTiリッチなTi-Mg二元合金の相変化のその場観察
2022A-H10	公開	高温高压プレス装置	Li-Re系遷移金属錯体水素物の高温高压合成過程におけるLi ₂ O添加効果
2022A-H11	公開	高温高压プレス装置	突合せ溶接配管の底部のひずみマップ測定
2022A-H12	公開	高温高压プレス装置	放射光白色X線を用いた高強度鋼板-アルミニウム合金異種材料抵抗スポット溶接継手の内部ひずみ分布の測定
2022A-H13	公開	高速2体分布関数計測装置	放射光を用いた全散乱法による次世代二次電池材料のin situ 測定
2022A-H14	公開	高速2体分布関数計測装置	PDF解析によるPb含有ペロブスカイト酸化物の負熱膨張関連相転移機構の解明
2022A-H16	公開	高速2体分布関数計測装置	Investigation of the structural changes and deformation behavior of N-A-S-H under compressive load and high temperature
2022A-H17	公開	コヒーレントX線回折イメージング装置	電子デバイス内部に実装された単結晶ナノ粒子の非破壊三次元構造可視化技術の確立

2022A-H18	非公開	コヒーレントX線回折イメージング装置	異材接合部における内部残留歪み(応力)の測定
2022B-H02	公開	放射光メスバウアー分光装置	Imaging of hyperfine interactions
2022B-H03	公開	放射光メスバウアー分光装置	核共鳴散乱を用いた混合原子価鉄酸化物の電荷秩序配列の検証
2022B-H04	公開	放射光メスバウアー分光装置	ガンマ線光子相関時間測定系の開発研究
2022B-H05	公開	放射光メスバウアー分光装置	超高压下におけるケイ酸塩ガラス中の鉄の電子状態：地球深部メルトの安定性の解明
2022B-H06	公開	放射光メスバウアー分光装置	放射光メスバウアー分光を用いた高压下でのペリドタイトガラスの鉄スピン転移の観察
2022B-H07	公開	共鳴非弾性X線散乱装置	Untangling the structural, magnetic dipole, and charge multipolar orders in Ba ₂ MgReO ₆
2022B-H08	公開	共鳴非弾性X線散乱装置	高分解能 XAFS を利用した燃料電池カソード 電極触媒上における酸素還元反応時の吸着構造解明研究
2022B-H09	公開	共鳴非弾性X線散乱装置	深さ分解手法を用いた方向性電磁鋼板の内部磁区構造調査
2022B-H10	公開	表面X線回折計	ヘテロリモートエピタキシーにおけるGa ₂ N核を用いた結晶化過程の観察
2022B-H11	公開	表面X線回折計	高品質InGa ₂ Nエピタキシャル結晶実現のための成長その場X線回折測定
2022B-H12	公開	表面X線回折計	グラフェンを直接成長させたサファイア基板上でのGa ₂ NリモートエピタキシーのリアルタイムX線回折
2022B-H13	公開	高温高压プレス装置	超高压水素下でのホウ化水素シートの加熱による構造変化解析
2022B-H14	公開	高温高压プレス装置	酸化物イオン拡散を利用した酸素欠損BaTiO _{3-δ} のその場観察
2022B-H15	公開	高温高压プレス装置	鉄鋼材料の高温圧縮・等温保持過程のX線その場観測
2022B-H16	公開	高温高压プレス装置	高温高压下におけるバナジウム酸水素化物のアニオン秩序-無秩序相転移の探索
2022B-H17	公開	高温高压プレス装置	空隙を有する金属間化合物NiInの水素吸蔵反応の観測
2022B-H18	公開	高温高压プレス装置	遷移金属錯体水素化物Li ₂ ReH ₉ の最適合成条件探索
2022B-H19	公開	高温高压プレス装置	高压合成技術を活用した高压作動型水素吸蔵合金の相変化挙動の観察

2022B-H20	公開	高速2体分布関数計測装置	载荷による加速炭酸化養生した純粋多様なカルシウムシリケート硬化体の反応生成物構造解析及び変形挙動特性解明
2022B-H22	公開	高速2体分布関数計測装置	高温作動型水素吸蔵材料の高温・水素ガス雰囲気下での水素吸蔵・放出反応の観察
2022B-H23	公開	コヒーレントX線回折イメージング装置	放射光を用いた一軸ひずみ下精密構造解析によるネマティック超伝導体 $Cu_xBi_2Se_3$ の新奇な超伝導電子対形成機構の解明
2022B-H24	公開	コヒーレントX線回折イメージング装置	電子デバイス内部に実装された単結晶ナノ粒子の非破壊三次元構造可視化技術の確立II
2022B-H25	公開	コヒーレントX線回折イメージング装置	Bragg-CDIによる正方晶巨大負熱膨張物質のドメイン構造温度変化の観察
2022B-H26	公開	コヒーレントX線回折イメージング装置	形状制御強誘電体ナノ結晶における構造と物性
2022B-H27	非公開	共鳴非弾性X線散乱装置	方向性電磁鋼板の放射光磁区観察
2022B-H28	非公開	コヒーレントX線回折イメージング装置	円筒缶かしめ部の応力解析

関西光科学研究所での各種シンポジウム・施設公開・出展・アウトリーチ活動

新型コロナウイルス感染症（COVID-19）の影響も落ち着いてきたため、2022年度はアウトリーチ活動として、地元のイベントに出展する等、昨年度に比べて活動の場が増えてきました。関西研の各種シンポジウム・施設公開・出展・アウトリーチ活動について主なものを記載します。

年1回の施設公開について木津地区では2022年10月22日（土）に人数制限・事前登録のうえ当日の感染症対策を徹底して開催しました。なお、播磨地区での開催は見送りました。

【木津地区】

1	6-JUN-2022	オンライン開催	主催：「レーザー駆動による量子ビーム加速器の開発と実証」プロジェクト
	JST 未来社会創造事業 「レーザー駆動による量子ビーム加速器の開発と実証」		
2	28-29-JUN-2022	関西光科学研究所（木津地区：京都府木津川市） オンライン・現地ハイブリッド開催	主催：量研 関西光科学研究所、大阪大学 レーザー科学研究所
	光・量子ビーム科学合同シンポジウム 2022 The Joint Symposium on Optical and Quantum Beam Science (OPTO2022) 併催：「パワーレーザーDXプラットフォーム」シンポジウム Power Laser DX Platform Symposium		

3	30-31-JUL-2022	東京都 科学技術館	主催：科学技術館
	青少年のための科学の祭典 2022 全国大会		
4	21-AUG-2022	大阪科学技術館	主催：大阪科学技術館
	大阪科学技術館夏休みイベント「出展者スペシャルDAY」		
5	6-7-OCT-2022	オンライン開催	主催：けいはんな R&D フェア実行委員会
	けいはんな R&D フェア 2022		
6	6-7-OCT-2022	けいはんなオープンイノベーションセンター	主催：関西文化学術研究都市推進機構
	けいはんなビジネスマッセ 2022		
6	22-OCT-2022	関西光科学研究所	主催：関西光科学研究所
	関西光科学研究所（木津地区）施設公開		
7	8-9-FEB-2023	関西光科学研究所 オンライン・現地ハイブリッド開催	主催：量研 関西光科学研究所、理化学研究所 光量子工学研究センター
	第 6 回 RIKEN-RAP & QST-KPSI ジョイントセミナー		
8	12-MAR-2023	上人ヶ平遺跡公園	主催：木津川アートプロジェクト事務局
	木津川アートプレイイベント「くうそうのはらっぱ」 出展内容：工作教室「偏光ステンドグラスを作ろう」		

【播磨地区】

1	28-APR-2-MAY-2022	オンライン開催	主催：SPring-8/SACLA 施設公開実行委員会
	2022 年第 30 回 SPring-8&SACLA オンライン施設公開		
2	1-JUN-2022	オンライン開催	主催：国立研究開発法人物質・材料研究機構マテリアル先端リサーチインフラセンターハブ運営室
	文部科学省マテリアル先端リサーチインフラ技術支援者意見交換会		
3	10-13-JUL-2022	SPring-8	主催：兵庫県立大学理学部・大学院理学研究科、 関西学院大学理学部・工学部・生命環境学部・ 大学院理工学研究科、東京大学シンクロトン 放射光連携研究機構、岡山大学、大阪大学未来 戦略光科学連携センター・蛋白質研究所・核物 理研究センター、茨城大学大学院理工学研究 科、高輝度光科学研究センター（JASRI）、理 化学研究所 放射光科学研究センター、日本原 子力研究開発機構 物質科学研究センター、量 研 関西光科学研究所
	第 22 回 SPring-8 夏の学校		

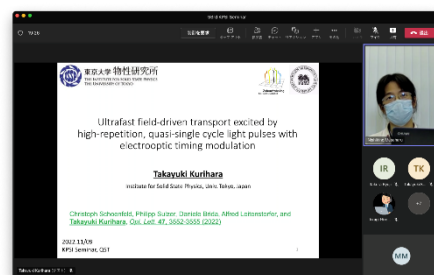
4	29-JUL-2022	SPring-8	主催：国立研究開発法人物質・材料研究機構マテリアル先端リサーチインフラセンターハブ運営室
	文部科学省マテリアル先端リサーチインフラサイトビジット		
5	8-12-AUG-2022	SPring-8	主催：国立研究開発法人物質・材料研究機構マテリアル先端リサーチインフラセンターハブ運営室
	文部科学省マテリアル先端リサーチインフラ学生研修プログラム		
6	2-SEP-2022	オンライン開催	主催：原子力機構物質科学研究センター、量研関西研放射光科学研究センター
	令和4年度文部科学省マテリアル先端リサーチインフラ事業 JAEA & QST 合同放射光利用講習会ーバルク・表層の反応・合成解析ー		
7	4-7-SEP-2022	SPring-8	主催：SPring-8 ユーザー協団体、(公財)高輝度光科学研究センター
	第6回 SPring-8 秋の学校		
8	6-7-SEP-2022	オンライン開催	主催：日本放射光学会
	第14回日本放射光学会 放射光基礎講習会 放射光の基礎と活用の可能性		
9	7-9-SEP-2022	幕張メッセ	主催：一般社団法人日本分析機器工業会、一般社団法人日本科学機器協会
	JASIS2022		
10	15-SEP-2022	文部科学省研究交流センター+オンライン開催	主催：国立研究開発法人物質・材料研究機構マテリアル先端リサーチインフラセンターハブ運営室
	文部科学省マテリアル先端リサーチインフラ令和4年度利用成果発表会		
11	16-SEP-2022	文部科学省研究交流センター+オンライン開催	主催：国立研究開発法人物質・材料研究機構マテリアル先端リサーチインフラセンターハブ運営室
	令和4年度文部科学省マテリアル先端リサーチインフラ学生研修プログラム成果発表会		
12	25-26-SEP-2022	SPring-8+オンライン開催	主催：SPring-8 ユーザー協団体、理化学研究所放射光科学研究センター、高輝度光科学研究センター、東京大学
	SPring-8 シンポジウム 2022		
13	19-OCT-7-DEC-2022	NIMS、北海道大学、東北大学	主催：国立研究開発法人物質・材料研究機構マテリアル先端リサーチインフラセンターハブ運営室
	令和4年度文部科学省マテリアル先端リサーチインフラ技術スタッフ交流プログラム		
14	8-9-DEC-2022	東京大学本郷地区	主催：国立研究開発法人物質・材料研究機構マテリアル先端リサーチインフラセンターハブ運営室
	令和4年度文部科学省マテリアル先端リサーチインフラ技術スタッフ集合研修会		

15	7-9-JAN-2023	立命館大学びわこ・くさつキ ャンパス+オンライン開催	主催：第 36 回日本放射光学会年会・放射光科 学合同シンポジウム組織委員会
	第 36 回日本放射光学会年会・放射光科学合同シンポジウム		
16	1-3-FEB-2023	東京ビッグサイト+オンライ ン開催	主催：nano tech 2023 実行委員会
	第 22 回国際ナノテクノロジー総合展・技術会議 (nano tech 2023)		
17	3-FEB-2023	東京ビッグサイト+オンライ ン開催	主催：文部科学省マテリアル先端リサーチイン フラ、物質・材料研究機構マテリアル先端 リサーチインフラセンターハブ運営室
	文部科学省マテリアル先端リサーチインフラ第 21 回マテリアル戦略総合シンポジウム (JAPAN NANO 2023) マテリアル先端リサーチインフラが推進するマテリアル DX プラットフォーム構築		
18	21-FEB-2023	オンライン開催	主催：京都大学 ARIM 解析・計測プラットフ ォーム、日本原子力研究開発機構 JAEA マテ リアル先端リサーチインフラ、量研 QST マテ リアル先端リサーチインフラ
	令和 4 年度文部科学省マテリアル先端リサーチインフラ事業京大・JAEA・QST 解析・計測合同地域 セミナー -最新の微細構造・状態解析-		
19	13-MAR-2023	イーグレひめじ	主催：兵庫県立大学高度産業科学技術研究所
	ニューズバルシンポジウム 2023		

KPSI セミナー (第 86 回～96 回)

QST 木津地区では国内外の著名な研究者をお招きして学術的に最先端の専門的なセミナーを開催しています。今年度は人数制限した会場からオンライン中継も行うハイブリッドセミナーを中心に合計 11 回開催しました。開催にあたっては KPSI Web サイトを活用し、関西研内外に開催案内を行っています。また報告については Web サイト、関西研だより等を活用しています。(参加費無料・事前登録制)

Web サイト：<https://www.qst.go.jp/site/kansai-topics/29853.html>



第 93 回 東京大学 栗原博士
ハイブリッド開催の様子

86	15-APR-2022	Dr. Oue Daigo	The Blackett Laboratory, Imperial College London
	Scattering from "a space-time grating" Asymmetric diffraction and Vavilov-Čerenkov radiation		
87	30-MAY-2022	Dr. Fukahori Shinichi	The University of Tokyo
	Dynamics of molecular rotational wave packets induced by intense ultrashort pulsed laser fields		
88	8-JUN-2022	Prof. Yasui Takeshi	Institute of post-LED Photonics, Tokushima University
	A century of light pioneered by invisible light		

89	14-JUL-2022	Dr. Kosuge Atsushi	Tsuruga Comprehensive Research and Development Center, Japan Atomic Energy Agency
Development of CW fiber laser decontamination using high-speed scanning of high-power density laser beam ~Understanding the laser decontamination mechanism~			
90	28-JUL-2022	Prof. Ishizaki Akihito	Institute for Molecular Science, National Institutes of Natural Science
Quantum Biophysics: Old Roots, New Shoots			
91	9-SEP-2022	Dr. Taya Hidetoshi	RIKEN
Recent theoretical development in Schwinger effect			
92	5-OCT-2022	Prof. Kobayashi Yoichi	Ritsumeikan University
Exploring Novel Photofunctions of Organic-Inorganic Nanohybrids			
93	9-NOV-2022	Dr. Kurihara Takayuki	Institute for Solid State Physics, The University of Tokyo
Ultrafast field-driven transport excited by high-repetition, quasi-single cycle light pulses with electrooptic timing modulation			
94	15-FEB-2023	Prof. Maruyama Tomoyuki	Nihon University
Photon Vortex Generation by Synchrotron Radiation			
95	24-FEB-2023	Prof. Sugimoto Toshiki	Institute for Molecular Science, JST PREST
Nonlinear Optical Vibrational Spectroscopy for Unveiling Novel Structural Properties of Water Molecules on Solid Surfaces			
96	9-MAR-2023	Prof. Gopal Dixit	Indian Institute of Technology Bombay
Two-dimensional materials under tailored laser pulses			



第 88 回 徳島大学 安井教授



第 95 回 分子科学研究所
杉本准教授



第 96 回 インド工科大学
Prof. Gopal Dixit

S-cube (スーパーサイエンスセミナー)

中学高校生を中心に一般の方に光科学についての理解を深めていただくことを目的に、第一線の研究者による講義「S-cube (エスキューブ：スーパーサイエンスセミナー)」を開講しています。

2022年度は合計6回(第216回～第221回)開催しました。

Webサイト：<https://www.qst.go.jp/site/kansai-topics/29911.html>

216	29-JUL-2022	講師：宮坂 泰弘 先端レーザー技術開発グループ	42人参加
	テーマ：レーザーの基礎と身の回りのレーザー応用技術		
217	9-AUG-2022	講師：畑 昌育 X線レーザー研究グループ	26人参加
	テーマ：レーザーでつくる夢のイオンビーム？次世代がん治療装置の最前線		
218	9-FEB-2023	講師：神門 正城 光量子科学研究部	8人参加
	テーマ：高強度レーザーによる放射線の発生と利用		
219	10-FEB-2023	講師：小島 完興 X線レーザー研究グループ	41人参加
	テーマ：レーザーでつくる夢のイオンビーム～次世代がん治療装置の最前線～		
220	8-MAR-2023	講師：中新 信彦 高強度レーザー科学研究グループ	1人参加
	テーマ：レーザーの基礎知識について		
221	24-MAR-2023	講師：乙部 智仁 超高速光物性研究グループ	18人参加
	テーマ：「レーザー微細加工技術」に関する講義		



左：徳島市立高等学校 (S-cube)



右：岩手県立大船渡東高等学校 (実験室棟見学)

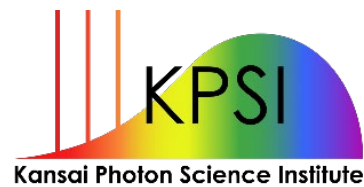
関西光科学研究所2022年度年報
KPSI Annual Report 2022

【発行】
2023(令和5)年6月

【編集・発行】
国立研究開発法人量子科学技術研究開発機構
関西光量子科学研究所 管理部庶務課

【印刷】
株式会社 春日

©2023 国立研究開発法人量子科学技術研究開発機構



Kansai Photon Science Institute
Foundational Quantum Technology Research Directorate
National Institutes for Quantum Science and Technology

8-1-7, Umemidai, Kizugawa-shi, Kyoto 619-0215, Japan
<https://www.qst.go.jp/site/kansai-english/>